

Federico Antonio D'Isa, Daniel Carralero, Tilmann Lunt, ASDEX Upgrade Team

Evolution of the SOL plasma background at density shoulder formation

**IPP 17/53
Dezember, 2016**

Università degli Studi di MILANO - BICOCCA

DIPARTIMENTO DI FISICA G. OCCHIALINI

Corso di Laurea Magistrale in Fisica

ELABORATO PER LA PROVA FINALE DI LAUREA MAGISTRALE



**Evolution of the scrape-off layer plasma
background at density shoulder formation**

Relatore:

Claudia Riccardi

Correlatori:

Daniel Carralero

Tilmann Lunt

Candidato:

Federico Antonio D'Isa

Matricola 752559

Anno Accademico 2015-2016

*Ai miei genitori,
A mia sorella,
A mia nonna.*

One of the main problems of our age is the ever increasing demand of energy. This prompts the search for new energy sources which should have the advantages of being nearly inexhaustible and usable to produce a predictable amount of energy. A possible solution is to build a reactor based on nuclear fusion. ITER will be the first divertor Tokamak to reach fusion break even and it will pave the way to a commercial use of fusion to produce sustainable and clean energy. One of the biggest obstacles to the construction of a commercial fusion reactor is represented by the heat and particle flux toward the main chamber plasma facing components and the divertor targets. A fusion reactor will likely experience power loads and erosion on the verge of the technical limits of available plasma facing materials. To predict properly the distribution of those fluxes between the divertor and the main chamber, a better understanding of the physics in the open field lines region (called Scrape-off layer or SOL) is required. This thesis, being developed in partnership with the Max-Planck-institut für Plasmaphysik (Garching bei München, DE), is framed in this context.

In the SOL of L-mode (low confinement) discharges, qualitatively two kinds of density profiles can be distinguished. The first one is characterized by a strong density gradient in the vicinity of the separatrix, followed by a flat region towards the far SOL. The second profile lacks such a strong gradient and displays an almost linear decay in the whole SOL. The latter kind of density profile is characterized by stronger fluxes toward the first wall with respect to the first kind. This may be a threat for the ITER unlike the divertor targets which are made of tungsten, the first wall will be made beryllium which can suffer damage from sputtering.

This work is focused on understanding the physics behind the transition between those two profiles, the so-called density shoulder formation. After the shoulder formation it is observed that filaments, namely coherent structures that enhance the transport in the outer region of Tokamaks, undergo a regime transition that enhances their transport at the outboard midplane. It is believed that inhomogeneous perpendicular transport related to the filaments is responsible for the density shoulder formation. The regime transition occurs because of the increase of the global collisionality. Since the plasma parameters (n_e , T_e) change significantly along a field line it is needed a full description of the plasma in the SOL in order to study where such increase of the collisionality takes place.

The first part of this work is focused on use EMC3-EIRENE simulations, in continuation of previous work, to provide a detailed 3D plasma background of the SOL condition in two different L-mode discharges carried out in the ASDEX Upgrade Tokamak, featuring different degrees of shoulder formation: case A (simulation of discharge 29231) in which no shoulder is observed and case B (simulation of discharge 29887) after the transition. In the simulation, cross field transport is described by the perpendicular particle and energy diffusive time independent transport coefficients: D_{\perp} , $\chi_{\perp}^{e,i}$. The simulations are compared with the experimental measurements at the midplane, the X-point and the divertor targets. The comparison shows that previous simulations of case B strongly underestimate the electron and ion temperatures. In order to improve the simulation results and provide a realistic description of the SOL plasma background

several simulations are performed. As a result, the final agreement between experimental measurement and numerical results has been improved with respect to the original work. The simulations show that:

- It is possible to simulate the density shoulder formation by increasing transport a factor of 3 only at the outer midplane, in good agreement with the experimental measurements.
- A reduction of the particle transport coefficient at the limiter surface is needed in order to match its experimental profiles.
- A better agreement is achieved if the energy transport coefficients are decoupled from the particle transport coefficient and reduced with respect to the previous simulations.

The results provided by the simulation are used to bridge the lack of diagnostics, that (for technical reasons) cannot cover the whole tokamak. The provided 2D picture of the SOL is used to study the plasma background conditions after the shoulder formation. Analyzing the neutral density distribution provided by the code, it is observed that, after the shoulder formation a cloud of neutral particles crosses the separatrix and covers the divertor targets. Moreover it has been found that, among the studied processes, the most likely to cool down the filaments in the SOL after the shoulder formation is the interaction between ions and neutrals. At the same time, the collisionality is studied as a line integrated parameter from a outer target to the midplane is studied. It is found that before the shoulder formation, collisionality at the midplane is below unity, but after the shoulder formation it is above unity, in good agreement with the model expectations. Moreover, in the case B it saturates near the divertor target and the contribution of the midplane is negligible. On the other hand, in case A the whole length of the field line contributes to the collisionality.

Contents

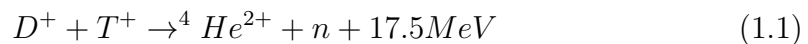
1	Introduction	1
2	Theory	5
2.1	Plasma description and parameters overview	5
2.1.1	Magnetized plasma	5
2.2	Tokamaks	6
2.2.1	Coordinates system for a tokamak	8
2.2.2	Plasma equilibrium in a tokamak	10
2.3	Scrape-off layer	11
2.3.1	Divertor	12
2.3.2	Detachment regimes	12
2.4	Collisions	12
2.4.1	Thermalization time	13
2.5	Filaments	14
2.5.1	Transport mechanism	15
2.5.2	Filaments velocity	16
2.6	Density shoulder in the scrape-off layer	17
3	Experimental setup	21
3.1	ASDEX Upgrade	21
3.2	Diagnostics	23
3.2.1	Lithium beam	23
3.2.2	Edge Thomson scattering diagnostic	23
3.2.3	Edge charge-exchange recombination spectroscopy	24
3.2.4	Manometers	25
3.2.5	Langmuir probes	25
3.2.6	Diagnostics arrangement in ASDEX Upgrade	28
4	EMC3-Eirene code	33
5	EMC3-Eirene simulations	37
5.1	Review of previous work	38
5.2	Definition of the position of the separatrix	41
5.3	Enhanced transport at the outboard midplane	45
5.4	Parameter optimization	48
5.4.1	Energy transport coefficient	48
5.4.2	Amplitude of the filament-related transport	49

5.4.3	Poloidal width of the filament-related transport	50
5.4.4	Reduction of the transport after the limiter	51
5.5	Final Simulations	53
6	Background plasma analysis	57
6.1	X-point analysis	57
6.2	Neutral particle density	58
6.3	Collisionality along a field line	62
6.4	Thermalization time	64
6.5	Perpendicular fluxes	67
7	Summary and conclusions	69
8	Acknowledgment	71

Chapter 1

Introduction

One of the main problems of our age is the ever increasing demand of energy. Nowadays the energy is produced mainly using not renewable resources, that have the disadvantage of being limited and to produce pollution. On the other hand the renewable resources currently available produce a variable amount of energy energy storage is needed in order to use those systems as major energy sources. Almost every energy demand prediction based on economic models highlights a drastic increase of energy consumption in the future [1]. This prompts the search for new energy sources which should have the advantages of being nearly inexhaustible and usable to produce a predictable amount of energy. A possible solution is to build a reactor based on nuclear fusion. Figure 1.1 (left) shows the binding energy per nucleon, it grows with the mass until ^{56}Fe then to gain energy it is possible to fuse two light atoms to form heavier ones. Fusion happens when two nuclei are close enough to overcome the repulsive Coulomb barrier, thanks to the tunnel effect, and interact with each other through the strong interaction field which is attractive. Figure 1.1 (right) shows the cross sections for different fusion processes. Among all the possible reactions the most convenient is the one that involves Deuterium (D) and Tritium (T), which has the largest cross section:



Deuterium has a relative abundance of 0.015 % and can be easily extracted from water, Tritium is unstable ($\tau_{\frac{1}{2}} = 12y$) and can not be found in nature, but can be bred from Lithium via the reaction:



Lithium is widely available the earths crust and also in the oceans.

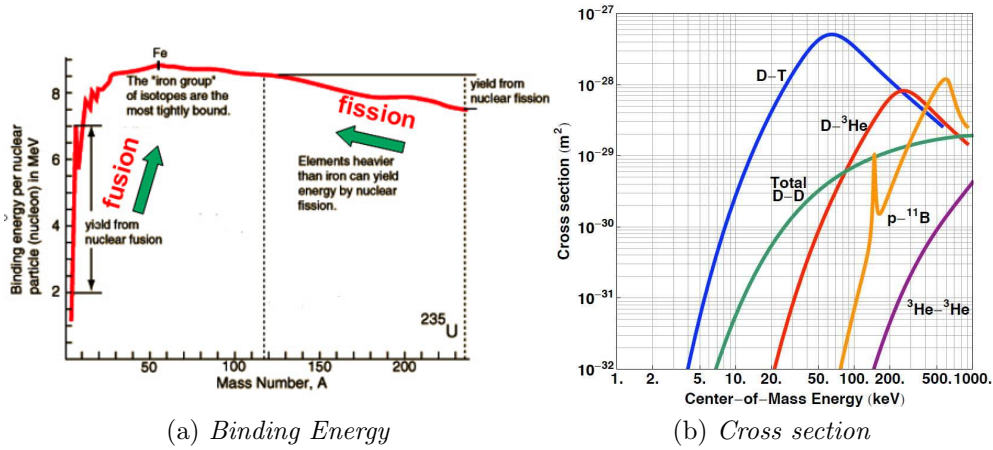


Figure 1.1: On the left the binding energy per nuclear particle against the mass number. On the right the cross section of $D - T$, $D - D$, $D - {}^3\text{He}$, $p - {}^{11}\text{B}$, ${}^3\text{He} - {}^3\text{He}$ reactions against particle energy.

Nuclear fusion is possible only when the nuclei are heated to very high thermonuclear temperatures, for a mixture of deuterium and tritium a temperature of at least $\simeq 10\text{keV}$ is required. At such temperatures the $D - T$ mixture is in the plasma state (see section 2.1). In order to achieve fusion on the earth, an auxiliary power supply is necessary to compensate the loss of energy due to different physical processes such as: bremsstrahlung emission, impurity radiation [1]. It is useful to define the ratio between fusion power output and the input power. Thus, for fusion power to be successful, the minimum criterion for a fusion power plant is $Q > 1$. The state $Q = 1$ is known as the break-even condition, when fusion output power just equals the auxiliary input power. The thermonuclear fusion plasma can also be confined in an ignited state when $Q \rightarrow \infty$, that means that no external heating is needed because the necessary power is supplied by the fusion reaction themselves, this condition is fulfilled in the stars. In order to harvest energy from fusion ($Q > 1$), the plasma density (n), temperature (T) and energy confinement time (τ_e) of the plasma must satisfy the Lawson criterion, in which also the bremsstrahlung emission is considered as energy loss [1]:

$$nT\tau_e \geq 1.5 \cdot 10^{21} \left[\frac{\text{keV s}}{\text{m}^3} \right] \quad (1.3)$$

The plasma temperature T determines the average collision cross section. The plasma density n is the number of particles available to fuse, so it determines the rate of fusion reactions. Figure 1.2 shows the Break-even condition, Lawson criterion and the ignition condition. Since the probability of a fusion reaction is low, deuterium and tritium must be confined at high temperature for a sufficiently long period of time (τ_e) to obtain a reaction.

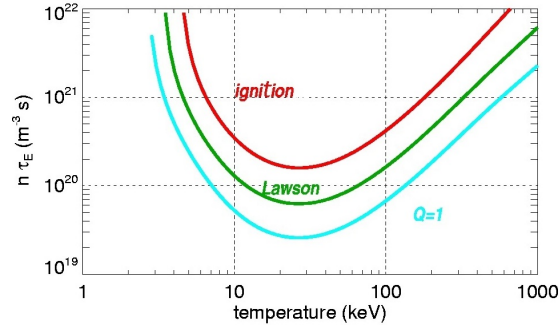


Figure 1.2: Product of density n and energy confinement time τ_e against temperature T . The lines denote the break-even ($Q = 1$, light blue), Lawson criterion (green), ignition ($Q = \infty$, red) .

Two approaches for achieving the Lawson condition are being investigated: magnetic confinement (high temperature and long confinement time but low density) and inertial confinement (high density and high temperature but short confinement time) [1]. The first one is presently the most promising path in order to develop future fusion reactors. Several different devices have been built until now, the Tokamak type (see section 2.2) is the most advanced of them. Up to now none of them succeed to satisfy the ignition condition due to lack of technology. However to accomplish a fusion reactor, an international project, lead by Europe, was born. The main effort is to build the first device, which will respond to the needs of satisfy the Lawson criteria: ITER (the “way” in latin, figure 1.3), it will be the first experimental device for fusion experiments with $Q > 1$ and pave the way to a commercial use of fusion for producing sustainable and clean energy. The project is a collaboration of EU, USA, Russia, Japan, India, China and South Korea and will be built in Cadarache (FR).

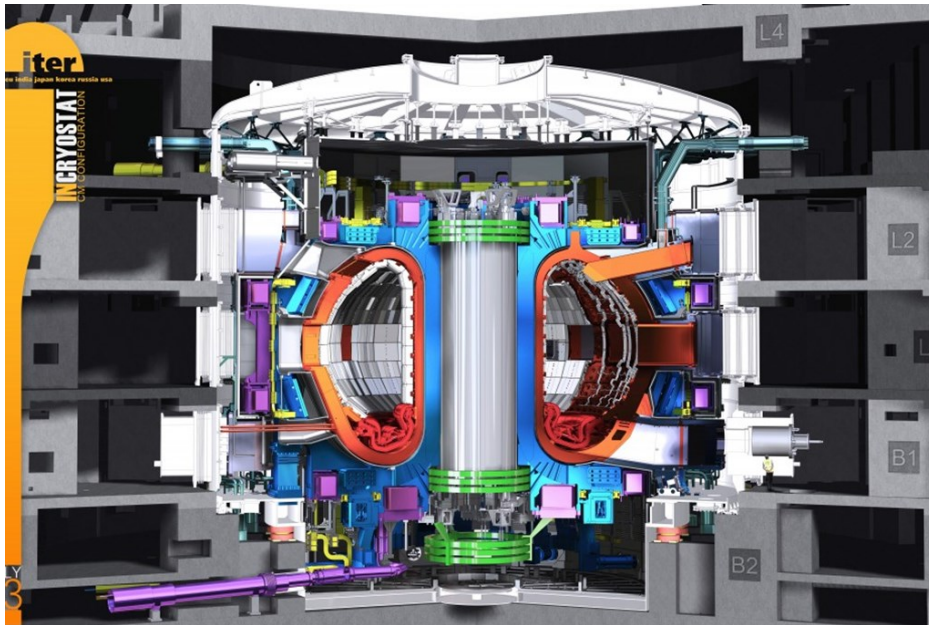


Figure 1.3: The ITER plan.[2]

The machine has been designed specifically to produce a ten-fold return on energy ($Q=10$), study plasmas under similar conditions to those expected in a future power plant, to test technologies, to test tritium breeding and to demonstrate the safety characteristics of a fusion device [2].

One of the biggest obstacles to the construction of ITER and, more in general, for a commercial fusion reactor is the heat and particle fluxes toward the plasma facing components and the divertor targets. In fact these devices will certainly experience power loads and erosion on the verge of the technical limits of available plasma facing materials. To predict properly the distribution of those fluxes between the divertor and the main chamber a complete understanding of the physics in the plasma-wall interaction region (called scrape-off layer or SOL, see section 2.3) is required. My thesis, that was developed in partnership with Max-Planck-Institut für Plasmaphysik (Garching bei München, DE), is framed in this context. In the SOL of L-mode (low confinement) discharges, qualitatively two kinds of profiles can be distinguished. The first one is characterized by a strong density gradient in the proximity of the separatrix, followed by a flat region towards the far SOL. The second profile lacks such gradient and displays a somehow constant decay length in the whole Scrape off layer (see section 2.6). This work is focused on understanding the physics behind the transition between those two profiles, the so-called density shoulder formation. This is likely caused by inhomogeneous perpendicular transport related to the filaments, which are coherent structures that enhance the transport in the outer region of Tokamaks (see section 2.5). ITER main chamber is not designed to withstand strong fluxes, since it is made of beryllium, thus the elements of the main chamber in contact with the plasma (plasma facing components, PFCs) may be damaged by the shoulder formation. Some preliminary studies of the background plasma conditions created after the density shoulder formation were carried out [3] using the EMC3-Eirene code that takes in account the interaction between the plasma and the plasma facing components, while most of the simulation codes normally used do not consider the main chamber recycling, that could play an essential role. The aim of this work is to use the EMC3-EIRENE code to provide a detailed 3D simulation of the SOL condition in two different L-mode discharges at different degrees of shoulder formation. The results provided by the simulations are used to answer the questions still present around the shoulder formation:

- It is known that the filament-related transport enhances because the filaments undergo a regime transition (see section 2.5). This occurs because of an increase of collisionality, but where does the increase take place?
- The shoulder formation is observed in correspondence with the cooling down of the ions in the SOL. Which is the mechanism that cools the ions?

Moreover, the diagnostics used in the experiment can not study the whole Tokamak, therefore the simulation results are used to bridge the lack of diagnostics and provide a 2D picture of the scrape-off layer.

Chapter 2

Theory

2.1 Plasma description and parameters overview

A plasma is a state of matter in which positive and negative charges coexist in a system dominated by collective motion. If an electric field is introduced, the particles in the plasma shield it. This effect is called Debye shielding. The characteristic length of this shield is called Debye's length and it is defined as:

$$\frac{1}{\lambda_d^2} = \sum_{\sigma} \frac{1}{\lambda_{\sigma}^2} \quad (2.1)$$

$$\lambda_{\sigma} = \sqrt{\frac{\epsilon_0 k_b T_{\sigma}}{n_{\sigma} q_{\sigma}^2}} \quad (2.2)$$

Where σ index represents the species (electron and the different types of ions), T is the temperature, n is the density and q the particle charge. From this comes the plasma propriety called quasi neutrality: in a region of size $L \gg \lambda_d$ the plasma overall appears neutral. In a plasma with only one type of positive ion this means:

$$n_e \simeq n_i Z_i \quad (2.3)$$

2.1.1 Magnetized plasma

In presence of a magnetic field \vec{B} , because of the Lorentz force ($\vec{F}_l = q\vec{v} \times \vec{B}$), a charged particle moves around a field line in a uniform circular motion which radius and frequency are named Larmor radius and cyclotron frequency:

$$r_{l\sigma} = \frac{m_{\sigma} v_{\perp\sigma}}{|q_{\sigma}| B} \quad (2.4)$$

$$\Omega_{\sigma} = \frac{|q_{\sigma}| B}{m_{\sigma}} \quad (2.5)$$

where m is the mass σ -particle, v_{\perp} the perpendicular velocity with respect to the magnetic field.

2.2 Tokamaks

Although 98% of ordinary matter in universe is in a plasma state, natural plasma is quite rare on the Earth (lighting, fire or auroras), so to study this fundamental state of matter during the last hundred years different devices were built. A complete overview of each of them is out of purpose of this short introduction, here only the most common confinement devices will be discussed, namely devices which use magnetic field in order to create and confine a plasma. Among them the most developed one is the tokamak. It is characterized by a magnetic field that has a torus shape.

Earlier devices were simple magnetized torus, but this shape is effected by strong outwards radial fluxes due to drift of the particles gyro center. This effect can be explained considering the motion of charged particles in a magnetic field with a presence of an external force, the gyro center moves with a velocity that is:

$$v_F = \frac{\vec{F} \times \vec{B}}{qB^2} \quad (2.6)$$

where \vec{F} is the external force. In a toroidal magnetic field a magnetic gradient that point to the center of torus is always present. Moreover the magnetic field lines have a curvature. Both curvature and gradient create two effective forces that according to equation 2.6 generate two drift:

$$\vec{v}_c = m\vec{v}_{\parallel}^2 \frac{\hat{r} \times \vec{B}}{qB^2} \quad (2.7)$$

$$\vec{v}_{\nabla B} = -\mu \frac{\vec{\nabla} |B| \times \vec{B}}{qB^2} \quad (2.8)$$

In addition the presence of an electric field leads to a third drift.

$$\vec{v}_E = \frac{\vec{E} \times \vec{B}}{B^2} \quad (2.9)$$

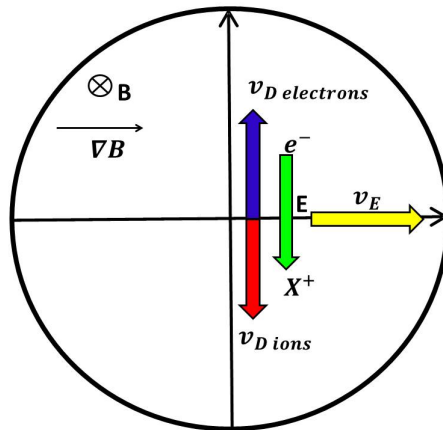


Figure 2.1: The drifts in a simple magnetized torus.

where $\mu = \frac{mv_{\parallel}^2}{2B}$ is the magnetic momentum, \vec{B} is the magnetic field, E the electric field, q is the particle's charge and v_{\parallel} is the parallel velocity.

v_E is the drift velocity due to the electric field, it is important to notice that it does not depend on the charge, so for both electron and ion it has the same direction. Otherwise v_c and $v_{\nabla B}$, depend on the charge, so they lead to a charge separation. Figure 2.1 shows the gradient, curvature and electric field drifts in a simple magnetized torus with circular cross section. This explains why a purely toroidal magnetic field can not confine the plasma particles: the curvature and gradient drifts produce opposite particle drifts for the ions and the electrons, leading to a charge separation; the resulting electric field leads to a rapid loss of the plasma on the walls due to the $\vec{E} \times \vec{B}$ drift.

To prevent the charge separation, an additional component of the magnetic field is required along the poloidal cross-section of the torus: the poloidal magnetic field. In tokamaks it is formed by driving a toroidal current in the plasma itself. The resultants field lines wrap infinitely around the torus in nested toroidal surfaces forming closed magnetic flux surfaces.

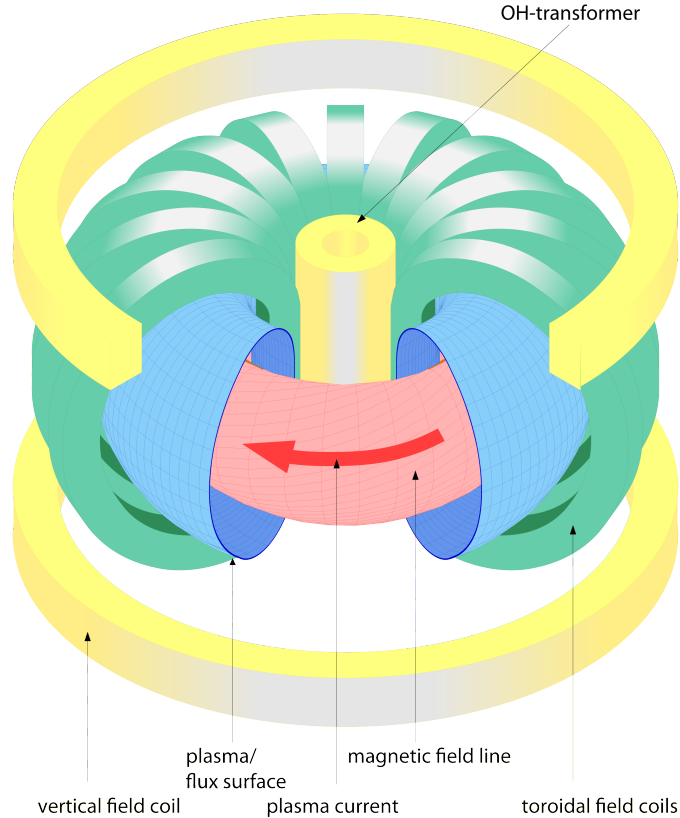


Figure 2.2: A picture of a tokamak, the image shows the different component.

Because of the shape of $B_{total} = B_{toroidal} + B_{poloidal}$, a field line for each toroidal pass crosses a given poloidal plane at different locations. The number of toroidal transits after which a field line fulfills one poloidal transit is expressed by the safety factor q :

$$q \simeq \frac{rB_{\phi}}{RB_{\theta}} \quad (2.10)$$

Where r is the minor radius of any particular flux surface, R is the major radius of the torus, B_ϕ is the toroidal magnetic field, B_θ is the poloidal magnetic field. The ratio between poloidal and toroidal magnetic field is θ_{pitch} :

$$\theta_{pitch} \simeq \frac{B_\theta}{B_\phi} \quad (2.11)$$

The first tokamak was designed with circular section, but it was found that a non-circular plasma section tends to be more stable and to resist higher mechanical loads, typically a D-shaped one.

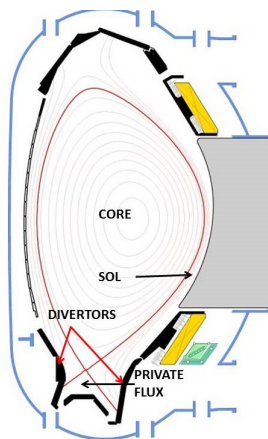


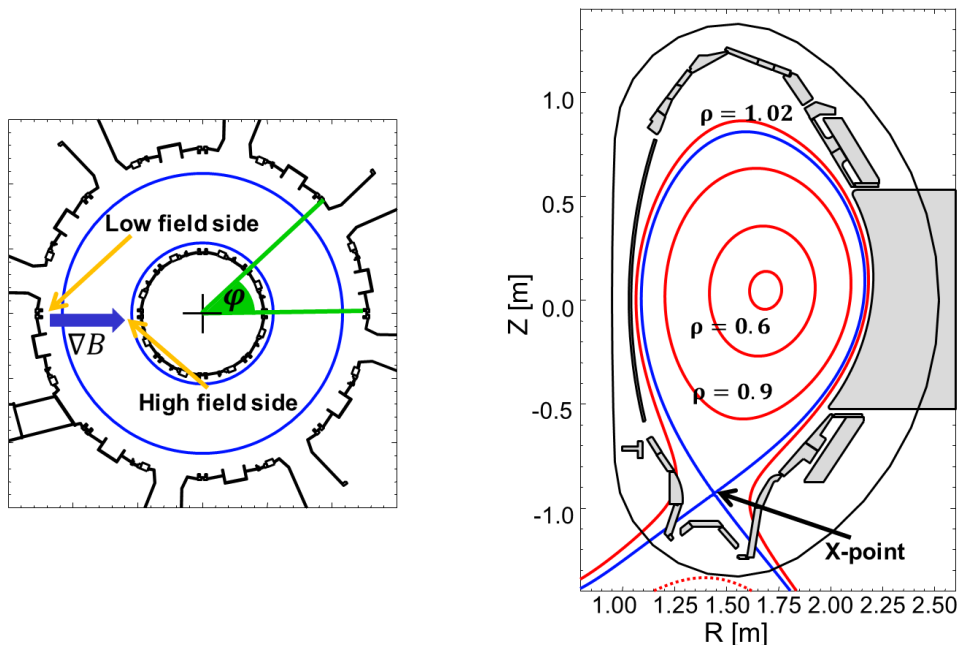
Figure 2.3: A poloidal section of Asdex Upgrade.

Another improvement to the basic design is to shape the magnetic lines inside the machine. In order to make the field lines strike on a chosen target, the so-called divertor targets, not all flux surfaces are closed. In such configuration the X-point, defined as the point where the poloidal component vanishes, is formed by field shaping, possible by means of dedicated coils. The magnetic flux surface that intersects the X-point is called separatrix and it is the last closed magnetic surface. In this configuration the divertor bears most of the thermal loads carried by the plasma particles which flow along the open field lines to the targets. As a result the divertor is characterized by a higher plasma density, that creates a density gradient along the field lines and reduces the energy of the particles that hit the targets. Moreover a strong pumping in the divertor regions prevents the impurities to affect the plasma inside the last closed surface. Figure 2.3 shows a poloidal cross section of a D-shaped tokamak. For the described system three magnetic regions can be distinguished: the core inside the separatrix, the scrape-off layer (SOL) between the separatrix and the wall and the private flux region between the two divertor legs .

2.2.1 Coordinates system for a tokamak

Since tokamaks have a toroidal geometry, the simplest way to define coordinates used to define a position in the machine are the cylindrical coordinates. An angle ϕ describes the toroidal position and the R and z coordinate describe the position

inside a poloidal section at fixed angle. $R = 0$ is the axis of the torus and $z = 0$ in the equatorial plane. In other words, the machine is described by a toroidal angle that point to a poloidal section, the section is then described by a Cartesian coordinates system with the origin in geometric torus center. Figure 2.4 shows a scheme of the coordinates used to describe a tokamak. In literature it is common to refer to the region of the torus near the geometrical center as high field side (HFS). On the contrary, the opposite region is called low field side (LSF, figure 2.4 left).



(a) An example toroidal projection.

(b) An example of poloidal section.

Figure 2.4: The coordinate systems in a tokamak. Picture on the left shows a toroidal projection of a tokamak. Picture on the right shows a poloidal cross section. The axis are the R and z coordinates. The dotted red lines are the magnetic surface corresponding to different ρ . In both figures, the blue solid line represents the separatrix.

Another set of coordinates that are often used is the normalized flux coordinate. Each magnetic surface in the tokamak is characterized by the magnetic flux, then for a point (R, z) lying on magnetic surface the ρ is defined as:

$$\rho = \sqrt{\frac{\Psi(R, z) - \Psi(R_0, z_0)}{\Psi(R_{sep}, z_{sep}) - \Psi(R_0, z_0)}} \quad (2.12)$$

(R_{sep}, z_{sep}) are the separatrix coordinates, (R_0, z_0) the magnetic axis coordinates and Ψ is the function that describes the magnetic flux:

$$B_R = -\frac{1}{2\pi R} \frac{\partial \Psi}{\partial z} \quad (2.13)$$

$$B_z = -\frac{1}{2\pi R} \frac{\partial \Psi}{\partial R} \quad (2.14)$$

At the separatrix $\rho = 1$, the core region has $\rho < 1$, in the scrape-off layer $\rho > 1$ (figure 2.4 right).

2.2.2 Plasma equilibrium in a tokamak

A simple way to describe magnetized plasma in a tokamak is via the magneto hydrodynamic (MHD) equations [4]:

$$\frac{d\rho}{dt} = \rho \vec{\nabla} \cdot \vec{v} \quad (2.15)$$

$$\rho \frac{d\vec{v}}{dt} = \vec{j} \times \vec{B} - \vec{\nabla} p \quad (2.16)$$

$$\frac{dp}{dt} = -\gamma p \vec{\nabla} \cdot \vec{v} \quad (2.17)$$

$$\vec{E} + \vec{v} \times \vec{B} = 0 \quad (2.18)$$

$$\vec{\nabla} \times \vec{E} = -\frac{\partial \vec{B}}{\partial t} \quad (2.19)$$

$$\vec{\nabla} \times \vec{B} = \mu \mu_0 \vec{j} \quad (2.20)$$

$$\vec{\nabla} \cdot \vec{B} = 0 \quad (2.21)$$

where γ , ρ , p , \vec{v} are the adiabatic index, the fluid mass density, the pressure and the fluid velocity respectively. Considering in equation 2.16 a time scale longer than $\tau_A = \frac{L_0}{v_A}$ and $\tau_s = \frac{L_0}{c_s}$, where $v_A = \sqrt{\frac{B^2}{\mu_0 \rho}}$, $c_s = \sqrt{\frac{p}{\rho}}$ where L_0 is the typical dimension of the system and under the assumption $\vec{v} \ll c_s$ equation 2.16 can be simplified onto [4]:

$$\vec{j} \times \vec{B} = \vec{\nabla} p \quad (2.22)$$

During a discharge plasma conditions change in time, for example because of a change in the external heating, these changes are slow respect to τ_A and τ_s . During these slow variations the plasma goes through a sequence of states that satisfy equation 2.22.

In a tokamak the magnetic field lines are bent in a torus, so it is useful to split the magnetic field vector and the density current in toroidal and poloidal components: $\vec{B} = \vec{B}_{pol} + \vec{B}_{tor}$ and $\vec{j} = \vec{j}_{pol} + \vec{j}_{tor}$. The poloidal components can be expressed as:

$$\vec{j}_{pol} = \frac{1}{R} \hat{e}_\phi \times \vec{\nabla} G \quad (2.23)$$

$$\vec{B}_{pol} = -\frac{1}{R} \hat{e}_\phi \times \vec{\nabla} \xi \quad (2.24)$$

where R and ϕ are the cylindrical coordinates and $G(R, z)$ and $\xi(R, z)$ are the stream functions of the poloidal density current and magnetic field respectively. Equations 2.23 and 2.20 imply that the toroidal magnetic field can be expressed as a function of G :

$$\vec{B}_{tor} = -\mu_0 \frac{G}{R} \hat{e}_\phi \quad (2.25)$$

Equation 2.24 says that a field line lies on a surface with constant flux. At the same time considering

$$0 = \vec{B} \cdot (\vec{j} \times \vec{B}) = \vec{B} \cdot \vec{\nabla} p \quad (2.26)$$

the pressure must be constant along a field line. Moreover since $\vec{j}_{pol} \times \vec{B}_{pol} = 0$ the density current stream function (G) can be expressed as a function of ξ , and therefore no poloidal current can cross a flux surface. Finally it can be shown [4] that considering the inner product with $\vec{\nabla}\xi$ of equation 2.22 and the Ampere's law 2.20 gives the toroidal current and the closure of the system, known as Grad-Shafranov equation:

$$\frac{\partial^2 \xi}{\partial R^2} - \frac{1}{R} \frac{\partial \xi}{\partial R} + \frac{\partial^2 \xi}{\partial z^2} = \mu_0 R j_{tor} = -\mu_0 R^2 \frac{\partial p(\xi)}{\partial \xi} - \frac{\mu_0^2}{2} \frac{\partial F(\xi)^2}{\partial \xi} \quad (2.27)$$

The one discussed until now is a model and in particular the closure of this model is valid under the assumption of equation 2.22. Plasma rotation and not isotropic plasmas may require corrections. The slow time evolution is expressed in the pressure and current density flux $p(\xi, t)$ and $F(\xi, t)$, the solution of equation 2.27 depends parametrically on the time.

2.3 Scrape-off layer

The SOL is the region where plasma is in contact with solid surfaces. In this region the interaction of ions and electrons with molecules, atoms and solid surface dominate the overall plasma behavior. For these reasons, the SOL is of particular interest when it comes to deal with such problems as:

- The exhaust of fusion power without excessive damage to the vessel walls;
- The removal of fusion ash (helium) and other impurities from the core plasma;
- Recovery of fusion fuel and prevention of tritium retention in plasma-facing components;
- Control of material erosion and migration within the vacuum vessel.

It has been found that the energy confinement time critically depends on the plasma properties near the edge region of the tokamak plasma, and hence the edge region in tokamaks has to be handled with care.

2.3.1 Divertor

The SOL surrounds the confined plasma outside the separatrix, intercepted by the divertor targets at both ends. Power and particle fluxes enter the SOL from the core and exit it either along the magnetic field lines directly to the divertor target plates, or across the magnetic field lines to the vacuum chamber walls. The use of divertor moves the location of the main plasma-surface interaction away from the confined plasma, facilitating impurity control. In addition, by guiding the plasma exhaust stream into the divertor region, the neutralization at the divertor target plates results in a higher neutral gas pressure, allowing efficient pumping. Furthermore, divertor operation allows to achieve low plasma temperature at the target plate, in association with strong volume losses, such as radiation, charge exchange and recombination. This not only reduces impurity production and erosion at the target plate, but also provides an effective means for controlling the power reaching the divertor plate, which is one of the major concerns for high power and long pulse operation [1].

2.3.2 Detachment regimes

At low temperature and high density, the physics of the divertor is largely influenced by the presence of neutrals. The birth, history and annihilation of a neutral are controlled by recombination (target and volume recombination), ion neutral interaction (charge exchange and elastic collisions) and electron impact ionization. At sufficiently low temperature and high density in front of the targets, volume recombination and charge-exchange losses become important. The plasma enters into the detached regime. Detachment is characterized experimentally by the following main features [1]:

- A reduction of ion fluxes to the target, mainly due to synergistic effects of recombination and ion-neutral friction;
- A reduction of plasma pressure near the target, possible due to friction between ion and neutral;
- A reduction in heat flux reaching the target plate by volume losses including radiation, recombination and charge-exchange.

2.4 Collisions

Inside a Debye sphere (a sphere of volume $\frac{3}{4}\pi\lambda_d^3$) the charges are not shielded, so each particle interacts with the others and Coulombian collisions take place. In a plasma, different types of collisions are possible such as electron-ion, electron-electron, ion-ion, in which both energy and momentum can be exchanged. Momentum loss frequency is required for calculating resistivity, viscosity, particle and energy diffusion. Energy loss frequency is required for calculating equilibrium time and energy transfer between species. Under the assumption of a Maxwellian

distribution for electrons and ions, the frequency for momentum exchange can be expressed as [5]:

$$\bar{\nu}_{ei} = \frac{\sqrt{2}}{3\sqrt{\pi}} n_i \left(\frac{Ze^2}{4\pi\epsilon_0} \right)^2 \frac{4\pi}{m_e^{\frac{1}{2}} T_e^{\frac{3}{2}}} \ln(\Lambda_e) \quad (2.28)$$

$$\bar{\nu}_{ee} \simeq \frac{1}{\sqrt{2}} \bar{\nu}_{ei} \quad (2.29)$$

$$\bar{\nu}_{ie} = \frac{n_e m_e}{n_i m_i} \bar{\nu}_{ei} \quad (2.30)$$

$$\bar{\nu}_{i_1 i_2} = \frac{\sqrt{2}}{3\sqrt{\pi}} n_{i_2} \left(\frac{q_{i_1} q_{i_2}}{4\pi\epsilon_0} \right)^2 \frac{4\pi}{m_{i_1}^{\frac{1}{2}} T_{i_1}^{\frac{3}{2}}} \frac{m_{i_2}}{m_{i_1} + m_{i_2}} \ln(\Lambda_{i_1}) \quad (2.31)$$

where Λ_σ the coulomb logarithm ($\Lambda = \frac{\lambda_d}{b_{\frac{\pi}{2}}}$ where $b_{\frac{\pi}{2}}$ is the impact parameters for a coulombian scattering at an angle of 90°).

It should be noted that ion-electron collision frequency is much lower than electron-ion collision frequency. This is because ion possesses much more momentum for the same velocity. Moreover the collision frequency behaves as $T_e^{-\frac{3}{2}}$, so in a hot plasma collisions rate is low. From momentum exchange frequency can be calculated the energy exchange frequency as:

$$K_{\nu_{\alpha\beta}} = \frac{2m_\alpha}{m_\alpha + m_\beta} P_{\nu_{\alpha\beta}} \quad (2.32)$$

where α, β describe the two particle species.

2.4.1 Thermalization time

In section 2.6 will be shown that the filaments (but also the ions) in the SOL cool after the density shoulder formation. In order to understand why this occurs it is important to study how the ions lose their energy in the SOL. When the electrons enter the scrape-off layer, they lose the majority of their energy, due to parallel heat conduction (the characteristic thermalization time for the ions is shown in equation 2.38). Since ions are heavier than electrons the parallel conduction is smaller and ions lose their energy via different processes.

If an ion gives its energy to an electron it will rapidly lose it, as explained so far. As a consequence the collisions between ions and electrons reduce the ions energy and eventually thermalize with electrons. The energy exchange between electrons and ions can be written as [6]:

$$\frac{\partial}{\partial t} T_i = 3\nu_{ie}(T_e - T_i) \quad (2.33)$$

The characteristic thermalization time for electron-ion collisions if $\frac{\partial}{\partial t} T_i \simeq \frac{T_i}{\tau_{ie}}$ is supposed can be approximated as:

$$\frac{1}{\tau_{ie}} \simeq 3\nu_{ie} \frac{T_i - T_e}{T_i} \quad (2.34)$$

where ν_{ie} is the collision rate for momentum exchange between ion and electron discussed in section 2.4.

Another process that dissipates the ion energy is the collision with neutrals that trigger different reactions such as charge exchange and recombination. Among them the most significant one is the charge exchange. Therefore only this reaction will be taken into account. The energy exchange between ions and neutrals is described by [6]:

$$\frac{\partial}{\partial t} T_i = 3\nu_{cx}(T_n - T_i) \quad (2.35)$$

under the same assumption of equation 2.34 the characteristic time for this process is then:

$$\frac{1}{\tau_{ni}} \simeq \nu_{cx} \frac{T_n - T_i}{T_i} = 3.2 \cdot 10^{-28} \left(\frac{3}{2} T_i\right)^{-0.2} \sqrt{\frac{3T_i}{m_i} n_n} \frac{T_n - T_i}{T_i} \quad (2.36)$$

where ν_{cx} is the charge exchange collision rate and n_n is the neutral density. Moreover the thermal conduction, that is responsible for the electrons cooling, drives the ions energy to the wall, the parallel loss of energy is described by [6]:

$$n_i \frac{\partial}{\partial t} T_i = \nabla \cdot (k_{\parallel} \hat{b} \nabla_{\parallel} T_i) \quad (2.37)$$

where k_{\parallel} is the parallel conduction coefficient. The characteristic time that leads to the thermalization of the ions due parallel heat conduction can be estimated as:

$$\frac{1}{\tau_{\parallel}} \simeq \frac{T_i}{m_i \nu_{ii}} \frac{1}{L_c^2} \quad (2.38)$$

where ν_{ii} is the collision frequency between ion and ion and L_c is the connection length. In a tokamak the connection length is defined as the distance along the field line, that must be covered to move from a specific position to a divertor target or a wall component.

Heat conduction is inhibited by collisions, while for the electron-ion and neutral ion characteristic thermalization time is the contrary, the higher the collision rate the faster the energy loss.

2.5 Filaments

Blobs or filaments are convective cells that transport plasma across the open magnetic field line region (SOL) and enhance the plasma interaction with the surrounding material boundaries. Figure 2.7 shows filaments in a L-mode discharge. A blob can be defined as filament of plasma that satisfies the following properties [7]:

- It has a monopole density distribution and the peak value is larger (2-3 times) than the surrounding RMS fluctuation;
- It is aligned to the magnetic field and the variation along it is smaller than in the transverse direction;

These coherent objects are spatially localized in the 2D plane perpendicular to the magnetic field and spatially elongated in the magnetic field direction. In a 3D view blobs look like field-aligned structures. Experiments show that large-amplitude, intermittent turbulence governs the edge of plasma devices: it is shown that blobs may transport up to 50% of the particles in the SOL [8, 9]. In an experiment it is possible to detect filaments as fluctuation of density 2-3 times bigger than the RMS fluctuation [7].

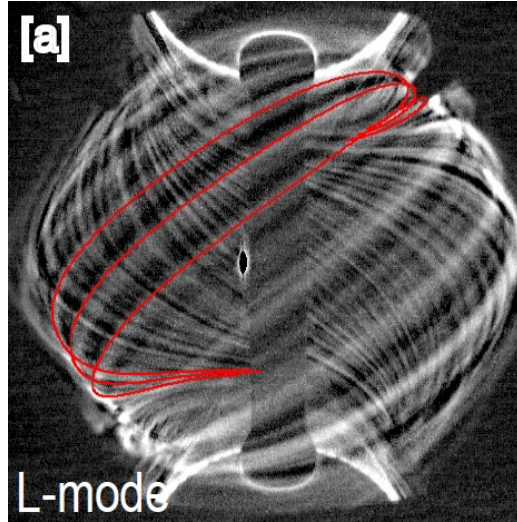


Figure 2.5: In red are highlighted filaments during an L-mode discharge [10].

2.5.1 Transport mechanism

In a tokamak a blob becomes polarized under the action of the curvature drift (equations 2.7 and 2.8). These drifts form a charge polarization that creates an electric field that moves the filament under the electric field drift. In fact the drift directions are different for electron and ion and provokes a charge separation. The resulting poloidal electric field inside the blob creates an $\vec{E} \times \vec{B}$ drift that moves the density structure. Figure 2.7 shows the polarization mechanism for a blob. In the high field side of the torus the $\vec{E} \times \vec{B}$ points toward the confined plasma. As a result the instabilities that create filaments are stabilized and no filaments are present at the high field side. Instead, in the low field side the $\vec{E} \times \vec{B}$ propels the filaments from inside the plasma to the wall.

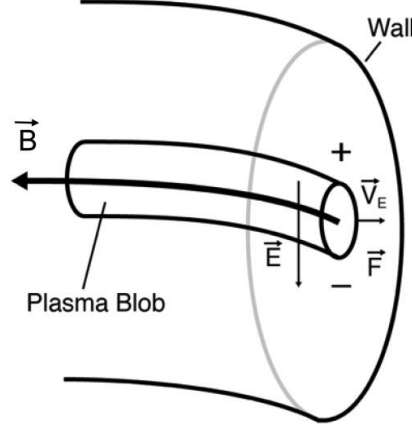


Figure 2.6: A scheme of the filaments polarization mechanism and the resulting electric field that determines their movement inside a tokamak [7].

2.5.2 Filaments velocity

Taking a reduced magnetohydrodynamics approach applied on a magnetized stationary plasma affected by a force density related to the curvature and the gradient drift, under the assumption of constant temperature. The charge conservation equation can be expressed as [11]:

$$\nabla \cdot \frac{d}{dt} \left(\frac{nm_i}{B^2} \nabla_{\perp} \phi \right) = \frac{2T}{B} \hat{b} \times \hat{e}_{\perp} \cdot \vec{\nabla} n + \nabla_{\parallel} \vec{J}_{\parallel} \quad (2.39)$$

The solutions are different according to the parallel closure used for \vec{J}_{\parallel} . Two different regimes can be found: the sheath limited regime, if the filament extends along the field line to the target plates and the current density is limited by the sheath; the inertial regime if this approximation is not valid. In this latter regime it can be approximated that $\nabla_{\parallel} \vec{J}_{\parallel} \rightarrow 0$, leading to a different solution of equation 2.39.

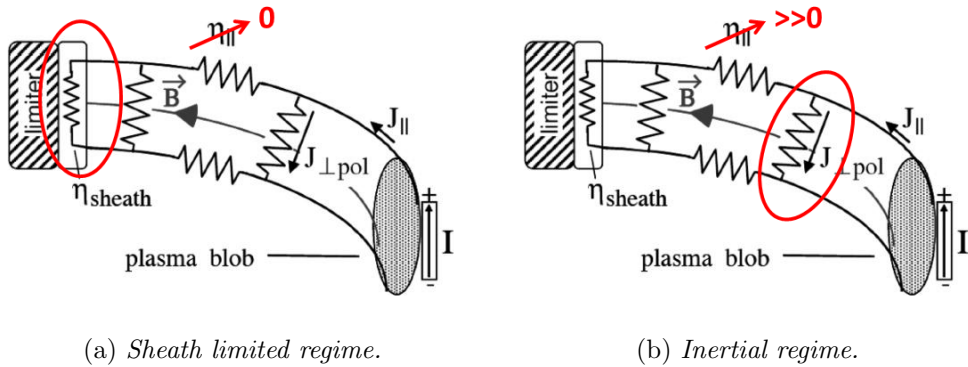


Figure 2.7: The closure scheme for the sheath limited regime (left) and the inertial regime (right) [7].

Considering in the equation realistic SOL condition such as hot ions and large

fluctuations amplitude, the filaments velocity in the sheath limited regime and in the inertial regime is respectively[12]:

$$v_b^{SL} = c_s(1 + \tau_i) \frac{L_c}{R} \cdot \frac{\tilde{n}}{\tilde{n} + \bar{n}} \left(\frac{\rho_s}{\delta_b} \right)^2 \quad (2.40)$$

$$v_b^{IN} = c_s \sqrt{(1 + \tau_i) \frac{L_c}{R} \frac{\tilde{n}}{\tilde{n} + \bar{n}} \frac{\delta_b}{R}} \quad (2.41)$$

τ_i is the ratio between ion and electron temperature, \tilde{n} is the filament density, \bar{n} the background density, δ_b the filament size and R the major radius of the tokamak.

The filament regime transition has been related to the effective local collisionality parameter in the scrape-off layer [13]:

$$\Lambda = \nu_{ei} \frac{\Omega_i L_c}{\Omega_e c_s} \quad (2.42)$$

ν_{ei} is the momentum loss frequency discussed in 2.28, $c_s \simeq \sqrt{\frac{T_e}{m_i}}$ is the sound speed, Ω is the cyclotron frequency and L_c is the connection length. Λ is the ratio between the characteristic parallel length and the electron-ion mean free path. When $\Lambda > 1$ the typical parallel time is longer than the electron-ion collision time. Recent observations show that likely the filament regime transition is determined by the effective collisionality at the divertor targets [14, 15]. It is defined using in equation 2.42 the temperature and density measured at the divertor targets and as connection length $L_c = \frac{1}{5} \pi R q_{95}$, where R is the major radius of the tokamak and q_{95} the safety factor [14, 15]. The position in the SOL of a filament evolves according to:

$$\frac{\partial x}{\partial t} = v_{\perp}^{fil} \quad (2.43)$$

where x represent the radial position of the filament respect to the separatrix. The time that a filament takes to travel from the separatrix to a radial position in the SOL can be express using equation 2.43:

$$\tau_{fil} = \frac{v_{\perp}^{fil}}{x} \quad (2.44)$$

at the midplane $x = R - R_{sep}$. If filaments undergo to a regime transition, namely they change from sheath limited to inertial regime, the transport related to them increases and may becomes dominant. The filament regime transition occurs in association with a change in the density profile in the whole SOL known as density shoulder formation [15].

2.6 Density shoulder in the scrape-off layer

The experiments carried out on different tokamaks such as JET, COMPASS and the ASDEX Upgrade tokamak [16], show a transition in the SOL density profiles as the density is increased. Recent experiments [14, 15] relate the shoulder

formation with an increasing of the filament related and provide a comprehensive experimental coverage of the SOL evolution across the transition in order to analyze simultaneously the changes at the outboard midplane perpendicular transport, turbulence characteristics, collisionality parameter Λ and the effect on the divertor to obtain a consistent picture of all the phenomena.

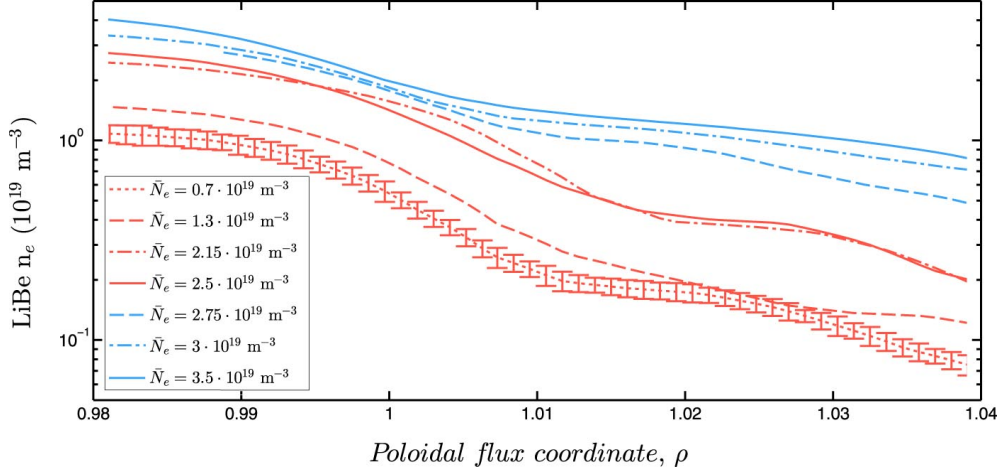


Figure 2.8: Evolution of radial density profiles for different line density averaged values \bar{N}_e . Red and blue lines represent profiles before and after the transition. Typical error bars are shown in one case as a reference.

Qualitatively, two kinds of profiles can be distinguished. The first one is characterized by a strong gradient in the vicinity of the separatrix, followed by a flat region towards the far SOL (blue curves in figure 2.8). The second kind lacks such a first gradient and displays a similar e-folding length in the whole scrape-off layer (red curves in figure 2.8).

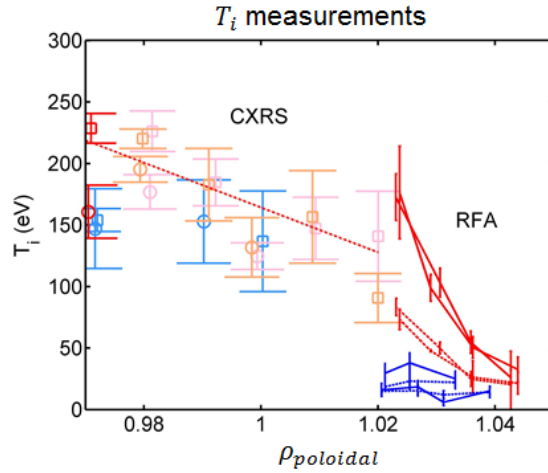


Figure 2.9: The ion temperature in the SOL. The measurements are performed by CXRS (the dots) and by midplane manipulator RFA probe (the solid and dashed lines). Solid lines represent the ions in the filament, dashed lines the plasma background ions [17].

In addition to the transition in the density profile a transition in the filament behavior is observed. In agreement with the model [18] the filaments undergo to a regime transition, when the divertor collisionality became greater than one. This transition occurs at the same density at which the density shoulder formation is observed. When the transition takes place filaments increase in size, density, velocity and the detection rate increase as well as the perpendicular transport related to the filaments [15]. Moreover after the shoulder formation the ions that compose the filaments and the ions in the plasma background are colder than before the shoulder formation. This is shown in figure 2.9 before the density shoulder formation (red curves) the ions are hotter than after the shoulder formation (blue curves).

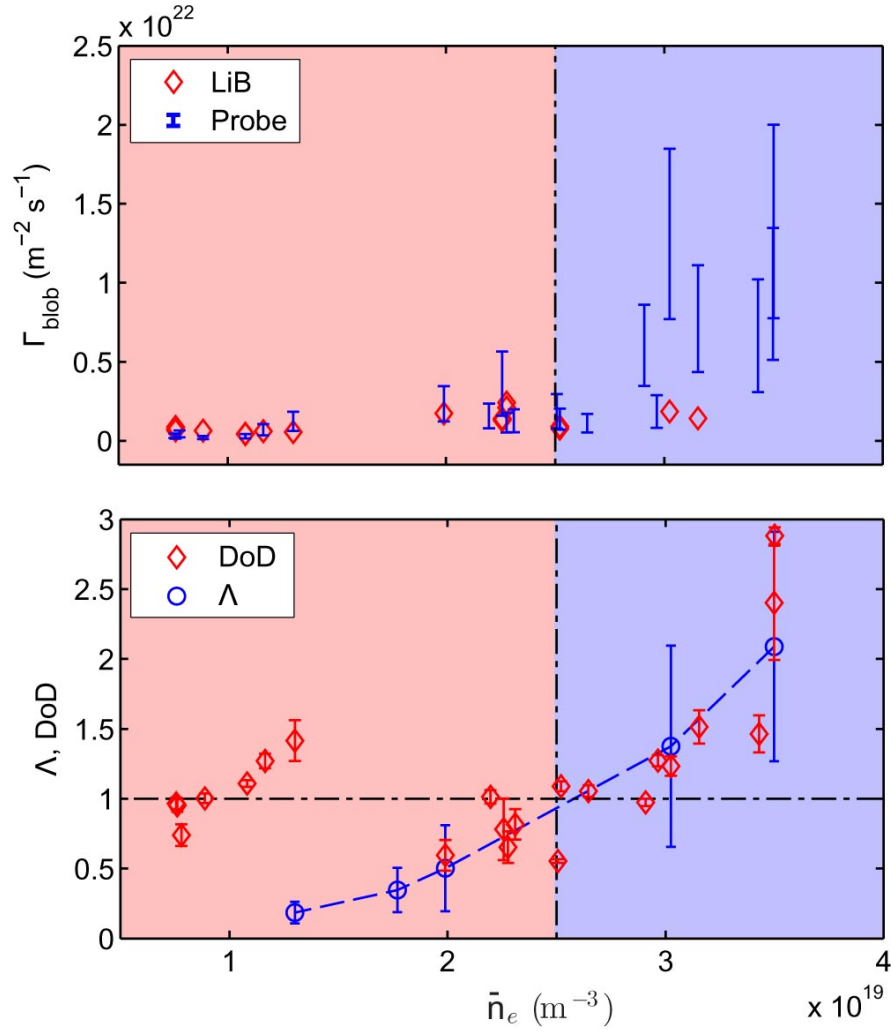


Figure 2.10: The plot on the top in the figure shows how the transport related to filament changes increasing the plasma density. The red and blue areas indicate before and after the shoulder formation. The plot in the bottom of the figure shows both the increase of the divertor collisionality and the degree of detachment (DoD) with the density.

Plot on the top of figure 2.10 shows the increase of convective transport related

to filaments is shown: it is about one order of magnitude and the sharp trend is consistent with the broadening of the profiles. It is calculated as:

$$\Gamma = v_{fil} \cdot n_{fil} \cdot f_{fil} \quad (2.45)$$

where v_{fil} is the filaments velocity, n_{fil} the filaments density and f_{fil} the filament fraction, namely the ratio between the time in which filaments are measured from the total measurement time. Plot on the bottom of figure 2.10 shows how the degree of detachment (namely DoD, a parameter that is high when the plasma is fully detached from the divertor and low when it is fully attached) changes increasing the density. This provides a relation between the filament transition and the detachment of the outer divertor targets.

Chapter 3

Experimental setup

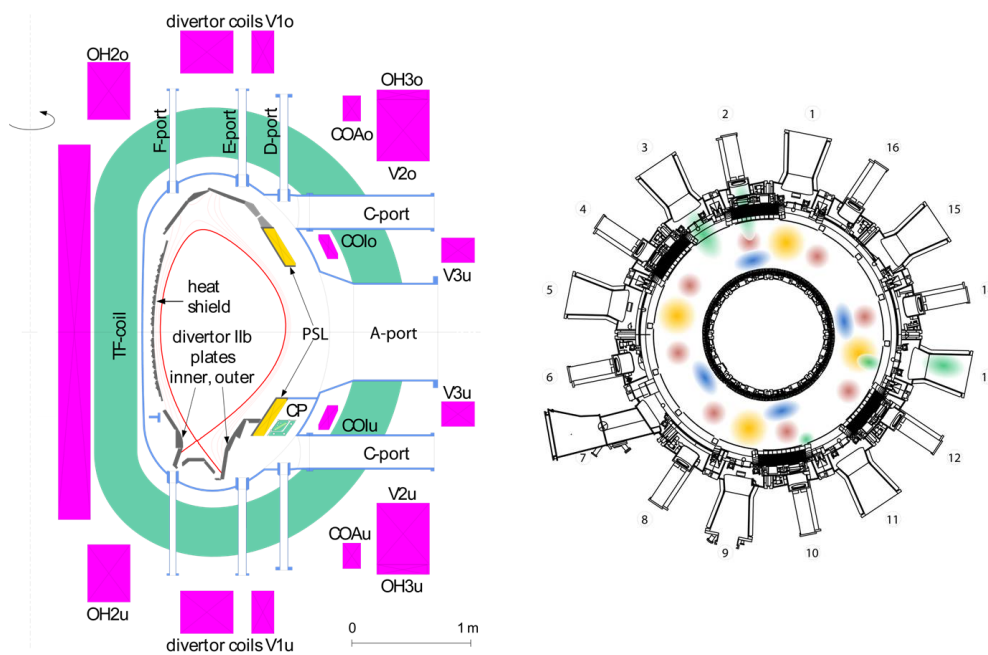
3.1 ASDEX Upgrade

ASDEX Upgrade (AUG) is a D-shaped Tokamak [19] with a plasma major radius $R_0 = 1.65 \text{ m}$ and a minor radius $a = 0.5 \text{ m}$. The toroidal magnetic field is 2.5 T and a typical plasma current in the order of 1 MA . The plasma inside AUG has a maximum density of $n_e = 3 \cdot 10^{20} \text{ m}^{-3}$.

The Toroidal magnetic field is generated by a system of sixteen toroidal coils made of an alloy of copper and silver, that generate a magnetic field of $4,65 \cdot 10^{-2} \text{ T kA}^{-1}$. Alongside of the toroidal coils a system of coils that generate a poloidal magnetic field is present. Three different groups of coils can be distinguished according to their purpose:

- Five ohmic heating coils used to drive the plasma current used to heat the plasma (OH- coils in figure 3.1 left);
- Eight coils used to control the plasma shape and achieve the divertor configuration (V- coils in figure 3.1 left);
- Six coils used to correct the plasma position and reduce the instabilities (PLS and C- coils in figure 3.1 left).

Two of the coils (PLS) of the last group are placed inside the vacuum vessel. The vessel of ASDEX Upgrade is a rigid self supporting structure composed of 16 wedge-shaped segment of D-shaped cross-section. The vessel is provided with ports trough which different diagnostics as well as plasma heating components and pumping system are inserted. The heat shield, i.e. the surface covering the inner column, the divertor targets and the other plasma facing components are located inside the vacuum vessel. Two limiters are positioned in order to reduce the interaction between the plasma and the vessel wall. These components and the divertor targets are the ones that interact with the plasma in the scrape off layer (figure 3.1). In AUG all of the plasma-surface interacting materials are made of tungsten, every two weeks during the operations periods a deposition of a thin layer of boron is performed in order to reduce the tungsten impurities generation.



(a) *ASDEX Upgrade poloidal cross section.* (b) *ASDEX Upgrade toroidal projection.*

Figure 3.1: On the left a picture of a poloidal section of AUG. In light blue the vessel and the ports. In green the Toroidal field coil. In fuchsia the poloidal field coils. In gray the heat shields and the divertor targets. The red solid line is the separatrix. [20]. The picture On the right shows the position of the gas valves in a toroidal projection of AUG and the cloud of gas pump thrown them in the torus.

The neutral gas needed to ignite the plasma is provided by two different systems: gas valves and pellet injection. The gases used normally in AUG are hydrogen, deuterium and helium. The gas valves are spread all over the main chamber (figure 3.1 right). The valves set in the divertor region can be used to inject nitrogen in order to increase the radiation and cool down the plasma that interact with the wall. The other way to supply gas is via the pellet injection system, that injects high purity solid tablets of different gases of a size from 2.94 mm^3 up to 7.22 mm^3 .

The plasma generated in the main chamber is heated through:

- Ohmic heating: the current that flows toroidally heats up the plasma that behaves like a resistance. Since such resistance is related to collisions this effect is relevant only for low power discharges;
- Electron cyclotron resonance heating (ECRH), ion cyclotron resonance heating (ICRH): RF waves deposit energy into the plasma with a resonance in electron or ion cyclotron frequency;
- Neutral beam injector: a beam of high energy neutral particles is injected into the plasma. These particles are not affected by the magnetic field an

reach the core, where thanks to charge exchange and ionization collisions they become energetic ions.

The maximum combined heating power is 23 MW and the peak temperature achieved is 3 keV , while typical core temperatures are of the order of 1 keV .

3.2 Diagnostics

3.2.1 Lithium beam

The lithium beam diagnostic (LiB) is based on the observation of the spectral line Li I (transition $Li_{2p} \rightarrow Li_{2s}$, $\lambda = 670.8\text{ nm}$) from neutral lithium atoms injected with an energy of $30 - 80\text{ keV}$ into the plasma. The measured emission profiles are modeled with a collisional-radiative model which include electron impact excitation, ionization and charge exchange processes. A system of coupled linear differential equations describes the occupation densities of excited states of Li [21]:

$$\begin{cases} \frac{dN_i(x)}{dx} = \sum_{j=0}^{N_{L_i}} n_e(x) a_{ij}(T_e(x)) + b_{ij} N_j(x) \\ N_i(x=0) = \delta_{1i} \end{cases} \quad (3.1)$$

where x is the coordinate along the injected lithium beam and $x = 0$ defines the entrance of the lithium beam into the plasma (first measured channel); N_i is the occupation density for the i -th energy level, N_{L_i} the total number of occupation levels. Attenuation of lithium state i , which is due to charge exchange ionization and excitation and de-excitation to any other bound state, is described by coefficient a_{ij} . The coefficients b_{ij} are the Einstein coefficients of spontaneous emission. n_e and T_e are the electron density and temperature, respectively. At $x = 0$ the lithium atoms are assumed to be in ground state where the boundary condition has to be fulfilled.

3.2.2 Edge Thomson scattering diagnostic

Due to the great difference in mass between ions and electrons, electro-magnetic radiation in a plasma is mainly scattered by the light electrons. In a fusion plasma, which is fully ionized, the radiation is scattered by unbounded electrons (Thomson scattering) and not by bounded electrons (Rayleigh scattering).

The scattering of monochromatic light by a moving electron leads to a spectral shift of the scattered radiation due to the Doppler effect. Since the Doppler shift depends on the velocity vector of an electron, an ensemble of electrons with a velocity distribution generates a broad spectrum of scattered light.

The plasma property which is measured by Thomson scattering depends on the scattering vector \vec{k} , which is the difference between the wave vectors of the incoming and scattered light, and the Debye length λ_d of the plasma: For $k\lambda_d < 1$ the collective effects of the plasma, like plasma waves associated with the ion motion, determine the scattered spectrum. For $k\lambda_d > 1$ the uncorrelated motion of the electrons contributes to the scattered radiation, since any collective plasma effects which have correlation lengths larger than the Debye length do

not contribute to the scattered radiation because of destructive interference. In this case the number of scattered photons is proportional to the number of scattering electrons and the spectral shape of the scattered radiation is determined by the velocity distribution of the electrons. By measuring both the amount of scattered photons and their spectral distribution the electron density and their velocity distribution can be determined. For electrons with a Maxwellian velocity distribution a simple diagnostic setup can be used for measuring the electron temperature. Figure 3.2 shows a schematic example of how a monochromatic radiation is scattered by the electrons.

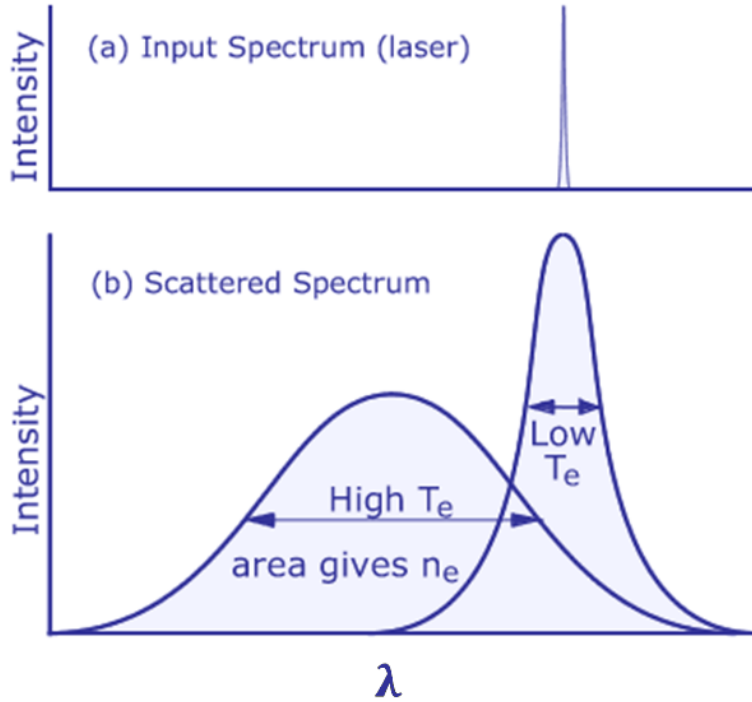
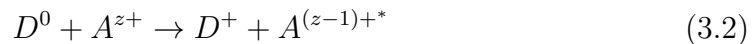


Figure 3.2: An example of emission profile broadening due to the Thomson scattering.

3.2.3 Edge charge-exchange recombination spectroscopy

Charge-exchange recombination spectroscopy (CXRS) is based on the observation of the light emitted by impurities. The neutrals that are injected to heat the plasma exchange their charge with the different ions present in the plasma.



where D represent the deuterium and A an impurity atom. When charge-exchange process takes place the plasma ion cascades to the ground state and emits a characteristic radiation line by which statements about speed, temperature and density of the observed particles can be retrieved. Normally impurities species such as boron and nitrogen are considered as acceptors. Since this kind of charge-exchange processes take place along the trajectories of the neutral beams,

CXRS can be used for spatially resolved measurement. The impurities are nearly at the same temperature of the plasma deuterium ions. The particle velocity leads to a Doppler broadening $\Delta\lambda$ of the charge-exchange spectral line, from which the ion temperature can be determined [22]:

$$\Delta\lambda = \frac{2\lambda}{c_0} \sqrt{2\ln 2 \frac{k_B T_i}{m_i}} \rightarrow T_i = \left(\frac{\Delta\lambda c_0}{2\lambda} \right)^2 \frac{m_i}{2\ln 2 k_B} \quad (3.3)$$

where λ is the unperturbed wavelength of the emitted radiation, $\Delta\lambda$ the Doppler shift that is measured, m_i the mass of the ions and T_i the ion temperature.

3.2.4 Manometers

Ionization pressure gauges measure the flux density of the neutrals. In this type of manometers a regulated electron current (between $200 \mu A$ and $600 \mu A$) is emitted from a heated filament. Then the electrons, emitted due to thermionic effect, are attracted to grid by a DC potential. Most of the electrons pass through the grid, and collide with the background gas molecules in the enclosed volume, causing the ionization of a fraction of them. These ions are then attracted by a central collector wire due to its negative polarization. The number of created ions is proportional to the gaseous molecule density and the electron current emitted from the filament. The flux of particles can be found as[21]:

$$\Phi_n = d \frac{I_{ion}}{I_{electron} - I_{ion}} \quad (3.4)$$

where d is the calibration coefficient, depending on the gas type. The gas density could be estimated as:

$$n_n = 4 \frac{\Phi_n}{\sqrt{\frac{8k_b T}{\pi m_n}}} \quad (3.5)$$

where T is the neutral particles temperature and m_n the neutral particles mass.

3.2.5 Langmuir probes

A Langmuir probe is a device composed by one or more conductor electrodes, it is inserted into the plasma and collects a current that is used to determine the electron temperature, electron density, and electric potential of the plasma.

Electrons have a much higher mobility than ions so a probe pin inserted into the plasma will be charged up negatively, resulting in the creation of the so-called Debye sheath. Inside the sheath the quasi neutrality is violated and the particles motion is dominated by the electric potential of the probe. Moreover no sources (such as ionization) are present inside the sheath since the sheath width is negligible respect to the characteristic length of such processes. This means that the perpendicular flux in the sheath is equal to that at the entrance of the layer. By solving the set of equation provided by ion continuity, the ion energy conservation and the Poisson's equation and assuming the Boltzmann distribution

for electrons, uncollisional plasma and not magnetized plasma, a lower limit for the ion velocity at the entrance of the sheath is [23]:

$$v_i = \frac{kT_e}{m_i} \simeq c_s \quad (3.6)$$

this is known as Bohm criterion. Solving the same equation in the region before the Debye sheath, so under the assumption of quasi neutrality the current collected by the probe is found. The probe current depends on the plasma conditions in the region before the sheath and the probe potential [23]:

$$I_{probe} = -A_{probe} j_{sat_i} \left(1 - e^{\frac{e(V_{probe} - V_f)}{k_b T_e}} \right) \quad (3.7)$$

In equilibrium the probe is at a fixed potential, called floating potential (V_f), and the current flowing into the probe is zero. A_{probe} is the collecting area of the probe, V_{probe} is the probe potential and j_{sat_i} the ion density saturation current: when the probe pin is biased, the plasma reacts shielding the perturbation. At enough negative potential all the ions inside the Debye sheath reach the probe and the ion saturation current density is measured:

$$j_{sat_i} = eZn_i c_s \quad (3.8)$$

where Z represents the charge number of the ions. The plasma density is calculated from the ion density saturation current. By increasing the potential more electrons are collected and the current increases then the slope of the I-V characteristics in a logarithmic plot gives the electron temperature:

$$T_e = \frac{e(V_{probes} - V_f)}{k_b} \left(\ln \left(1 + \frac{I_{probe}}{I_{sat_i}} \right) \right) \quad (3.9)$$

If the probe potential is increased further, the electron saturation current is collected near the plasma potential. It can be calculated from kinetic theory supposing a maxwellian distribution for the electrons

$$j_{sat_e} = \frac{1}{4} en_e \sqrt{\frac{8k_b T_e}{\pi m_e}} (1 - \gamma_e) \quad (3.10)$$

γ_e is the factor that describe the secondary electron emission at the probe surface (0.4 - 0.6 for $Te < 100 eV$). The electron saturation current regime is normally avoided because the collected current usually is so high that the probe may be damaged.

The effective area of a Langmuir probe is the most significant uncertainty of the measurement. The presence of the magnetic field oblige the charged particles to gyrate around the field lines therefore electrons and ions can only stream along a field line and the cross field transport is strongly suppressed before the sheath. In this system the effective area of the Langmuir probe is the projection of the probe area on the field lines. The Langmuir probes used in a modern Tokamaks have to withstand strong thermal loads. As a result this kind of diagnostics can

be used only in the scrape off layer and at the divertor. Even in these relatively cold regions (compared to the core where the electron and ion temperature are much higher) the thermal loads can damage the probes. In order to preserve the probes special designs characteristics have been developed:

- Moving probes: the probes move in and out with a constant time, the exposition time is small enough to avoid the overheating of the probe pin.
- Heat sink probe: a small probe tip is in thermal contact with a big cooled heat sink.
- Flush mounted probes: the surface of the probe is aligned with the surrounding wall so it can withstand the same power deposition that the wall sustains. These probes are only employed in material surfaces which are exposed to the plasma

3.2.6 Diagnostics arrangement in ASDEX Upgrade

In figure 3.3 the positions of the diagnostics discussed in ASDEX Upgrade are shown.

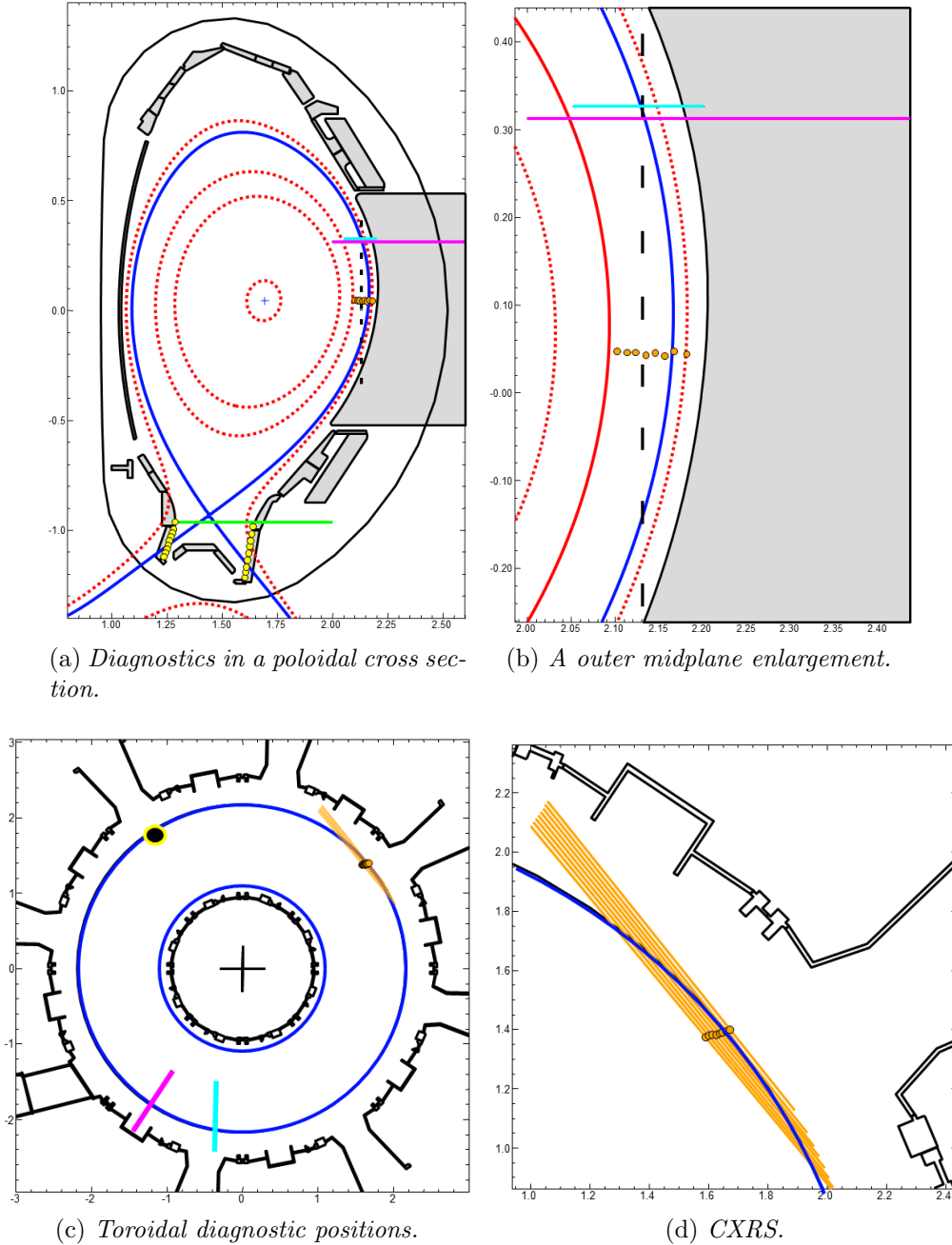


Figure 3.3: In (a) the diagnostics position in a poloidal section of AUG. In magenta the MPM, in green the XPR, in yellow the probes in the divertor, in orange the toroidal CXRS, in black the TS, in cyan the LiB. In (b) an enlargement of the midplane. In (c) the toroidal position of the probes. In magenta the MPM, in orange the toroidal CXRS for which are plotted the lines of sight, the black dot with yellow boarder is the TS, in cyan the LiB. In (d) an enlargement of the CXRS diagnostic with the lines of sight.

The lithium beam injector in ASDEX Upgrade is located in sector 9 at $z = 0.326\text{ m}$ above the equatorial midplane of the torus (figure 3.3). The radiation emitted by the lithium is collected by an array of 35 lines of sight then the spectra allows to reconstruct the electron density profiles along the lithium beam. Figure 3.4 shows how the lithium beam injector and the lines of sight are arranged in the vacuum vessel of ASDEX Upgrade.

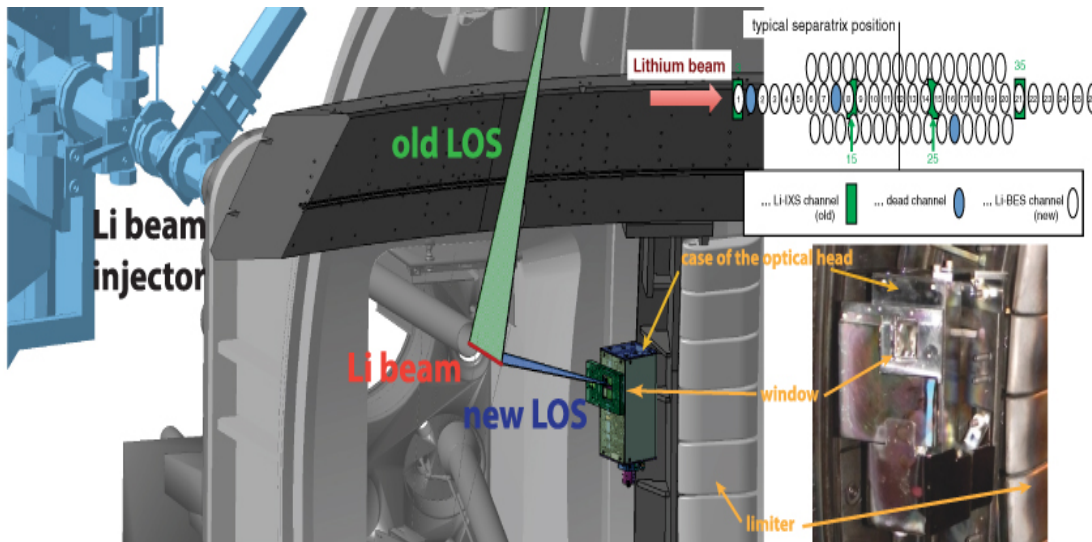


Figure 3.4: Left the CAD design of the lithium beam system. Right in the picture can be distinguished the beam of neutral particle, the two lines of sight, the optical head and the different channel [24].

The spatial resolution of the system is $\Delta R = 5\text{ mm}$ while the temporal resolution is $50\ \mu\text{s}$ [24]. The emitted radiation is filtered in order to measure only the emission related to the $Li_{2p} \rightarrow Li_{2s}$ transition the signal is amplified by a photomultiplier. Since the filter collects also photons originated from different transitions the beam is chopped to allow background subtraction. The photomultiplier requires a calibration this is usually performed: during the pause between two shots when only homogeneous neutral gas is present inside the main chamber: then each channel must see the same signal and this allows the calibration of the lithium beam diagnostic [24].

Two different system of Thomson scattering diagnostics are available in ASDEX Upgrade: one is dedicated to study the core region and the other one is dedicated to study the SOL region, only the latter is used in this work and it is composed of sixteen channels vertically arranged and spaced by 2 mm (figure 3.3). For achieving an acceptable signal-to-noise ratio a pulsed high power laser is used as monochromatic light source. The vertical Thomson scattering system (TS) in ASDEX Upgrade is equipped with a cluster of six lasers with a repetition rate of 20 Hz each. More details in [25, 26].

In AUG the light emitted by charge exchange processes is measured by three different systems: toroidal core, poloidal edge, toroidal edge. Where poloidal and toroidal, core and edge indicate the direction of the lines of sight and regions they look to respectively. The one used for this work is the toroidal edge CXRS

system (figure 3.3). The system observes a wavelength interval of 13.1 nm at a central wavelength of 494.5 nm . The entrance slit of the spectrometer is typically set to $100\ \mu\text{m}$, but can be adjusted to any value between 0 and $400\ \mu\text{m}$. For the edge diagnostic, the entrance slit of the spectrometer is typically set to $50\ \mu\text{m}$. The system commonly analyzes the $B^{5+}(n = 7 \rightarrow 6)$ CX spectral line at 494.467 nm , but it is possible to evaluate also the $N^{7+}(n = 9 \rightarrow 8)$ CX spectral line at 566.937 nm as well (like in figure 3.5). In figure 3.5 an example of measured spectrum is shown, the active (N^{7+}) and passive (N^+) lines are fitted with gaussian functions, the active line provided the informations needed to obtain the T_i . The toroidal edge system uses an in-vessel optical head, which resolves the plasma edge at the outer midplane using eight lines of sight. These LOS are pointed at the center of the neutral beam injector placed in sector 15 (figure 3.3 c). Each line of sight is separated from the next one by about 1 cm and is equipped with three optical fibers (with a diameter of $400\ \mu\text{m}$). The radial profile can be obtained by moving the plasma position by 2 cm in about 800 ms during a steady-state stage of the discharge and by mapping the measurements onto the plasma coordinate system ρ . This increases the radial resolution up to 3 mm .

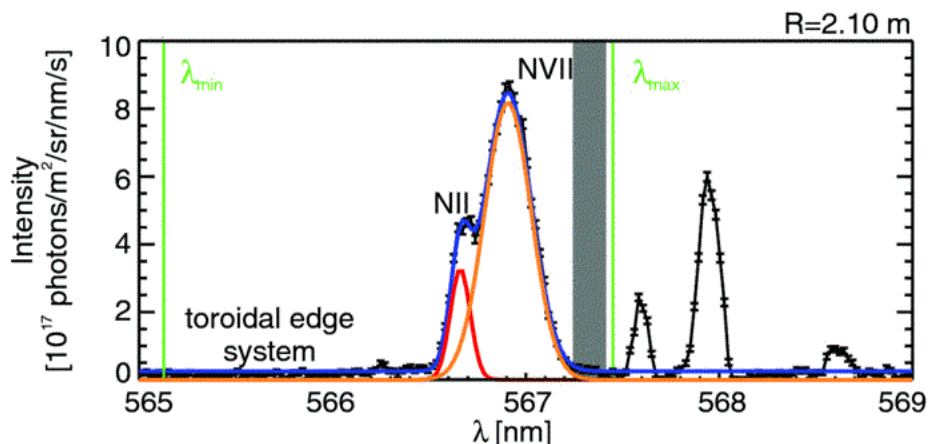


Figure 3.5: A typical spectra of the toroidal edge CXRS diagnostic. The figure shows the N^{6+} and the N^+ lines. These two are fitted with two different Gaussians (red lines). The blue line is the sum of the two fitted function. Black data the measured radiation intensity. The data lower then λ_{min} , greater then λ_{max} and inside the gray region are not used for the fit [27].

In this work moving probes are used to study the outer midplane and the X-point. The Langmuir probes are fixed on a solid carbon probe head mounted on the reciprocating midplane manipulator (MPM). It penetrates the plasma horizontally from the low-field side of about 30 cm above the outer midplane with a speed of about 1 m s^{-1} (figure 3.3). The Langmuir probes are fixed on a carbon head (figure 3.6). Fourteen probe tips are embedded on three different levels in a carbon block. The cylindrical carbon tips have a radius of 0.45 mm and a length of 2 mm . These small free standing probe tips minimize the perturbation due to the presence of the probes, but may easily burn if the power load exceeds a certain limit. The tips that measure the ion-saturation current were biased to

$-180V$ with respect to the vacuum vessel to ensure that the ion saturation regime is reached even at negative plasma potential and high temperature close to the separatrix. Probe current and voltage signals are recorded with an acquisition rate of $2 MHz$ [28].

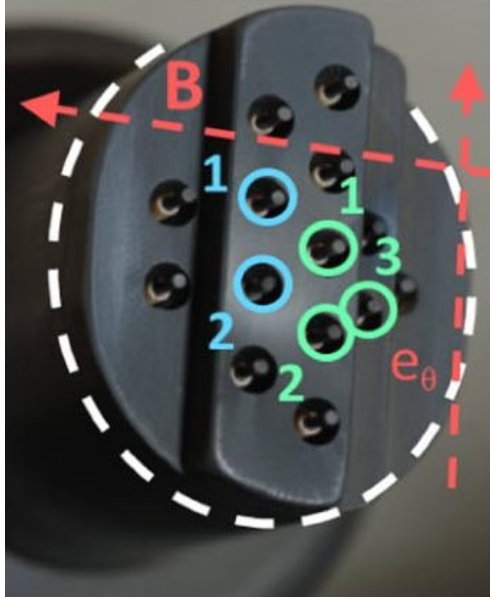


Figure 3.6: A picture of the probe. The red dashed lines indicates the parallel and normal directions. The green and blue pins are used to measure ion saturation current and floating potential.

The X-point manipulator (XPR) is installed at $z = -0.996m$ and reciprocates horizontally through the divertor entrance, falling below the X point by about $2 - 5 cm$. The probe head is equipped with three graphite pins, that measure T_e and I_{sat} . The acquisition rate is $100 kHz$ [29].

In addition Langmuir probes are installed to measure T_e and n_e at the inner and outer divertor (figure 3.3). These probes are flush mounted in the tiles of the inner and outer divertors and have typical dimensions of $25 mm$ in the toroidal direction and $4 mm$ in the poloidal direction. The acquisition rate is $33 kHz$.

The position of the manometers in ASDEX Upgrade is shown in figure 3.7.

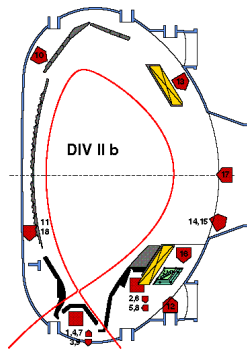


Figure 3.7: The picture shows the position of the manometers in a poloidal section.

Chapter 4

EMC3-Eirene code

In order to properly describe the SOL condition a set of equation that consider all the different particles present is needed: plasma particles, neutral particles and impurities, that may be important in this region. Among all the different models that describe the SOL, the one that is used in this work is the fluid model provided by the Braginskii's equations. In each elements of volume dV must be valid [30]:

$$\vec{\nabla} \cdot (n_i v_{i||} \hat{b} - D_{\perp} \bar{\bar{b}}_{\perp} \cdot \vec{\nabla} n_i) = S_p \quad (4.1)$$

$$\vec{\nabla} \cdot (m_i n_i v_{i||} v_{i||} \hat{b} - \eta_{||} \bar{\bar{b}} \cdot \vec{\nabla} v_{i||} - D_{\perp} \bar{\bar{b}}_{\perp} \cdot \vec{\nabla} m_i n_i v_{i||}) = -\hat{b} \cdot \vec{\nabla} p + S_m \quad (4.2)$$

$$\frac{m_Z n_Z}{\tau} (V_{Z||} - v_{i||}) = -\hat{b} \cdot \vec{\nabla} n_Z T_Z + n_Z Z e E_{||} + n_Z Z^2 C_e \hat{b} \cdot \vec{\nabla} T_e + n_Z C_i \hat{b} \cdot \vec{\nabla} T_i \quad (4.3)$$

$$\vec{\nabla} \cdot \left(\frac{5}{2} n_e T_e v_{i||} \hat{b} - \kappa_e \bar{\bar{b}} \cdot \vec{\nabla} T_e - \frac{5}{2} T_e D_{\perp} \bar{\bar{b}}_{\perp} \cdot \vec{\nabla} n_e - \chi_e n_e \bar{\bar{b}}_{\perp} \cdot \vec{\nabla} T_e \right) = -k(T_e - T_i) + S_{ee} \quad (4.4)$$

$$\vec{\nabla} \cdot \left(\frac{5}{2} n_i T_i v_{i||} \hat{b} - \kappa_i \bar{\bar{b}} \cdot \vec{\nabla} T_i - \frac{5}{2} T_i D_{\perp} \bar{\bar{b}}_{\perp} \cdot \vec{\nabla} n_i - \chi_i n_i \bar{\bar{b}} \cdot \vec{\nabla} T_i \right) = +k(T_e - T_i) + S_{ei} \quad (4.5)$$

$$T_Z = T_i \quad (4.6)$$

where \hat{b} is the unitary vector for the magnetic field lines, $\bar{\bar{b}}_{\perp}$ is the tensor that points the direction perpendicular to the magnetic field lines, $\bar{\bar{b}}$ is the tensor parallel to the magnetic field lines and is such as $\bar{\bar{b}}_{\perp} = \bar{\bar{I}} - \bar{\bar{b}}$ where $\bar{\bar{I}}$ is the unit tensor.

Equation 4.1 describes the density mass balance for all the plasma species and the impurities, the \hat{b} is the transport along a field line, while the $D_{\perp} \bar{\bar{b}}_{\perp}$ is the cross field transport. This is a diffusive component. S_p is the source of particles in the volume and is the balance between recombination and ionization.

Equation 4.2 is the momentum balance for main ion species, the first term of the left hand side of the equation stands for the momentum transport along a field line. The second one represents the viscosity: the friction between two plasma columns with different velocities reduces the difference between them. The last term is the momentum transport in the perpendicular direction. On the right hand side of the equation the first term is the pressure force and S_m summarizes all the possible momentum sources and losses such as charge exchange processes.

Equation 4.3 describes the momentum balance for the impurities. Z is the

impurity charge number. The term on the left hand side stands for the friction between ions and impurities. The first term in the right hand side is the parallel momentum transport, the second describes the gain of momentum related to the parallel electric field, that is created by the electrons and can be determined by the parallel momentum balance for the electrons $-\hat{b} \cdot \nabla n_e T_e + n_e e E_{\parallel} + n_e C_e \hat{b} \cdot \nabla T_e = 0$. The last two terms are the thermal forces. The impurities are supposed to be at the same temperature of the plasma ions (equation 4.6).

Equations 4.4 and 4.5 are the energy balance for the plasma species: ions and electrons. Each particle transports an energy of $\frac{5}{2}T_e$ (or T_i), so the parallel component of equation 4.1 leads to a convective energy transport along the field lines. That is taken in account by the first and the third terms of the left hand side of the equations. The second term describes the parallel heat conduction and k_e/k_i are the conduction coefficients. The last term of the left side is the energy cross field diffusion. On the right side of the equation the energy exchanged between the plasma species and S_{ee} , S_{ei} summarize all the energy sources and losses such as external heating and radiation.

In this work the EMC3-Eirene code has been used. The EMC3-Eirene code is composed of two different Monte Carlo codes: EMC3 solve the Braginskii's equations for plasma particles (equations from 4.1 to 4.6) by simulating the plasma behavior and it is self-consistently coupled to EIRENE that solves the kinetic equation for neutrals (equation 4.7).

$$\left(\frac{\partial}{\partial t} + \hat{v} \cdot \nabla_{\hat{r}} + \frac{\hat{F}(\hat{r}, \hat{v}, t)}{m} \cdot \nabla_{\hat{v}} \right) f(\hat{r}, \hat{v}, t) = \left(\frac{\partial f}{\partial t} \right)_{coll.} \quad (4.7)$$

where f is the probability density function, \hat{r} and \hat{v} spatial coordinates and velocity respectively. $\frac{\partial f}{\partial t}$ stands for the changes in the pdf due to collisions.

The Braginskii's equations can be generalized in the form [30]:

$$\nabla \cdot (\hat{v} f - \overline{\overline{D}} \hat{\nabla} f) = S \quad (4.8)$$

where $\overline{\overline{D}} = D_{\parallel} \overline{\overline{b}} + D_{\perp} (\overline{\overline{I}} - \overline{\overline{b}})$ is the diffusive tensor and \hat{v} , D_{\parallel} , D_{\perp} and S are the transport coefficients and the source term respectively for the quantity f . Equation 4.8 can be treated as a stochastic process that obeys to a transition probability function. This can be solved numerically, a round of false particle are generated and followed along the field line. They distribution will follows the probability distribution of the f quantity. The number of numerical particle in each position will be proportional to the physical f quantity in that position. To solve the equation a high accuracy in the magnetic field used by the code is needed. However field line integration is a rather time-consuming process, so it is replaced by an interpolation from a source given as input to the code. The details about the interpolation can be found in [31].

The crucial elements, for what concerns this work, are the input plasma parameters: the average density at the separatrix, the heating energy for electrons and ions as well as the cross field transport coefficients (χ_e , χ_i and D). The average density at the separatrix is kept constant during the iterations, the heating

energy is the initial energy for electrons and ions while the perpendicular transport coefficients in this work are considered as fitting parameters, namely values that must be found in order to properly simulate the plasma conditions.

The code does not take into account every physical process, in particular volumetric recombinations and radiative emissions. On the other hand EMC3 allows to calculate the interaction between the plasma and all the PFCs, whose role is crucial in the scrape-off layer.

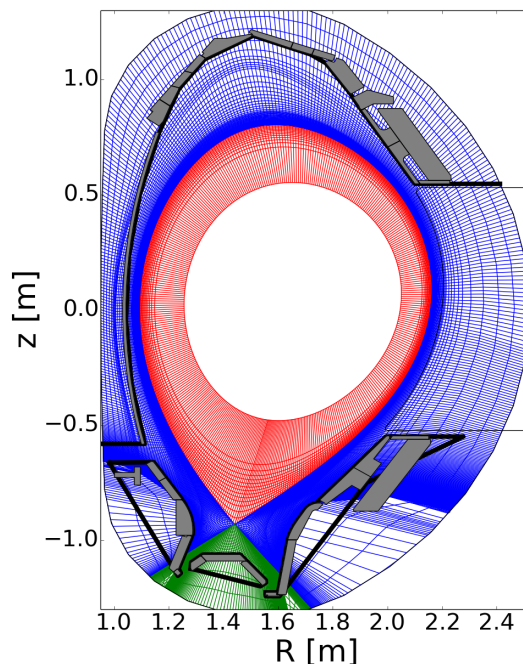


Figure 4.1: The grid in a poloidal cross section of ASDEX. In red the core grid, in blue the SOL grid and in green the private flux region grid. The solid black lines are the toroidal symmetric components as are seen by the code while the gray are the real ones.

The interaction can be considered on the code by means of a specific grid that allows a misalignment between the magnetic surfaces and the grid itself: in this way the PFCs, that are not aligned with the field lines, can be considered. Moreover the grid is characterized by a 3D-shape that allows to consider PFCs without a toroidal symmetry. The grid is based on the experimental facility that is studied: in this case Asdex Upgrade. The case for this work is shown in figure 4.1. Three different zones can be distinguished: the core region inside the separatrix, the SOL region and the private flux region. The core extends from $\rho = 0.9$ to $\rho = 1.0$ while the SOL region from $\rho = 1.0$ to $\rho = 1.15$. The grid extends from $\phi = 0^\circ$ to $\phi = 180^\circ$ and it is aligned to the magnetic field for almost its extension: the last aligned flux surface is $\rho = 1.13$. The grid is described by a vector $\hat{G}_{[ir,ip,it]}$ that points to a cell position: ir is the radial index, ip the poloidal index and it the toroidal one. Since the grid is aligned to the magnetic field it is

true that:

$$\vec{B} = |B| \frac{\vec{G}_{[ir,ip,it]} - \vec{G}_{[ir,ip,it+1]}}{|\vec{G}_{[ir,ip,it]} - \vec{G}_{[ir,ip,it+1]}|} \quad (4.9)$$

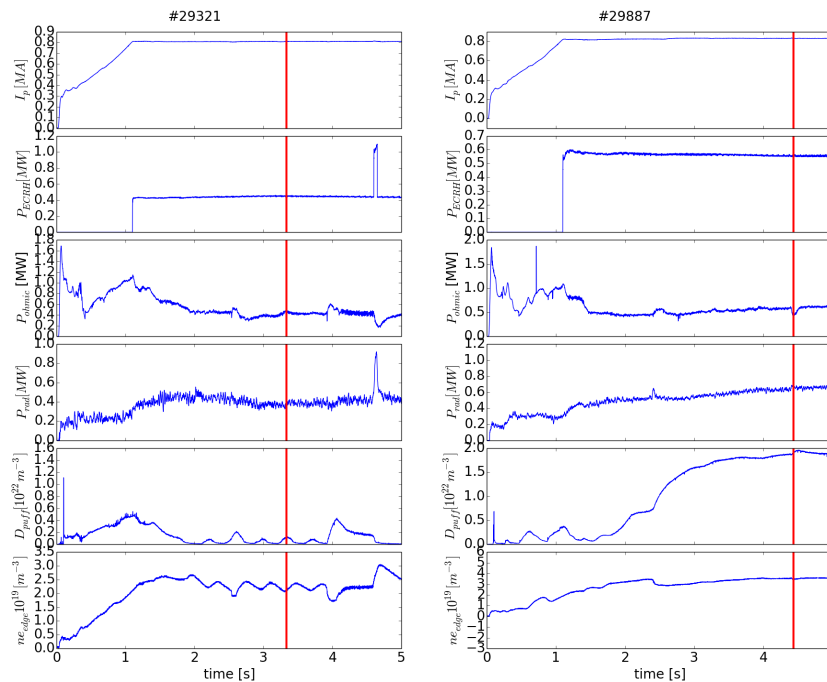
The plasma components considered are modeled as closed volumes (see figure 4.1). The heat shield limiters intersect the grid at $\phi = 19^\circ$ and $\phi = 64^\circ$. The ICRH limiters are positioned at $\phi = 85^\circ$, $\phi = 108^\circ$, $\phi = 130^\circ$ and $\phi = 154^\circ$. All the PFCs are considered to be made of tungsten as well as in the real machine.

A run of the code is a sequence of several iterations. Each iteration starts from the results provided by the previous one and sum its result to initial parameters weighted by the relaxation factor: $f_{i+1} = Rf_i + (1 - R)f_{i+1}$, where f_i stands for the results of the i -th iteration and R is the relaxation factor. After an iteration the code calculates the averaged difference between the starting parameters and the results. A run can be considered as converged when the averaged difference is constant. A too high value of this parameter means that the simulation is oscillating and so it do not converge. Anyway these values must be handled with care: if a region is affected by a strong fluctuation and all the others have almost constant values, the averaged difference does not indicate the lack of convergence on that point. In addition to that the simulation convergence behaves differently according to the divertor temperature: the lower the divertor temperature the worse convergence.

Chapter 5

EMC3-Eirene simulations

The aim of this chapter is to provide a realistic simulation for the two discharges at different degrees of shoulder formation. The code used for the simulation is EMC3-Eirene described in chapter 4. In particular in one discharge no shoulder is observed while in the second one the shoulder forms. The filament-related transport, that affects the outer midplane, is likely responsible for the transition and it is approximated as diffusive transport by means of the perpendicular transport coefficients (D_{\perp} , χ_{\perp}^e , χ_{\perp}^i).



(a) *Case A.*

(b) *Case B.*

Figure 5.1: Main parameters for the two discharges. From top to bottom the plasma current, the ECRH heating power, the ohmic heating power, the radiation power, the deuterium gas puff into the machine, the edge density. The red lines represent the time considered for the simulations.

The two different discharges studied are the discharges 29321 and 29887 performed on ASDEX Upgrade. In the rest of this chapter these shots will be referred to as case A and case B respectively. Figure 5.1 shows the time evolution of the plasma current, input power and radiation power, gas puff and endge density for the two cases. The time consider is 3.334 s for case A and 4.440 s for case B. At that time the toroidal magnetic field is $B_T = -2.5 T$ at the magnetic axis and the plasma current is $I_p = 0.8 MA$ for both discharges. The total deuterium gas puff in the machine is $0.1 \cdot 10^{22} m^{-3}$ and $1.9 \cdot 10^{22} m^{-3}$ for case A and B, respectively. The heating systems used in these discharges are ohmic heating ($P_{ohmic} = 500 kW$) and electron cyclotron heating ($P_{ECRH} = 440, 550 kW$ respectively). The density in the case A is lower than in case B, the edge line density is $\bar{n}_e = 2.2 \cdot 10^{19} m^{-3}$ and $\bar{n}_e = 3.5 \cdot 10^{19} m^{-3}$ respectively. The magnetic configuration of the two discharges is shown in figure 5.2. No shoulder is observed in case A and the plasma is partially detached from the inner divertor target and totally attached to the outer divertor target. On the contrary in the case B it is observed the density shoulder and the inner divertor is in a fully detached condition, while the outer divertor is partially detached. At the time of interest the position of the heat shield limiter magnetic surface is $\rho = 1.55$ and $\rho = 1.038$ respectively, while the ICRH limiter is at $\rho = 1.67$ and $\rho = 1.047$ respectively (figure 5.2).

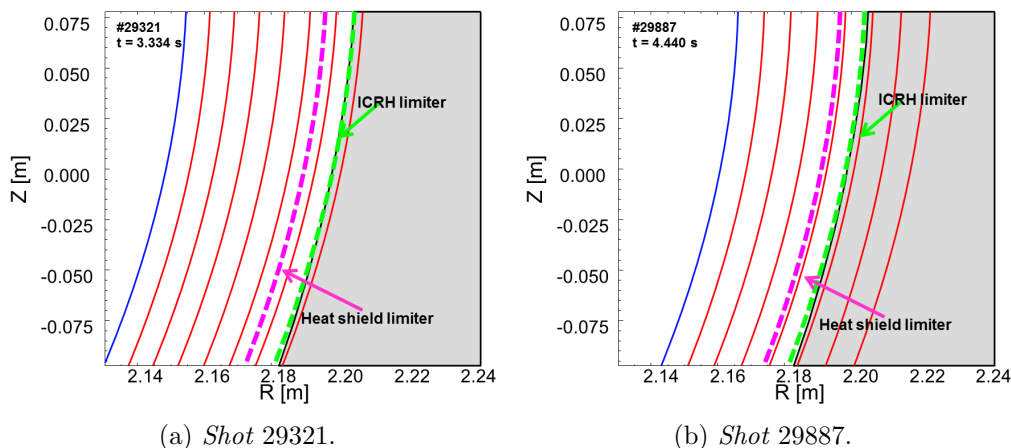


Figure 5.2: Comparison between the magnetic configuration at the midplane for shot case A (left) and case B (right). The plots show: the separatrix (blue solid line); magnetic surface from $\rho = 1.01$ to $\rho = 1.07$ (red solid lines); the heat shield limiter surface (magenta dashed line) and the ICRH limiter surface (green dashed line).

5.1 Review of previous work

In previous work[3] simulations were already performed in order to reproduce the plasma conditions of these shots.

The grid used in the simulation is aligned with the magnetic flux surface until $\rho = 1.11$ and it is built according to the magnetic configuration at 3.334 s and 4.440 s for case A and B respectively. Since the code does not compute impurity

radiation, this is subtracted from the input power. The total input power used in the code is $P_{in} = 500kW$ for both discharges equally distributed between electrons and ions. The perpendicular transport coefficient used in case A increases in the vicinity of the separatrix from 0.1 to $0.9 m^2 s^{-1}$, and then it is constant. In case B, D_{\perp} increases from 0.25 up to $2.5 m^2 s^{-1}$ between $0.999 < \rho < 1.009$, then it decreases again to $0.9 m^2 s^{-1}$ at $\rho = 1.034$. The energy transport coefficients for electron (χ_{\perp}^e) and ion (χ_{\perp}^i) are proportional to the particle transport coefficient ($\chi_{\perp}^e = \chi_{\perp}^i = 7.2 \cdot D_{\perp}$). The density at the separatrix, which is an input parameter in the EMC3 code, is chosen according to the Lithium beam measurement.

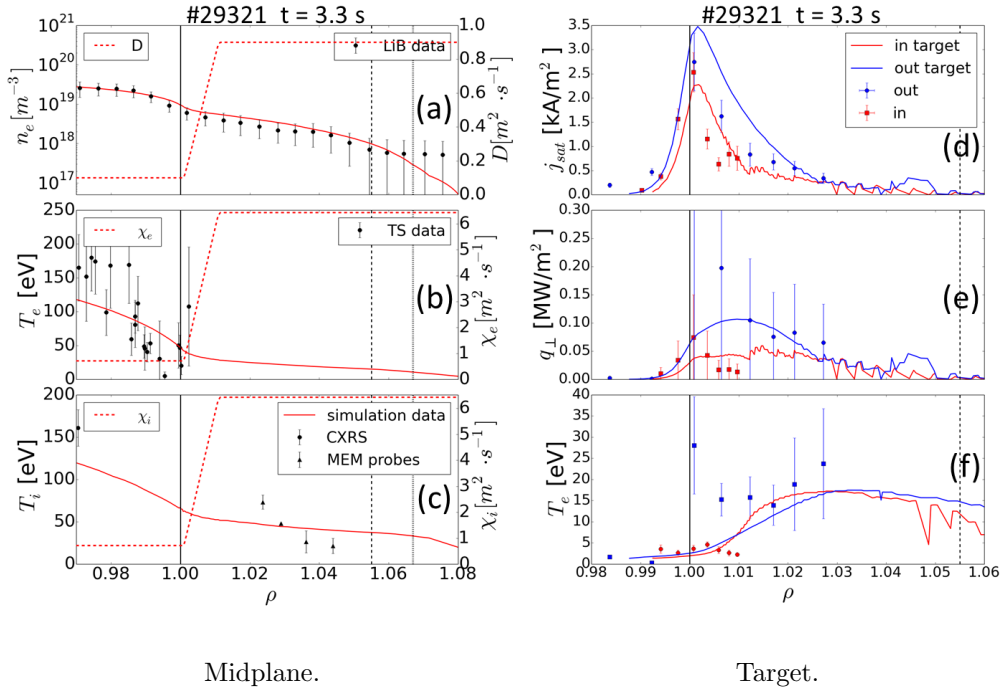


Figure 5.3: EMC3-Eirene simulation of shot 29321 (case A, low density) as in reference [3]. Plots (a), (b) and (c) show the density, the electron temperature and the ion temperature profiles at the midplane. Plots (d), (e) and (f) show the ion saturation current, the heat flux and the electron temperature at the diverter targets. Dots represent the experimental data, while solid curves numerical results. The dashed curves in plot (a) - (c) are the transport coefficients used in the simulations: D_{\perp} , χ_{\perp}^e , χ_{\perp}^i . The solid, dashed and dotted vertical black lines are the separatrix, the heat shield limiter and ICRH limiter surface respectively. All the quantities are plotted against the normalized flux coordinates.

The simulated plasma parameters are compared with density measurements provided by the Lithium beam, electron temperature measured by Thomson scattering and ion temperature measured by charge exchange spectroscopy and midplane probes as well as the Langmuir probe at the targets. Figures 5.3 and 5.4 show the agreement between experimental and numeric results. Plot (a) shows the density profile at the midplane and the experimental points are the lithium

beam measurement, the data are averaged over 100ms around the time of interest ($t = 3.334\text{ms}$ and $t = 4.440\text{ms}$ for case A and B, respectively). Plot (b) shows the simulated electron temperature and the data measured by the Thomson scattering diagnostic, the experimental points shown are measured in the same time window used to average the lithium beam data. (c) shows the ion temperature, the experimental measurement from the CXRS diagnostic and from the midplane manipulator probe.

Plot (d) shows the j_{sat} measured at the divertor targets from the Langmuir probes, the simulated values are calculated using the density and temperature provided by the simulation. Plot (e) shows the perpendicular heat flux over the target plates, it is calculated as:

$$q_{\perp} = j_{sat} * T_e * 8 \quad (5.1)$$

Plot (f) shows the electron temperature at the divertor targets.

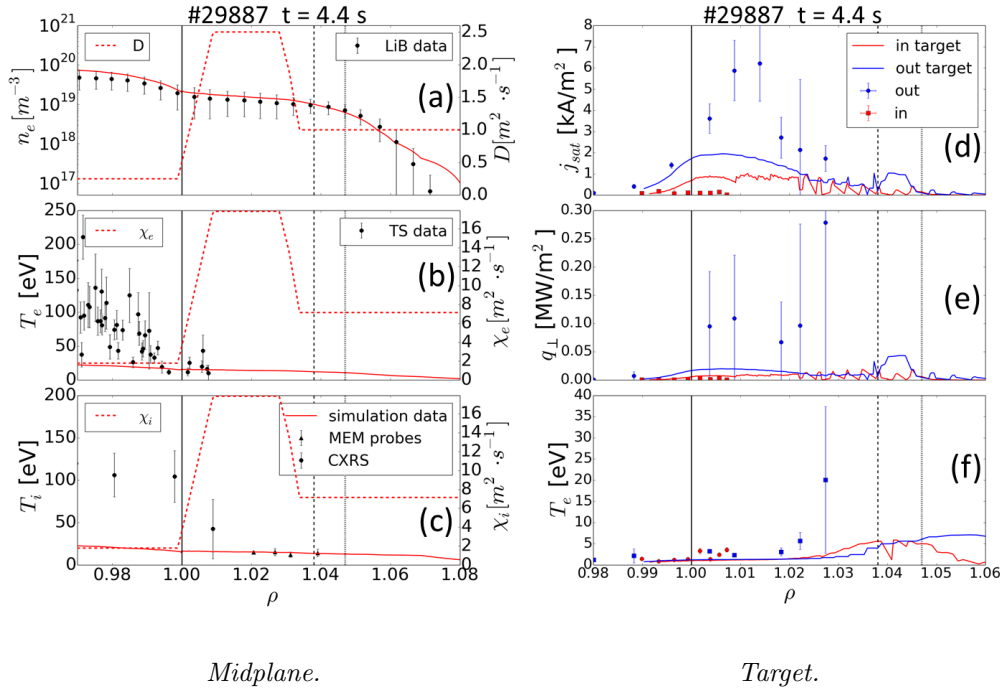


Figure 5.4: High density case. Figure is arranged in the same way as figure 5.3.

The agreement is remarkable in the low density case (before the shoulder formation), while the high density case (after the shoulder formation) the simulation does not match the electron (5.4 (b)) and ion temperature profile (5.4 (c)) at the midplane. Both electron and ion temperature are underestimated even by one order of magnitude. Similarly in case A the simulation matches the experimental measurement at the divertor. On the other hand in case B the simulation does not provide a correct picture of the divertor conditions, in fact figure 5.4 (d) shows that at the outer divertor target the ion saturation current is underestimated of a factor 3, while at the inner divertor target it is overestimated. At the same time

in figure 5.4 (f) can be seen that the electron temperature at the targets is flat and underestimated. However this is a reasonable result considering that in case B the inner divertor is fully detached and the outer divertor is partially detached and EMC3-Eirene does not implement all the physical processes that may play a key role in the detachment.

5.2 Definition of the position of the separatrix

The quantities measured by the diagnostics are plotted against the flux coordinates. This coordinate is calculated using numeric routines, therefore it is approximated. In addition to that the coordinates (R, z) studied by the diagnostics could be affected by a systematic error due to calibration or vibration in the vessel: this adds another uncertainty in the resulting flux coordinates, because the positions are used to calculate the flux coordinates. As a result the profiles measured by different diagnostics and plotted against the magnetic flux coordinates looks shifted one with respect to the others. In other words the the real ρ position studied by the probes is not the one that can be obtained from their R and z position. In the case studied the lithium beam profile and the Thomson scattering profile are displaced one with respect to the other: the shift needed to match the profiles is calculated in order to provide a more precise picture of the two shots analyzed and provide a consistent picture of n_e and T_e at the midplane.

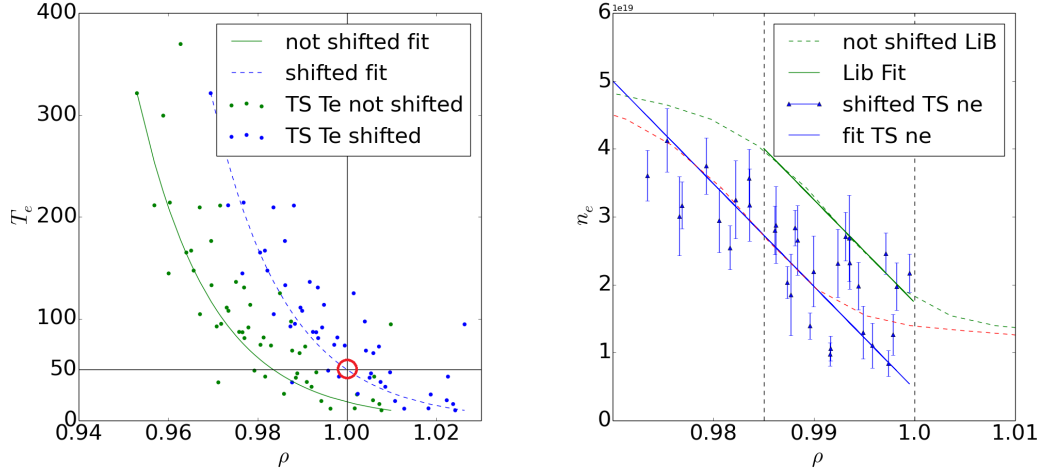
To properly shift the diagnostics a well known plasma parameter that can be set as a reference is necessary. The fact that the temperature at the separatrix is a constant is used to compute the correct shift. In the vicinity of the separatrix the temperature profile displays a e-folding behavior, so the electron temperature measured by Thomson scattering is fitted with an exponential curve:

$$T_e(\rho_{TS}) = A \cdot e^{\frac{\rho_{TS}-c}{b}} \quad (5.2)$$

where ρ_{TS} is the flux coordinate associated with the data measured by the diagnostic, it is different from the real flux coordinates because of the misplacement discussed so far. A , b , c are free parameters of the fit. The fitted function is shifted in order to have the chosen temperature value at the separatrix position. The main point of this shifting procedure is the temperature assumed at the separatrix. The shift can be calculated analytically as:

$$\Delta\rho_{TS} = 1 - c + \ln\left(\frac{T_e^{sep}}{A}\right)^b \quad (5.3)$$

where T_e^{sep} is the supposed temperature at the separatrix position.



The shift of the Thomson scattering.

The shift of the lithium beam function.

Figure 5.5: On the left the Thomson scattering shift process in case B. The green points represent the electron temperature measured by the Thomson scattering, the curves are the fit. In figure is highlighted the temperature supposed at the separatrix: 50 eV. On the right the shift process for the lithium beam. The solid green curve is the fit of lithium beam decay region, the fit region is the one comprised between the two dashed black lines. The red dashed line is the shifted lithium beam profile.

Once that the position of the Thomson scattering is defined, the density profile measured by lithium beam is fitted in the decay region with a linear function.

$$n_e(\rho_{LiB}) = m\rho_{LiB} + q \quad (5.4)$$

where ρ_{LiB} is the same of ρ_{TS} for the lithium beam diagnostic, q and m are the fitting parameters. Finally the density profile measured by the Thomson scattering is fitted using the function:

$$n_e(\rho_{TS} + \Delta\rho_{TS}) = n_e(\rho_{LiB} - \Delta\rho_{LiB}) = m(\rho_{LiB} - \Delta\rho_{LiB}) + q \quad (5.5)$$

where $\Delta\rho_{LiB}$ is the only free parameter and is the shift that is applied to the Lithium beam data. $n_e(\rho_{TS} + \Delta\rho_{TS})$ are the Thomson scattering data shifted. Only the data with $\rho < 1$ are used for the fit because these measurements are less scattered. The shift procedure is shown in figure 5.5. To compute the shift all the quantities are considered respect to the flux coordinate. To prove the validity of the method it is necessary to verify the linearity in the conversion from (R, z) to ρ conversion at least in the region of interest: this means that a $\Delta\rho$ interval correspond to a ΔR for all the regions studied by the diagnostics. This linearity is proved and the corresponding plot is shown in figure 5.6.

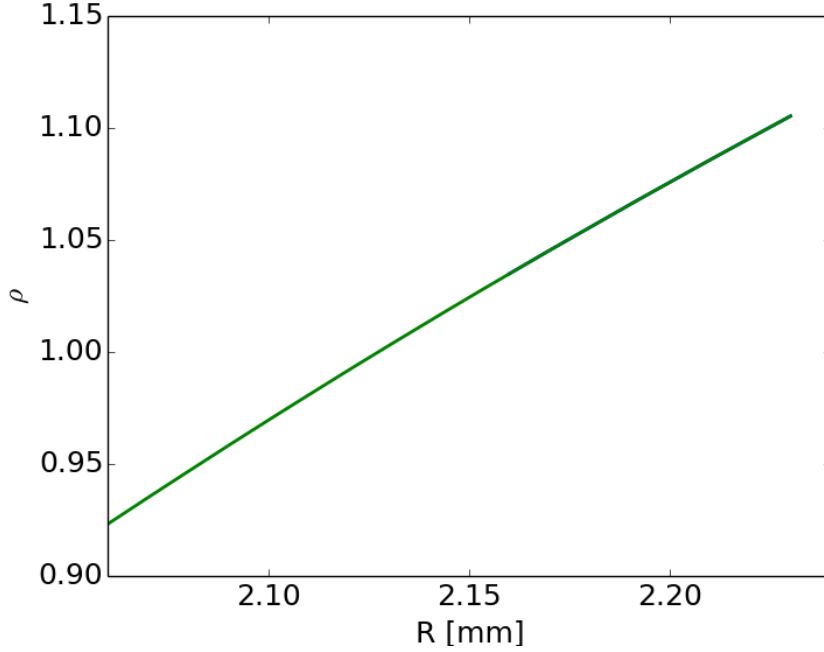


Figure 5.6: The flux coordinates against the radial coordinate in case B. $z = 0.326m$, which corresponds to the Lithium beam height, is used for the conversion.

Conventionally it is supposed $T_e^{sep} = 50 eV$ in L-mode discharge and $T_e^{sep} = 100 eV$ in H-mode discharge. While in the latter case this assumption works quite well, in L-mode the assumption may be false. Different electron temperature are assumed at the separatrix in order to study how the profiles change.

T_e^{sep}	TS shift [ρ]	TS shift [mm]	LiB shift [ρ]	LiB [mm]	$n_e^{sep} \cdot 10^{18} [m^{-3}]$
25 eV	0.0051	3.9	-0.0154	-11.9	12.2
35 eV	0.0106	8.0	-0.0131	-9.9	13.2
50 eV	0.0165	12.8	-0.0084	-6.5	16.0

Table 5.1: The effect of apply different electron temperature at the separatrix position in high density case is seen. In columns the supposed electron temperature at the separatrix, the Thomson scattering shift as $\Delta\rho$, the Thomson scattering shift computed in millimeters, the lithium beam shift as $\Delta\rho$, the lithium beam shift computed in millimeters and the density measured after the shift at the separatrix are reported. Negative value for shift means that the profile is shifted to the left, positive value to the right.

T_e^{sep}	TS shift [ρ]	TS shift [mm]	LiB shift [ρ]	LiB [mm]	$n_e^{sep} \cdot 10^{18} [m^{-3}]$
25 eV	0.0047	3.3	-0.0071	-5.0	4.8
35 eV	0.0085	6.0	-0.0034	-2.4	5.7
50 eV	0.0125	8.9	-0.0002	-0.0	8.3

Table 5.2: The effect of apply different electron temperature conditions in low density case. Columns are arranged as in table 5.1

For each considered temperature considered in table 5.2 and 5.1 a simulation is performed by changing the density at the separatrix used by the code in order to match the lithium beam profiles. The other parameters of the simulation are the same as as reference case. In the low density case (figure 5.7) the 50 eV shift seems to work properly both for T_e and n_e . In this case the simulation fit properly the data points at the separatrix, while in the other simulations the electron temperature is overestimated. For what concerns the electron density the simulation matches better the density profile in the whole SOL and not only at the separatrix. The results of those simulations are shown by figures 5.7 and 5.8.

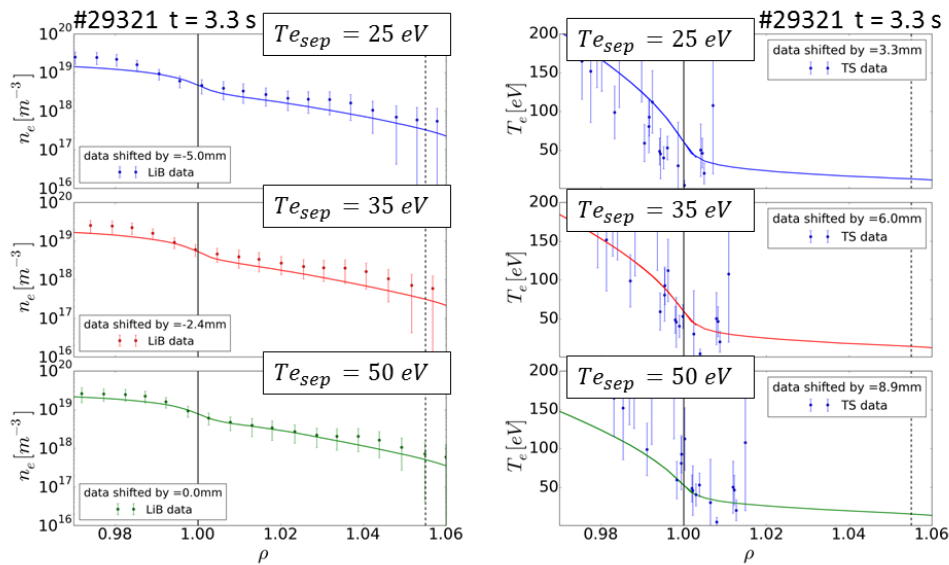


Figure 5.7: Case A. Plots on the left show how the outboard midplane density profile changes with different T_e^{sep} . The ones on the right show how the outboard midplane temperature profile changes.

In the high density case the agreement between experimental data and numeric results is worse if a shift is taken in account. However the shifted profiles at 25 eV

and 35 eV (blue and red curve in figure 5.8 left) are not realistic, the density drops too early, even before the heat shield limiter. The electron temperature profiles do not give any useful information, because the simulations underestimate it (figure 5.8 right) . The conventional electron temperature is the one that works better on both cases, then a $T_e^{se} = 50\text{ eV}$ is used to compute the diagnostic shift.

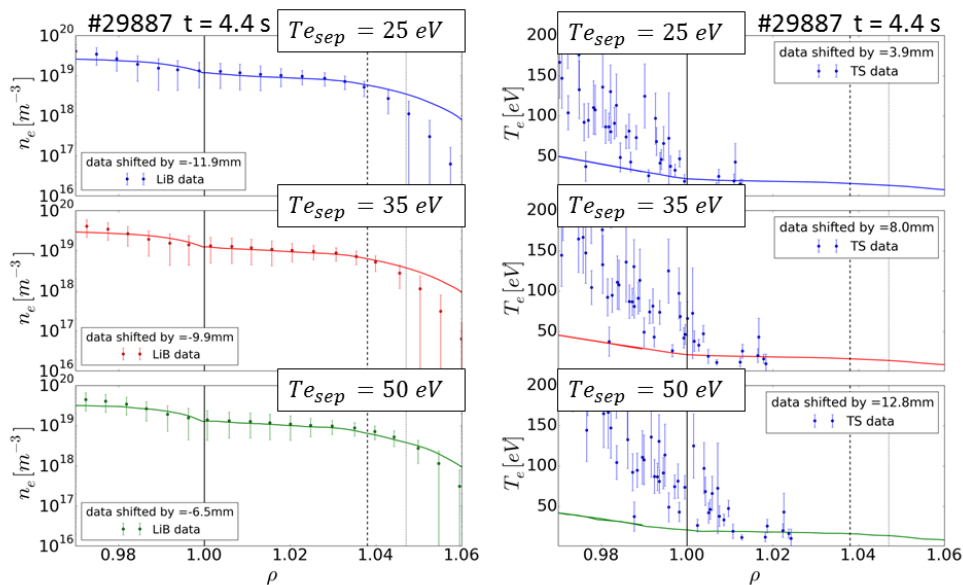


Figure 5.8: Case B. The left column shows how the outboard midplane density profile changes with different T_e^{sep} . The right column shows how the outboard midplane temperature profile changes.

5.3 Enhanced transport at the outboard mid-plane

The case B is characterized by the presence of the density shoulder in the scrape off layer. As explained in section 2.6 filaments undergo a regime transition that enhances the transport at the outer midplane and leads to the density shoulder formation. Since EMC3-EIRENE does not include a model for the filament convective transport, the filament-related transport is approximated as an increase of the perpendicular transport coefficients D_{\perp} , χ_{\perp}^e , χ_{\perp}^i , that determine the cross field transport in the simulations.

In the reference case the transport coefficient in case B is increased up to 2.5 in the region $1.009 < \rho < 1.034$ in the whole Tokamak. In the new simulation performed in this work the transport coefficients are increased in a way that reproduces the filament-related transport (see section 2.5). Therefore the transport coefficients are increased only in the low field side in order to enhance to trans-

port in the same way the filaments do. Since the enhanced transport is present only in the case B, after the shoulder formation, only this case will be studied. The transport coefficients, used in the high density simulation, are modified as:

$$D(\rho, \theta) = D_{\perp}^{homo}(\rho) + f(\rho, \theta) \quad (5.6)$$

where $f(\rho, \theta)$ is chosen as Gaussian-like:

$$f(\rho, \theta) = \frac{A(\rho)}{e^{-\frac{\theta^2}{2\sigma_{\theta}}}} \quad (5.7)$$

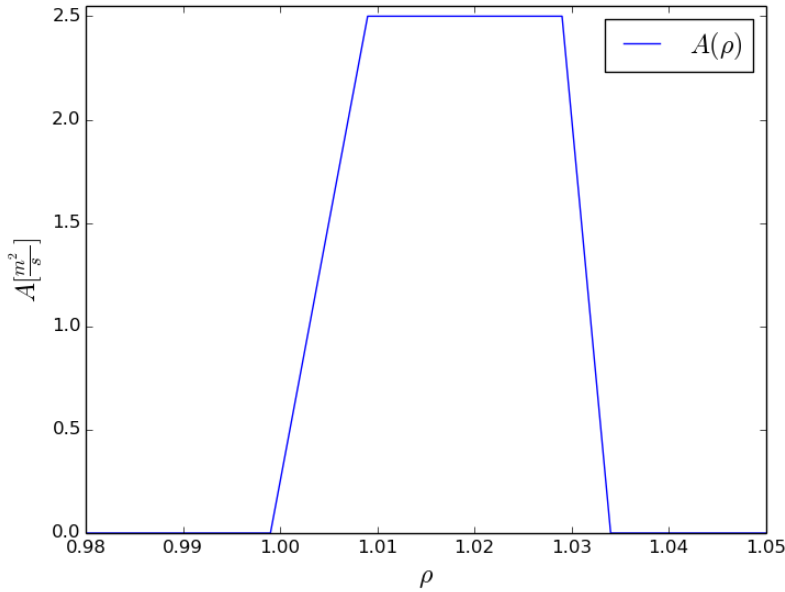


Figure 5.9: The amplitude of the filament-related transport.

The filament related transport is described by $f(\rho, \theta)$. Figure 5.9 shows the shape used for the amplitude $A(\rho)$. The value reached in the flat part of the step is related to the strength of the convective transport related to filaments. The step extension represents the radial region where filaments are present. The FWHM of the Gaussian $\sqrt{2\ln(2)} \sigma_{\theta}$ fixes the poloidal region influence by the filaments related transport, therefore σ_{θ} determines the poloidal width. Finally $D_{\perp}^{homo}(\rho)$ represents the transport unrelated to filaments and is constant in the whole tokamak. The energy transport coefficients have the same shape:

$$\chi(\rho, \theta) = \chi_{\perp}^{homo}(\rho) + g(\rho, \theta) \quad (5.8)$$

where $g(\rho, \theta)$ is chosen Gaussian-like:

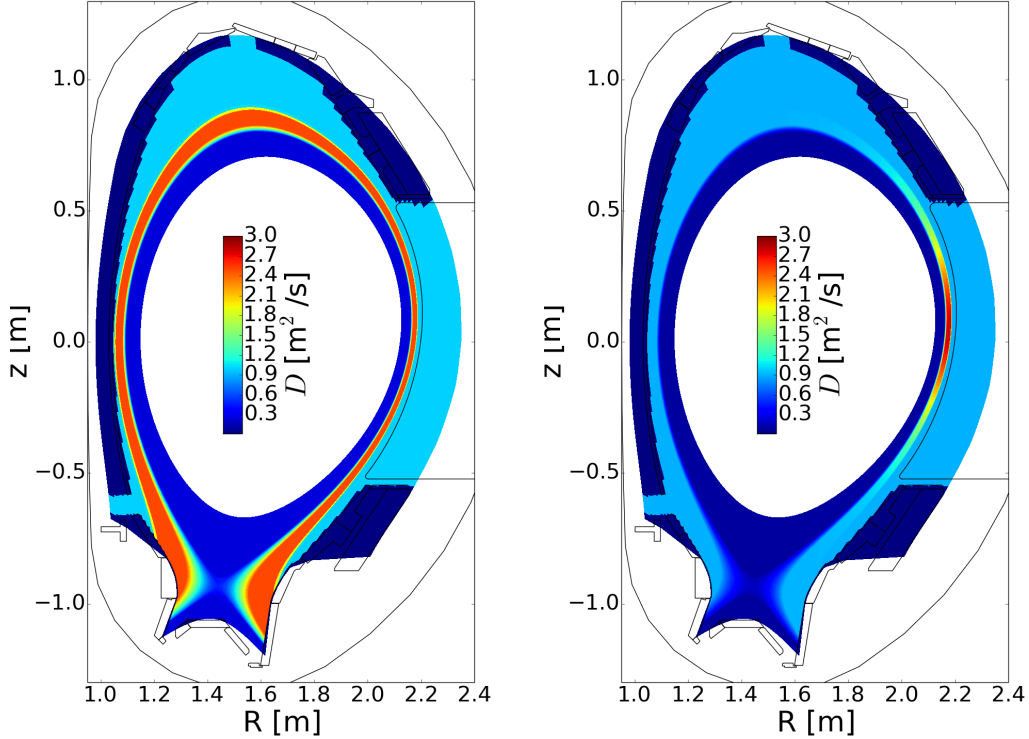
$$g(\rho, \theta) = B(\rho)e^{-\frac{\theta^2}{2\sigma_{\theta}}} \quad (5.9)$$

where χ stands for both χ_{\perp}^e , χ_{\perp}^i and $B(\rho)$ determines the strength of the energy transport related to the filaments. This may be different from $A(\rho)$ and

implies that the filaments transport in different ways energy and particles. The poloidal width σ_θ must be the same of equation 5.7. $\chi_\perp^{homo}(\rho)$ represents the energy transport not related to filaments. The energy transport coefficients could be different $\chi_\perp^e \neq \chi_\perp^i$, meaning that the cross field transport works differently for ions and electrons. However this case is not considered in this work.

A simulation is performed with this new set of parameters: $\sigma_\theta = \frac{\pi}{6}$. The $A(\rho)$ used is shown in figure 5.9. Since the only difference between case A and B is the expected filament-related transport, the homogeneous part of the transport coefficient is considered equal to the low density case $D_\perp^{homo} = D_\perp^{caseA}$. Figure 5.3 show the transport coefficient used in the reference case (left) and the localized one used for the new simulation (right). As in the reference simulation is used:

$$\chi_\perp^e = \chi_\perp^i = 7.2 \cdot D_\perp \quad (5.10)$$



D_\perp homogeneous in the whole Tokamak . D_\perp increased only in the outer midplane.

Figure 5.10: Comparison between the transport coefficient that is homogeneous in the whole Tokamak and the transport coefficient enhance with the stepwise function at the outer midplane.

The agreement between experimental and numeric results is slightly improved, the results are shown in figure 5.11. The electron and ion temperatures increase inside the separatrix and even if the simulated profiles do not match the experimental data the agreement is improved. Also the j_{sat} provided by the simulation at the outer target improves. The results provided by this simulation indicate

that an enhanced transport in the outer midplane is enough to create the shoulder. Moreover the filament-related transport can be properly simulated using the perpendicular transport coefficients. Finally it also gives a picture of the transport coefficient in the SOL region, that is normally assumed to be $\simeq 1$.

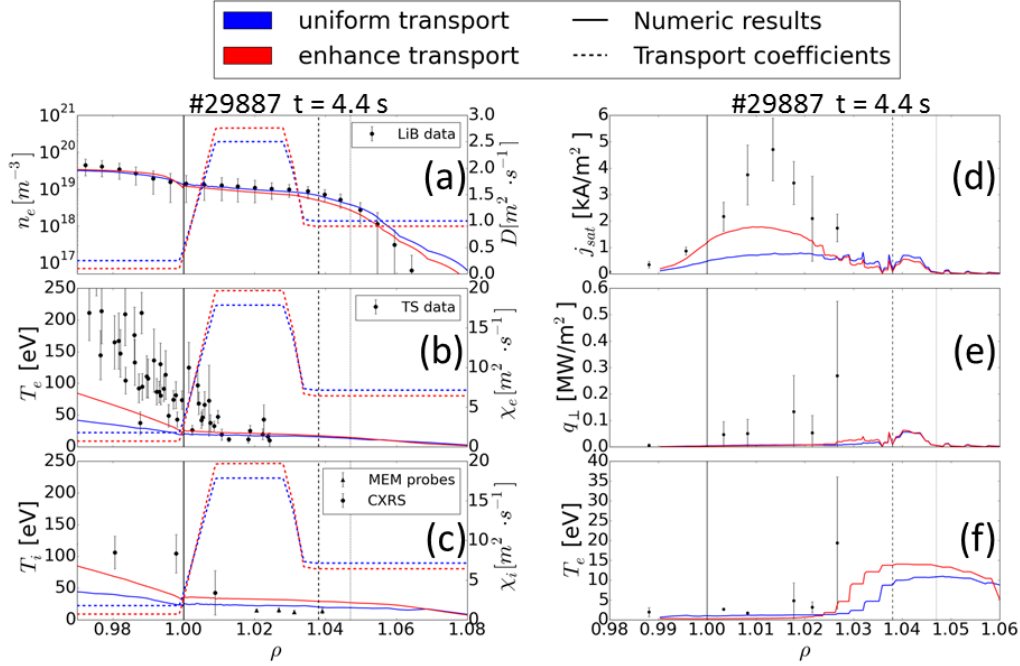


Figure 5.11: Comparison between the simulation is carried out using D_{\perp} equal in the whole Tokamak [3] shown in blue and using the modelled enhancement of transport in the outer midplane shown in red. Lines and plots are arranged as in figure 5.3.

5.4 Parameter optimization

The perpendicular transport definition used so far defined in equation 5.6 and 5.8 has an high number of degrees of freedom. A study on which are the parameters that influence the most the perpendicular transport is carried out in order to improve the agreement between the numerical results and the experimental measurements. Among all the parameters studied, here only the most interesting results will be reported: the energy transport coefficients ($\chi_{\perp}^{e,i}$), the amplitude ($A(\rho)$) and the width (σ_{θ}) influenced by filaments related transport.

5.4.1 Energy transport coefficient

In the simulation discussed in section 5.3 is used:

$$\chi_{\perp}^e = \chi_{\perp}^i = 7.2D \quad (5.11)$$

The energy transport coefficients used in that simulation are too high and lead to electron and ion temperature profiles lower than the ones measured by the diagnostics (figure 5.11). A new simulation is carried out using:

$$\chi_{\perp}^e = \chi_{\perp}^i = 3D \quad (5.12)$$

The results are shown in figure 5.12. The energy transport is strongly reduced inside the separatrix and the resulting electron temperature matches better the measurements both in the midplane and in the divertor targets (figure 5.12). At the same time the ion temperature is overestimated. Almost no difference is observed in the density profiles.

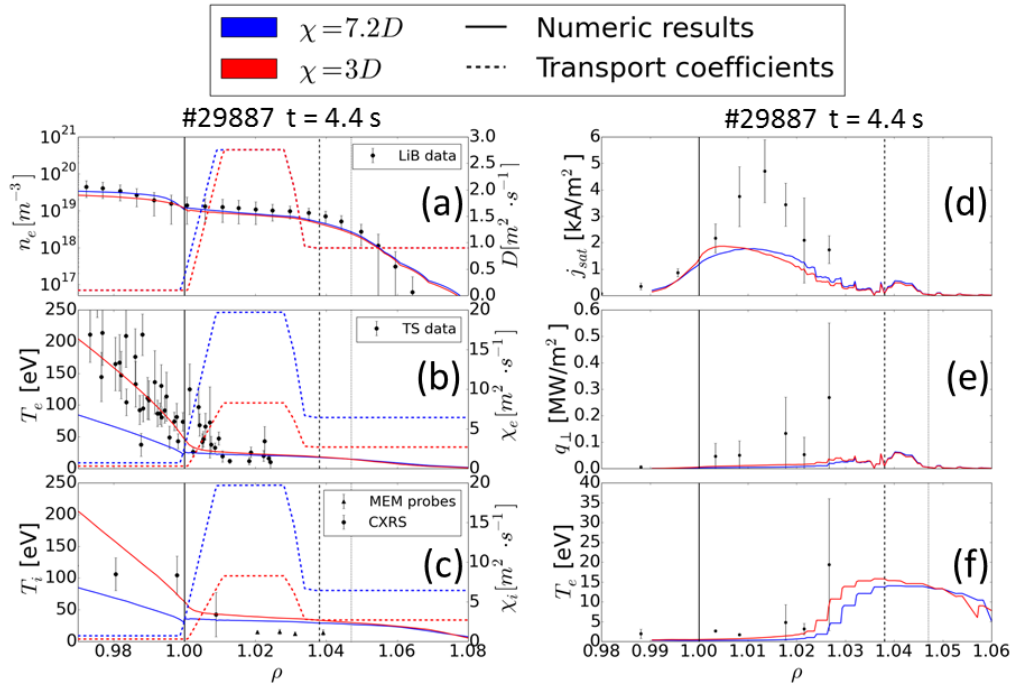


Figure 5.12: Comparison between the simulation carried out with using $\chi_{\perp}^{e,i} = 7.2D_{\perp}$ shown in blue and $\chi_{\perp}^{e,i} = 3D_{\perp}$ shown in red. The lines and plots are arranged as in figure 5.3.

5.4.2 Amplitude of the filament-related transport

A group of simulations is carried out using different maximum values for $A(\rho)$ the results are shown in figure 5.13: The $A(\rho)$ used in the simulation have a maximum value of 1.5, 2.5, 4.5. This change does not have a strong effect and only a weak dependence in the density is observed at the midplane. A decrease

of the filament-related transport leads to a lower density in the scrape of layer. On the other hand the j_{sat} increases in the divertor.

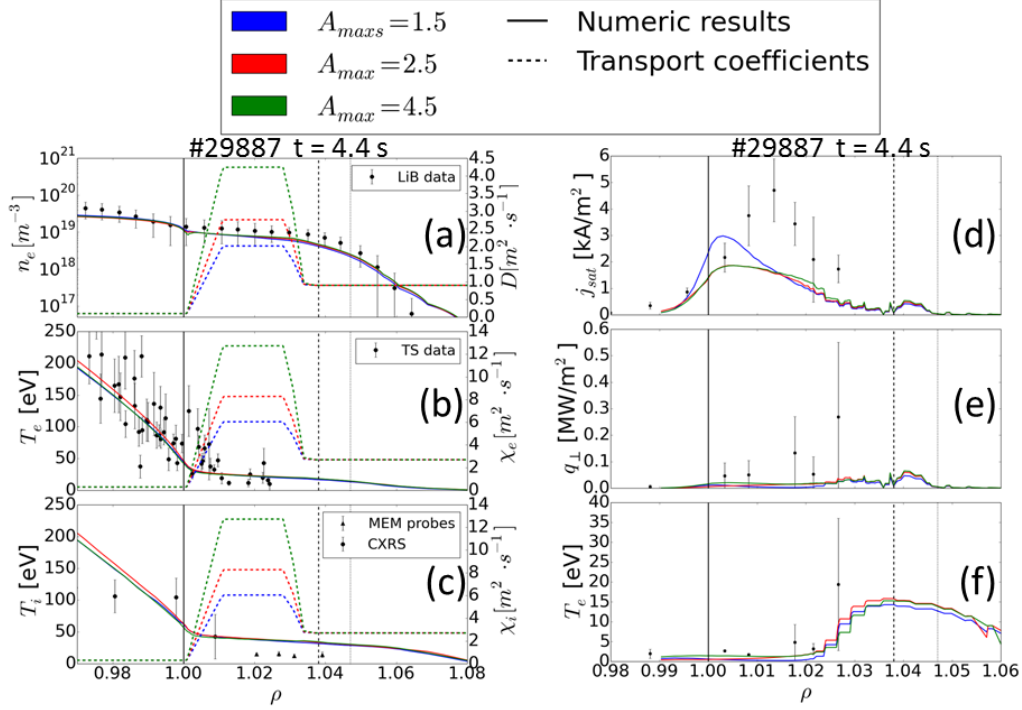


Figure 5.13: Comparison between the simulation carried out with different filament related transport strength. Blue, red and green represent $A_{max} = 1.5$, 2.5 and 4.5 respectively. The lines and plots are arranged as in figure 5.3.

5.4.3 Poloidal width of the filament-related transport

In order to understand which area of AUG is influenced by the increase of the convective transport a set of simulations is studied, is performed by varying the value of σ_θ . No significant differences are observed in the results provided by several simulations displayed in figure 5.14.

The results provided by simulation in sections 5.4.2 and 5.4.3 may bring into crisis the transport coefficients model used. In fact if the amplitude and the poloidal width which describe the filament related transport change significantly the results do not change substantially. This can be explained considering that the main affect of localize the transport in the outer midplane is to reduce the transport in other regions: since the transport in these regions is kept low then no significant variations are expected.

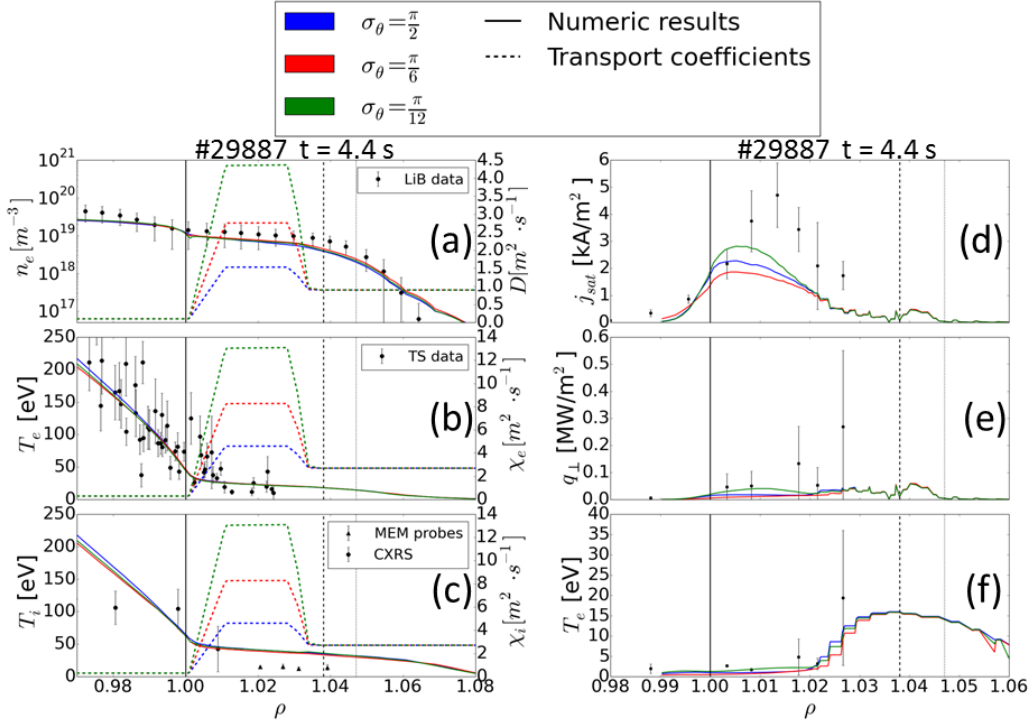


Figure 5.14: Comparison between the simulation carried out with different filament related transport width. Blue, red and green represent $\sigma_\theta = \frac{\pi}{2}$, $\frac{\pi}{6}$ and $\frac{\pi}{12}$ respectively. The lines and plots are arranged as in figure 5.3.

This is consistent with the observations. If $A(\rho)$ increases and $\sigma_\theta = \frac{\pi}{6}$ is kept constant, then this affects only the region around the midplane. Anyway if $A(\rho) = 0$ the numerical results would not match the measurements, in particular the simulated density profile has the same shape of the case A. This indicates that a poloidal dependence on the transport coefficients is needed. Similarly when σ_θ varies and $A(\rho) = 2.5$ is kept constant, the contributions at the edges will be negligible, meanwhile the transport coefficients values at the midplane ($\theta = 0$) will be the same and no differences are observed. If both σ_θ and $A(\rho)$ increase the simulation moves back to the reference case, where the transport coefficients are poloidally homogeneous coherently with this explanation. On the other hand, reducing the poloidal width affects the simulation convergence. It is observed that for the minimum poloidal width used the simulation is not properly converged because of the sharp variations in the transport coefficients.

5.4.4 Reduction of the transport after the limiter

In the simulations carried out up to now the density is overestimated at $\rho > 1.05$. This region is described by D_\perp^{homo} . The experimental density profile drops because of the interaction with the limiter. The simulation density profile overestimates the density in the limiter shadow because of a too high transport after the interaction with the limiter. In this region $f(\rho, \theta) = 0$ therefore D_\perp^{homo} is responsible

for the overestimated transport. A reduction in the transport is considered in order to properly simulate the effect of the limiter shadow. Up to now the D_{\perp}^{homo} is equal to the transport coefficient used in the case A, then $D = 0.9 \text{ m}^2 \text{ s}^{-1}$ after the limiter. In the following simulations a D_{\perp}^{homo} that decreases at $\rho = 1.37$ to different values, lower than $0.9 \text{ m}^2 \text{ s}^{-1}$, is used. $f(\rho, \theta) = 0$ at the same position where D_{\perp}^{homo} drops. The energy transport coefficient used in the simulation are proportional to the particle transport coefficient $\chi_{\perp}^{e,i} = 3D_{\perp}$.

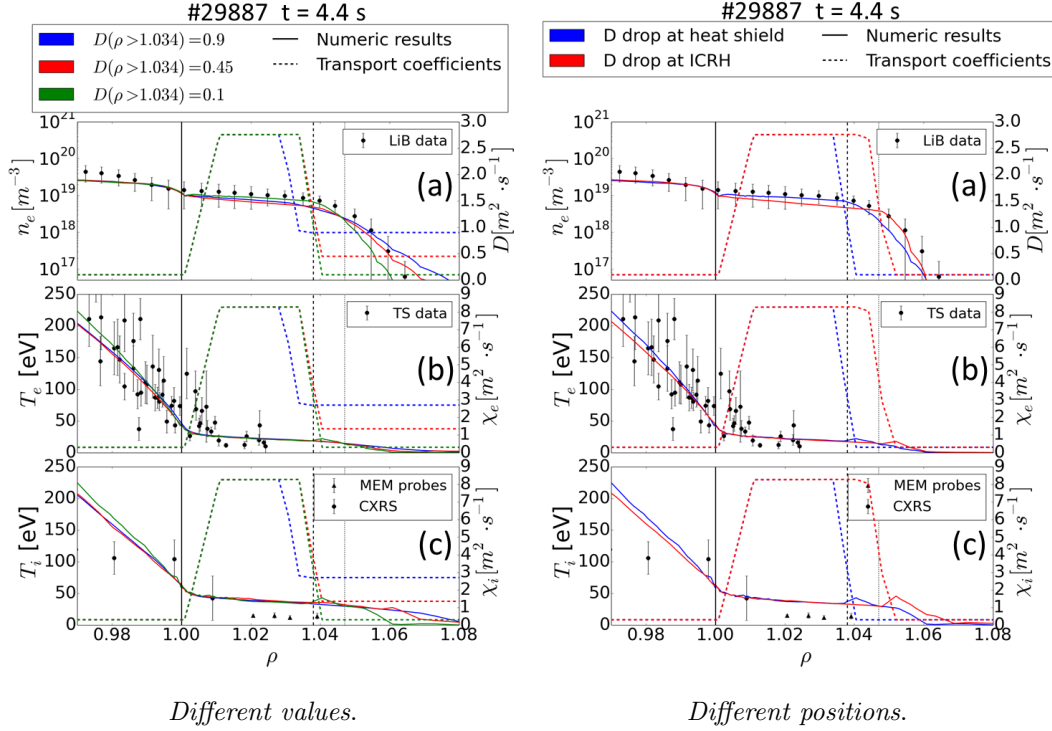


Figure 5.15: Plots on the left show the changes in the density, electron and ion temperature profiles considering different reductions of the transport coefficients. Plots on the right show the changes in the density, electron and ion temperature profiles considering different reduction positions. The lines and plots are arranged as in figure 5.3.

The simulated profiles shown in blue in figure 5.15 on the left are the one discussed in section 5.3 and are used as comparison. In simulations with $D_{\perp}^{homo}(\rho > 1.04) = 0.9 \text{ m}^2 \text{ s}^{-1}$ and $D_{\perp}^{homo}(\rho > 1.04) = 0.45 \text{ m}^2 \text{ s}^{-1}$ which are plotted in blue and red respectively in figure 5.15 the density is overestimated. On the other hand simulation with $D_{\perp}^{homo}(\rho > 1.04) = 0.1 \text{ m}^2 \text{ s}^{-1}$ underestimates the density. Anyway in this latter case the density profile shows the same trend of the experimental profiles, but the simulated density profile decays too early. The value of the particle transport coefficient in the limiter shadow controls the decay in the density, moreover it affects also the density before the limiter. In fact when the D_{\perp} drops to a value of $0.1 \text{ m}^2 \text{ s}^{-1}$ the density before the limiter increases. Other simulations, in which a displacement of the transport coefficient decay position is tried, shows that the density profile decays in different positions (figure 5.15 left).

The density decay starts at the midpoint of the particle transport decay. The electron and ion temperature profiles show a decay when the density becomes lower than $10^{17} m^{-3}$. Moreover all the simulations discussed so far have the same problem: the computational time needed to solve the energy equation is too long. It results in simulations that are not completely converged and the results in the divertor (where most of the fluctuation are localized) are not reliable, for this reason the divertor condition are not plotted. However it is proved that this problem can be overtaken considering the decrease of the transport only in D_{\perp} and not in $\chi_{\perp}^{e,i}$.

5.5 Final Simulations

The analysis carried out in this chapter are used to determine the best set of coefficients to simulate both discharges. In case A the separatrix density is $n_e^{sep} = 0.83 \cdot 10^{19} m^{-3}$. The particle and energy transport coefficients used are shown in figure 5.16. D_{\perp} is poloidally symmetric: it increases at $\rho = 1.001$ from $0.1 m^2 s^{-1}$ to $0.9 m^2 s^{-1}$. The results provided by simulations explained in section 5.4.4 show that a drop in the homogeneous part is needed to simulate the plasma conditions in the limiter shadow. Consistently with those result the particle transport coefficient used drops at the limiter to a value of $0.1 m^2 s^{-1}$. Differently the energy transport coefficients are the same used in the reference case, because of the same problem shown in section 5.4.4.

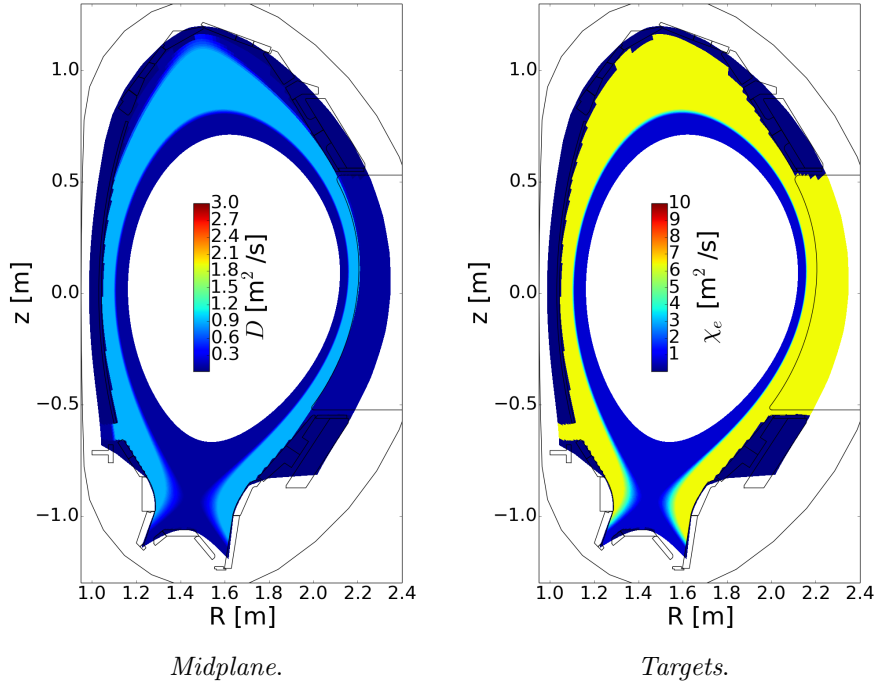


Figure 5.16: D_{\perp} and $\chi_{\perp}^e/\chi_{\perp}^i$ used in the low density simulation.

The results are shown in figure 5.17. The simulated density and electron temperature profiles at the midplane show a reasonable good agreement with

the experimental data. The ion temperature profile does not match perfectly the experimental measurement but it has a realistic shape. At the divertor the simulated j_{sat} matches the experimental data almost perfectly for the inner divertor and it is slightly overestimated at the separatrix in the outer target. The electron temperature, on the contrary, is well simulated in the outer target and overestimated in the inner target. Considering that the inner divertor is partially detached this overestimation of T_e is not surprising. Anyway in general the numeric results match properly the experimental measurements.

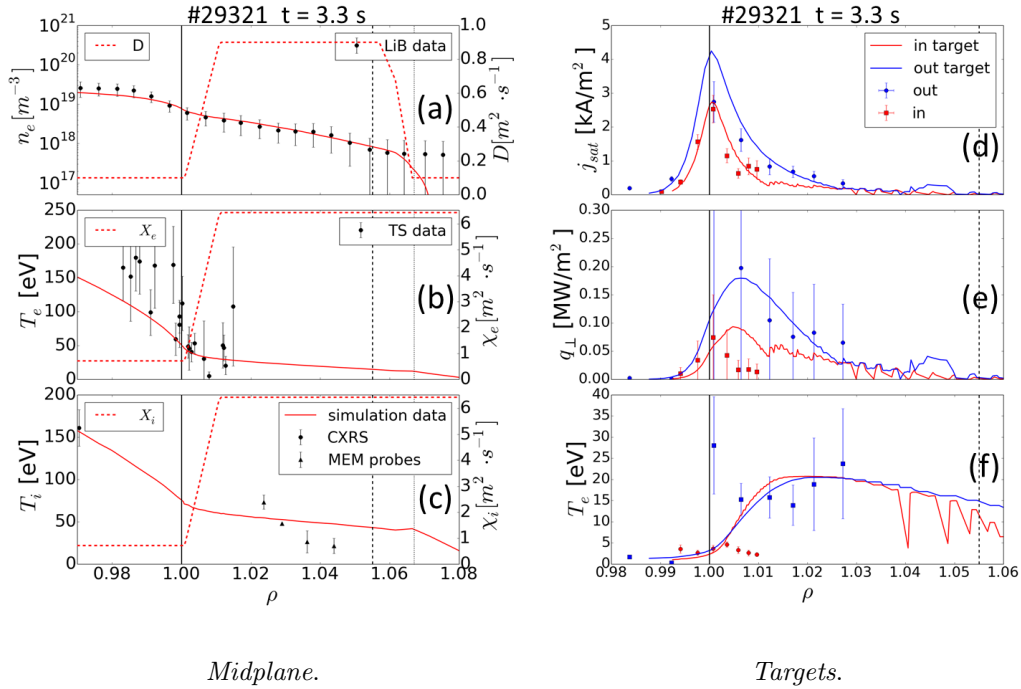


Figure 5.17: Agreement between experimental and numerical results in the best simulation for the low density case. The lines and plots are arranged as in figure 5.3.

Case B is the more problematic to simulate than case A because of the divertor targets conditions (detached and partially detached) and the high localized transport in the SOL. As learned from section 5.2 the density in the separatrix is set in the simulation to a value of $n_e^{sep} = 1.60 \cdot 10^{19} m^{-3}$. The particle and energy transport coefficient used are shown in figure 5.18. D_{\perp} is defined according to the equation 5.6, D_{\perp}^{homo} has the same shape of $D_{\perp}^{case A}$, where the decay position is moved accordingly to the limiter position in case B. $f(\rho, \theta)$ has the shape discussed in section 5.3. Both the components of the energy transport coefficients increase at $\rho = 1.011$ (instead of $\rho = 1.001$). The results of this simulation are shown in figure 5.19.

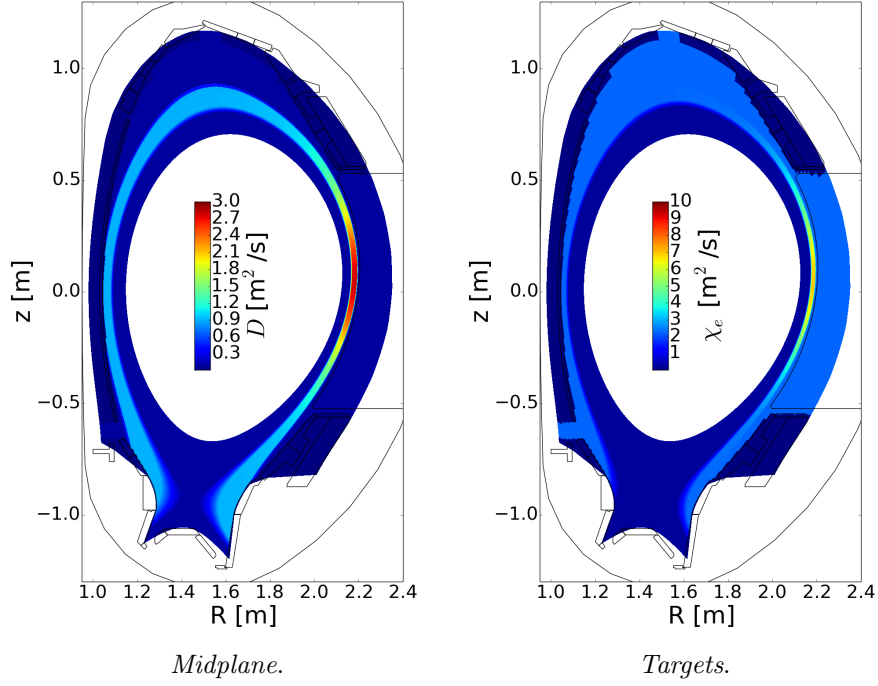


Figure 5.18: D_{\perp} and $\chi_{\perp}^e/\chi_{\perp}^i$ used in the high density simulation.

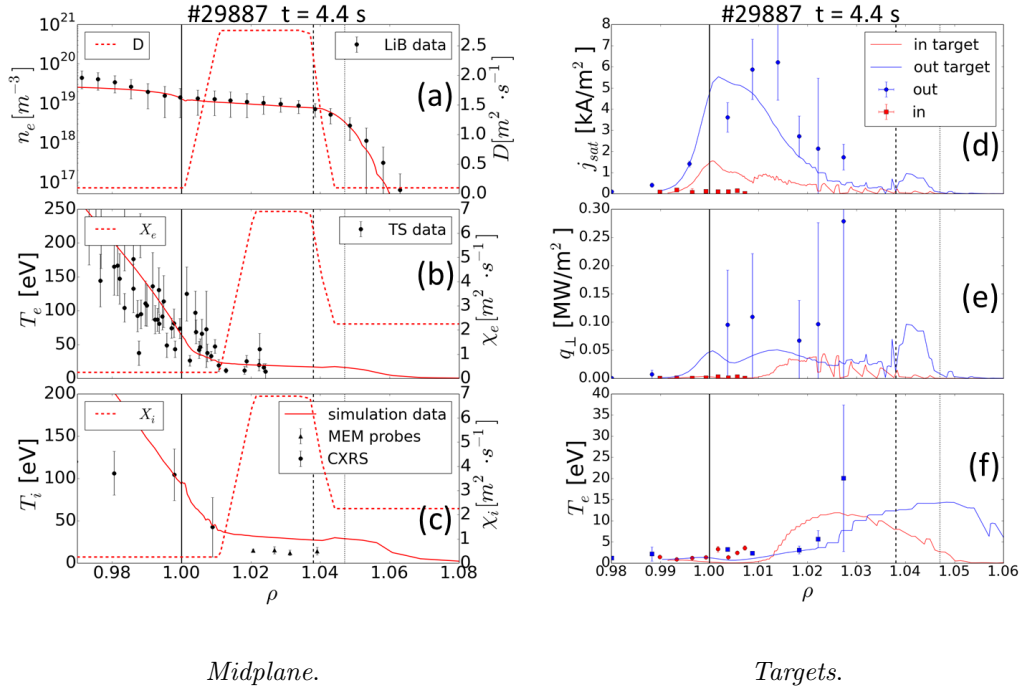


Figure 5.19: Agreement between experimental and numeric results in the best simulation for the high density case. The lines and plots are arranged as in figure 5.3..

Similarly to the case A the simulated density and electron temperature profiles match properly the experimental ones. On the other hand the ion temperature is overestimated. j_{sat} provided by the simulation has the same shape of the experimental one: a strong asymmetry between inner and outer target is observed. At the same time the simulation strongly underestimates the temperature in the inner targets, this explains the asymmetry in the j_{sat} . It is important to highlight that the power flux over the target is corrects.

Both cases show a realistic agreement between numeric results and experimental measurements both in the divertor and in the midplane. In both cases the worst fit is the ion temperature however the trend is correct in both cases and even if the simulations do not match exactly the results they are acceptable. The other problematic region is the divertor: in case B the density profile at the inner divertor while in case A the electron temperature differs significantly from the measurements. In this chapter the two discharges at different degrees of shoulder formation are properly simulated. In particular the shoulder formation is simulated enhancing the transport in the outer midplane region by a factor 3 in good agreement with the experimental observation [15]. The energy transport coefficients are decoupled from the particle transport coefficient. Moreover it is observed a strong reduction in the transport in the limiter shadow, this is also suggested by some recent observation [32]. Finally an accurate study of the simulation results is carried out, comparing the simulated profiles with the experimental measurement which were not considered in the previous work and the simulation are significantly improved with respect to the preliminary simulations [3].

Chapter 6

Background plasma analysis

6.1 X-point analysis

For what concerns the simulation in the X point, both volumetric recombination and impurity radiation may become important at low temperature, these processes are not considered in the EMC3-EIRENE simulation performed. In addition to that, at the X-point a probe measurement may (significantly) perturb the plasma conditions. For these reasons is challenging simulate the plasma at the X-point.

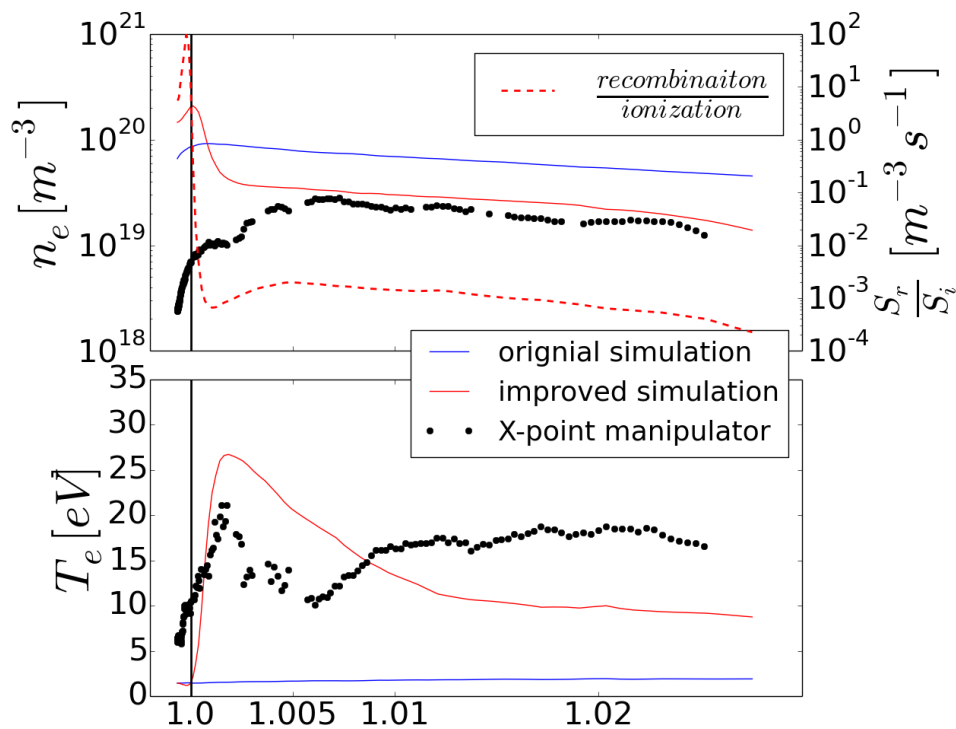


Figure 6.1: Simulated and experimental results at the X-point. Black dots represent the experimental measurement from X-point manipulator and solid curves the prediction from EMC3-EIRENE code. The dashed curve shows the ratio between the ionization and recombination rates.

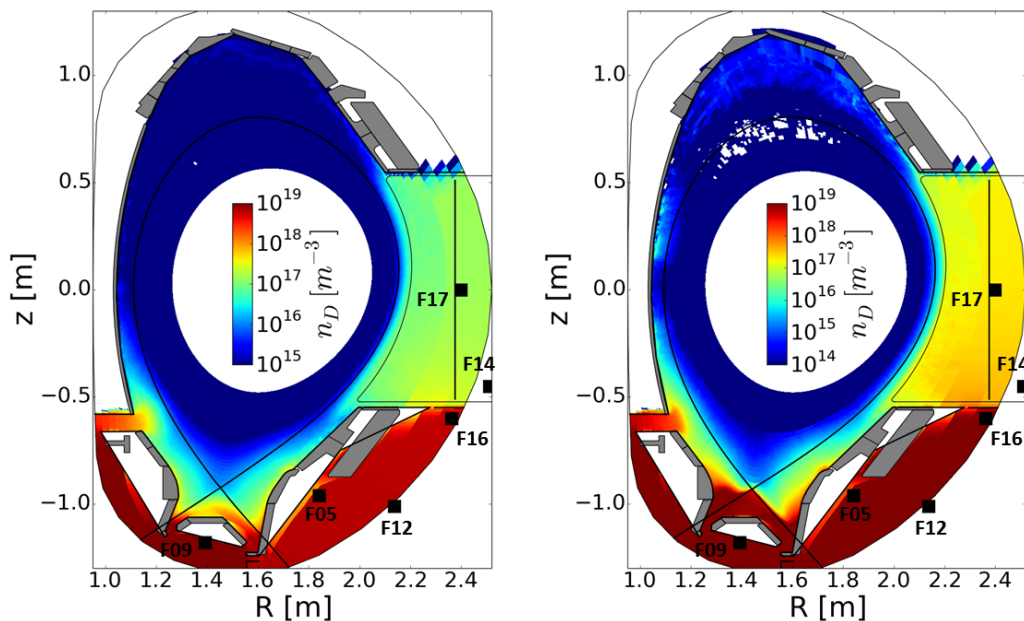
Figure 6.1 shows the comparison between the experimental data and the numerical results at the X-point for the reference case (uniform transport coefficients) and for the improved simulation (localized transport coefficients). The largest differences between simulations and experimental points are found close to the X-point. The high density and low temperature in the vicinity of the separatrix enhance the recombination processes that in this region may be important. The ration between recombination and ionization is shown in figure 6.1 (red dashed lines). It is not clear weather the inclusion of recombination is enough to improve the simulations, but it is likely that the recombination term cannot be neglected in this particular case. Anyway the simulation profiles in the vicinity of the X-point are strongly improved enhancing the transport at the outboard midplane. This represents a clear improvement with respect to the previous work, and is a further indication that the shape of transport coefficients is well chosen. The good agreement reached increases the reliability of the simulations by proving that the results are credible not only at the targets and outer midplane, but also at the X- point.

6.2 Neutral particle density

The EMC3-EIRENE code provides the deuterium molecule and atom density. In ASDEX Upgrade, the only neutral pressure measurements available are performed by the manometers (described in section 3.2.4) located behind the PFCs. The simulation results can give a picture of the neutral density where no measurements are available. The diagnostics measure ion current generated from the neutral particles that are ionized in the manometers. The measured flux is scaled in order to have an atom flux, consequently a single molecule is seen as two atoms by the manometers. For this reason the neutral density used to perform the comparison is $n_n = n_{atoms} + 2n_{molecules}$, where n_{atoms} is the neutral atom density and $n_{molecules}$ is the neutral molecule density.

Manometer	$\frac{n_{nprobe}}{n_{nsim}}$ case A	$\frac{n_{dprobe}}{n_{dsim}}$ case B
F05	$\frac{1.1 \cdot 10^{19}}{9.4 \cdot 10^{18}} = 1.2$	$\frac{2.8 \cdot 10^{20}}{1.5 \cdot 10^{19}} = 17.8$
F09	$\frac{4.2 \cdot 10^{19}}{2.2 \cdot 10^{19}} = 1.9$	$\frac{7.2 \cdot 10^{20}}{4.2 \cdot 10^{19}} = 16.9$
F12	$\frac{6.5 \cdot 10^{18}}{1.2 \cdot 10^{19}} = 0.5$	$\frac{1.3 \cdot 10^{20}}{2.1 \cdot 10^{19}} = 6.3$
F14	$\frac{1.3 \cdot 10^{17}}{4.0 \cdot 10^{17}} = 0.3$	$\frac{1.9 \cdot 10^{18}}{6.9 \cdot 10^{17}} = 2.7$
F16	$\frac{6.7 \cdot 10^{18}}{1.2 \cdot 10^{19}} = 0.6$	$\frac{1.2 \cdot 10^{20}}{2.0 \cdot 10^{19}} = 6.4$
F17	$\frac{3.4 \cdot 10^{17}}{2.3 \cdot 10^{17}} = 1.2$	$\frac{1.6 \cdot 10^{18}}{4.0 \cdot 10^{17}} = 3.9$

Table 6.1: The comparison between experimental measurements and numeric results. Columns are from left to right: the probe names, the ratio between probe data and simulation data in case A, the same ratio in case B.



Neutral particle density in case A.

Neutral particle density in case B.

Figure 6.2: The neutral particles density in a poloidal cross section of AUG. The squares indicate the position of the manometers. The white areas are regions where no simulation data are available.

The manometers F12, F14, F16 measure the neutral density outside of the computational domain of the simulations. In these cases, data is then compared with the nearest defined grid cell.

In case A the simulation results match pretty well the experimental data. The diagnostics (F05, F09, F17) placed in a region where simulation data are available show a good agreement with the simulation results. Only F09 shows a deviation, this could be related to its position or to the fact that the code does not take in account volumetric recombination and this can play an important role in the divertor regions. The three manometers (F12, F14, F16) out of the simulated area measure higher densities than the one provided by the simulation. However considering that the probes are placed in a region where the neutral density is expected to be lower, it can be inferred that the simulation results are correct.

In case B the simulation underestimates the neutral particles density. A trend can be recognized, namely that the agreement improves moving from the divertor targets to the midplane. This can be explained considering the divertor target conditions in that shot (inner and outer target are fully detached and partially detached respectively). The detachment of the plasma from the targets likely occurs when the plasma cools down at the divertor targets. As a result the recombination rate increases and the plasma that flows onto the targets is reduced. In the low density case, where the plasma is not detached from the targets, the neutrals are properly simulated without considering volumetric recombinations. On the other hand in the high density case the physics processes considered in

the code are not enough to provide a quantitative description of the neutral distribution at the targets. The recombination and ionization rate are calculated as:

$$S_i = n_n * n_e * C_i(T_e, n_e) \quad (6.1)$$

$$S_r = n_e * n_e * C_r(T_e, n_e) \quad (6.2)$$

where C_i and C_r are the ionization and recombination coefficient respectively, these coefficients depend on the plasma density and temperature. The recombination rate becomes higher than the ionization rate at the divertor (figure 6.3 and 6.4 right) in case B: the ionization rate drops in front of the inner divertor, and, at the same position, the recombination rate has a sharp increase to a point at which it is larger than the ionization rate. On the other hand this is not true in case A when the ionization rate decreases in front of the divertor, but never becomes lower than the recombination rate, which justifies the negligence of the recombination in equation 4.1.

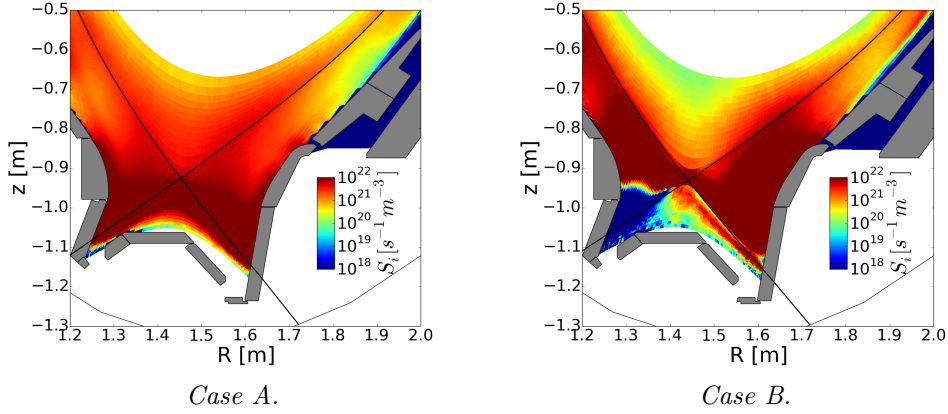


Figure 6.3: The ionization rate for both low (left) and high (right) density. The color code is shown in the figures.

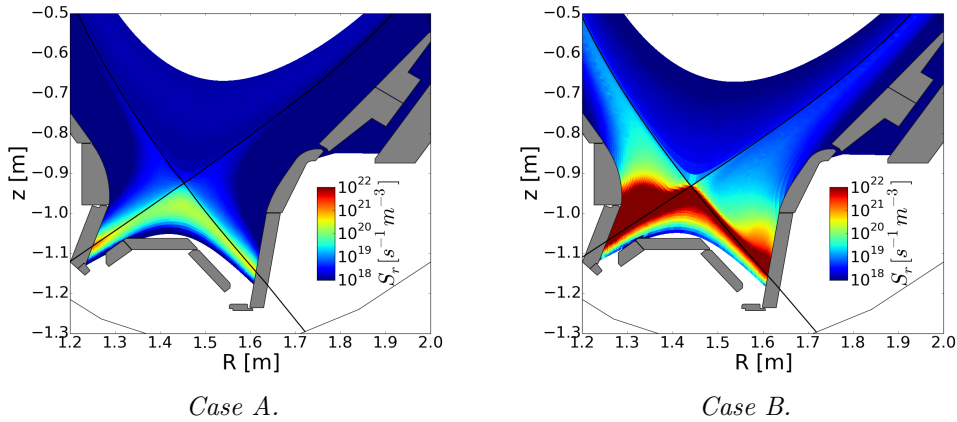


Figure 6.4: The recombination rate for both low (left) and high (right) density. The color code is shown in the figures.

In any case, this cannot explain the discrepancy at the midplane where recombination should be negligible. The experimental neutral density is inferred from a measured flux supposing the neutral particle temperature to be 300 K , but it may be higher for some plasma conditions leading to an overestimated neutral density. It can be concluded that the misplacement between measured and simulated neutral particles density in the high density case is likely related to the convolution of those two effects that leads to an underestimated simulated n_n and to an overestimated measured n_n .

Given what has been said so far, the results provided by the code are good enough to study the interaction between the neutral particles and the plasma, as well as the differences between the two cases. In case A the plasma is partially detached from the inner divertor target, while in case B it is fully detached. Figure 6.5 shows the target conditions for case A and B. Considering that the simulation underestimates the neutral density in case B, the distribution shown in figure 6.5 can be considered as a lower limit for the neutral density. In general in the high density case the neutral density at the divertor region is significantly higher than in the low density case. In case A where the outer target is fully attached the neutral density in front of the target is lower than 10^{18} m^{-3} and they are confined in the private flux region (see figure 6.5 on the left). When the plasma starts to detach from the targets (case B, figure 6.5 on the right) the neutrals cross the separatrix and starts to influence the plasma in the SOL.

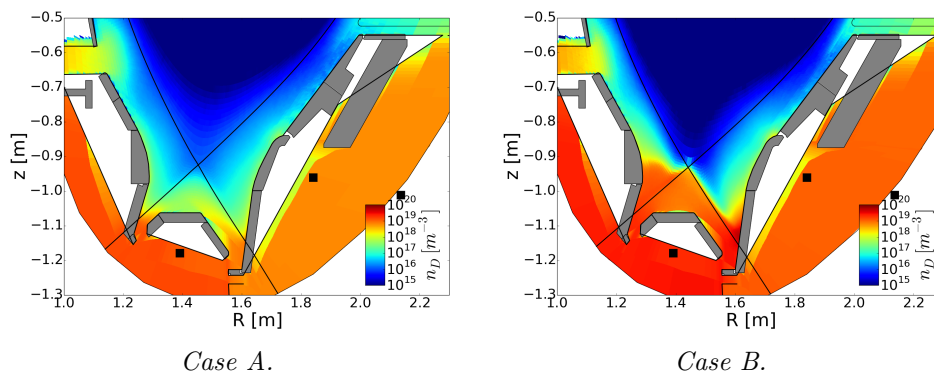


Figure 6.5: An enlargement of the divertor targets for both low (left) and high (right) density. The color code is shown in the figures.

At the midplane the neutral density is higher in the high density case than in the low density case. The high density case is characterized by a neutral density higher than 10^{17} m^{-3} in the far SOL that decreases near the separatrix (figure 6.6 right). Differently in the low density case the neutral density is lower in the far SOL but higher near the separatrix (figure 6.6 left). At the midplane a stronger gradient exists in the high density case, in which neutral density is higher near the wall, but a strong ionization peak appears in front of the limiter ($\rho \simeq 1.08$), and reduces the neutral density in the near SOL under the low density case level. Anyway the simulation underestimates the neutral density in the high density case also at the midplane, therefore the quantitative results must be handled with care.

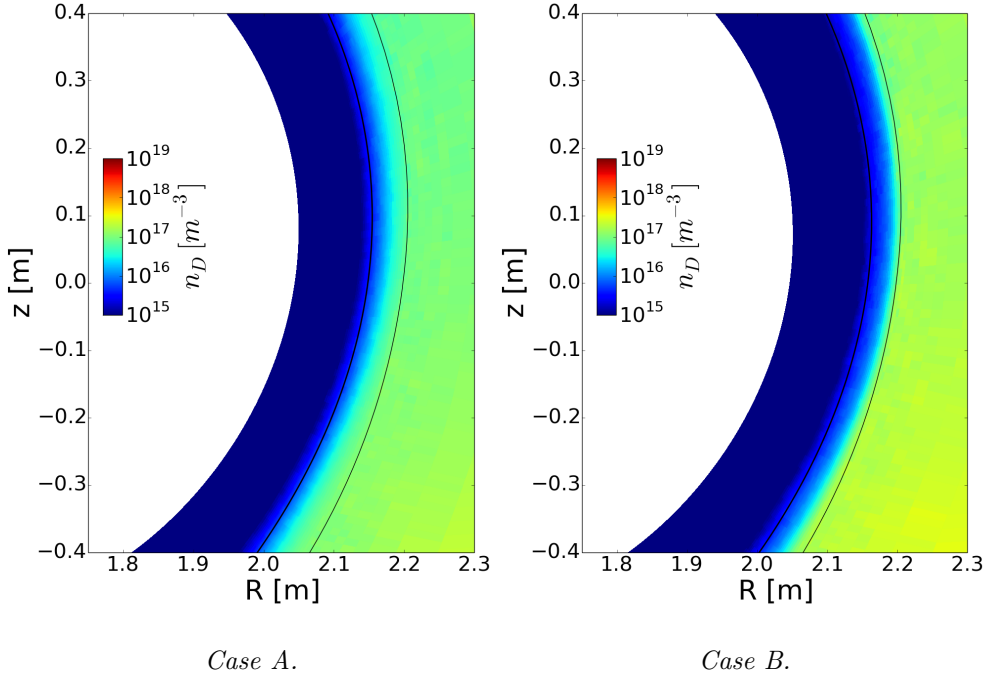


Figure 6.6: An enlargement of the outer target for both the low (left) and the high (right) density case. The color code is shown in the figures.

6.3 Collisionality along a field line

In section 2.6 it was shown how filament-related transport undergoes a regime transition, when the divertor collisionality increases. Nevertheless the experimental measures are localized in the divertor and in the outer midplane and how the collisionality evolves along a field line is not known. It is possible to calculate the collisionality parameter defined in section 2.5.2 in the whole SOL using the results of the simulation as inputs. That parameter changes locally accordingly to the plasma conditions. In order to understand how the collisionality evolves along a field line the integral of the collisionality along the field line is computed as:

$$\Lambda = \frac{\Omega_i}{\Omega_e} \int_{innertarget}^{outertarget} \nu_{ei}(s_{\parallel}) \frac{1}{c_s(s_{\parallel})} ds_{\parallel} \quad (6.3)$$

where $\nu_{ei}(s_{\parallel})$ is the local collision frequency between electron and ion for momentum exchange, $c_s(s_{\parallel})$ is the local sound speed and ds_{\parallel} is an interval along the field line. The connection length is given by:

$$L_c = \int_{innertarget}^{outertarget} ds_{\parallel} \quad (6.4)$$

Instead of computing the integral from target to target it is more interesting to study the collisionality from a target to a poloidal position as:

$$\Lambda(\theta) = \frac{\Omega_i}{\Omega_e} \int_{target}^{x(\theta)} \nu_{ei}(s_{\parallel}) \frac{1}{c_s(s_{\parallel})} ds_{\parallel} \quad (6.5)$$

where $x(\theta)$ represents the position along a field line of the poloidal position θ and target can be the inner or the outer target. The integral 6.5 are discretized over the grid used for the simulations. Both the collisionality from the inner target to the midplane and from the outer target to the midplane are calculated using the plasma parameters provided by simulations described in section 5.5. In case A (figure 6.7 left) the collisionality is below unity and it increases from the target to the midplane. In contrast to this the collisionality increases up to $\simeq 10$ in the divertor region in the high density case (figure 6.7 right) and is almost constant until the midplane. Once that the field line surpasses the low temperature belt around the divertor targets the relative contribution to the total collisionality is almost the same for both cases. This confirms the experimental observation that the divertor target conditions rule the filament regime transition. Moreover the total collisionality decreases moving from the separatrix to the wall. In the high density case the collisionality goes back to a value below unity in the far SOL. As a result filaments are in the inertial regime when they enter the SOL and in the sheath limited regime in the far SOL. This observation is consistent with the experimental measurements [32] and with the fact the filament-related transport in the simulation must be reduced to properly simulate the density shoulder formation.

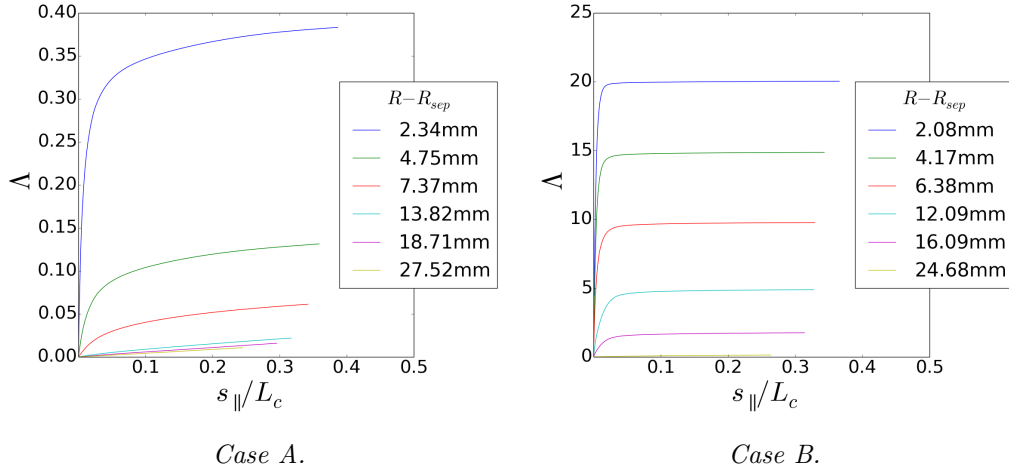


Figure 6.7: Collisionality along the field lines from the outer target to the midplane. The radial distance of the field lines from the separatrix at the outboard midplane is given in legends.

The point along a field line where the collisionality reaches 90% of its maximum value is shown in figures 6.8 *a* and *b*. In the low density case the position where the collisionality saturates is near the divertor targets in the vicinity of the separatrix, then the position where the collisionality saturates slowly reaches the midplane. On the other hand in the high density case a belt of high collisionality

covers the divertor targets near the separatrix, then it reaches the midplane when the total collisionality becomes lower than unity.

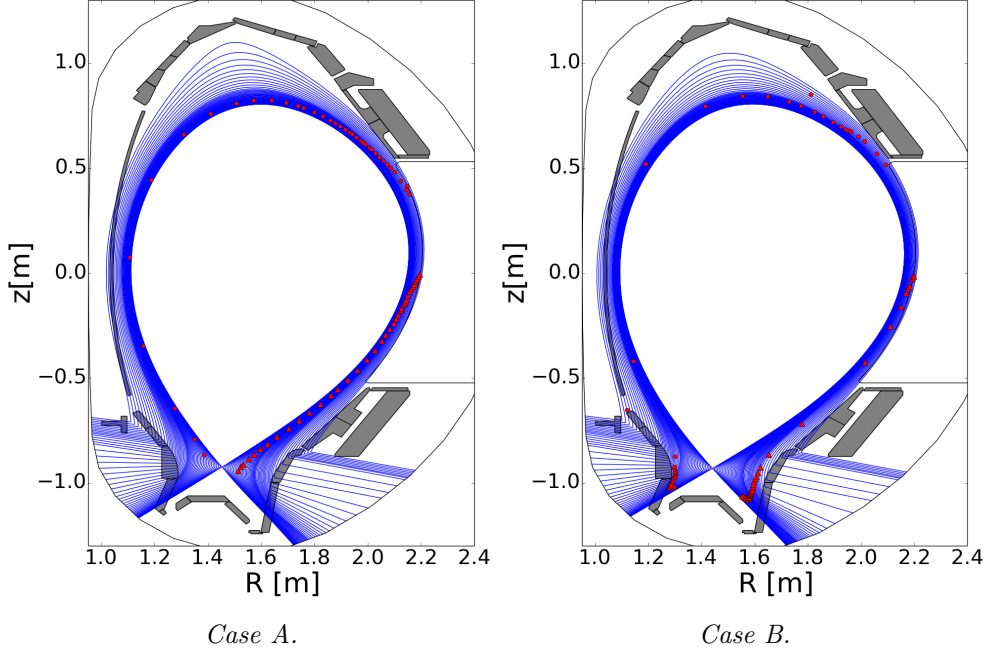


Figure 6.8: Poloidal position, where collisionality along the field line reaches 90% of its total value. Red circles refer to the line-integrated collisionality from the inner divertor target to the midplane, red triangles to that from the outer divertor target to the midplane.

6.4 Thermalization time

After the transition both in filaments and background temperature is substantially reduced (see section 2.6). Which mechanism is responsible for this effect is not clear yet. In section 2.4.1 the different effects that reduce the ion temperature are described. The results provided by the simulations allow to calculate the characteristic times for each of them and then which is the phenomenon that is the most relevant in cooling down the ions.

Figure 6.9 shows the thermalization time at the outboard midplane for each process along with the filament characteristic travel time for a given position (shown in the x axes). The filament velocity used for this calculation is the one measured in the experiments. In the low density case the filaments cross almost all the scrape-off layer without losing their energy. Moreover in case A two processes contribute to cool down the filament in the far SOL: the heat conduction and the neutral-ion interactions. In case B the only relevant process is the neutral-ion collision. This is consistent with the increase of the collisionality. In fact, since collisions between ions reduce the parallel transport (see equation 2.38), it seems likely that the radial transport becomes dominant in the high density case. On the other hand the increase of the neutral particles enhances the energy

loss via multiple collisions. Moreover as discussed in section 6.2 the neutral particle density is underestimated according to experiments and as a result the characteristic collision time is also underestimated. In order to account for this, an hypothetical thermalization time is also calculated assuming a neutral density profile four times higher than the one obtained by the simulation. As result, the inferred thermalization time (dashed red line in figure 6.9 right) is smaller than the filament travel time near the separatrix. If, as discussed, measurements overestimate the neutral density, the most likely neutral-ion thermalization time can be expected to lie between the two red curves in figure 6.9. In any case, neutral-ion collisions is the only process that seems to be short enough to cool down the filament.

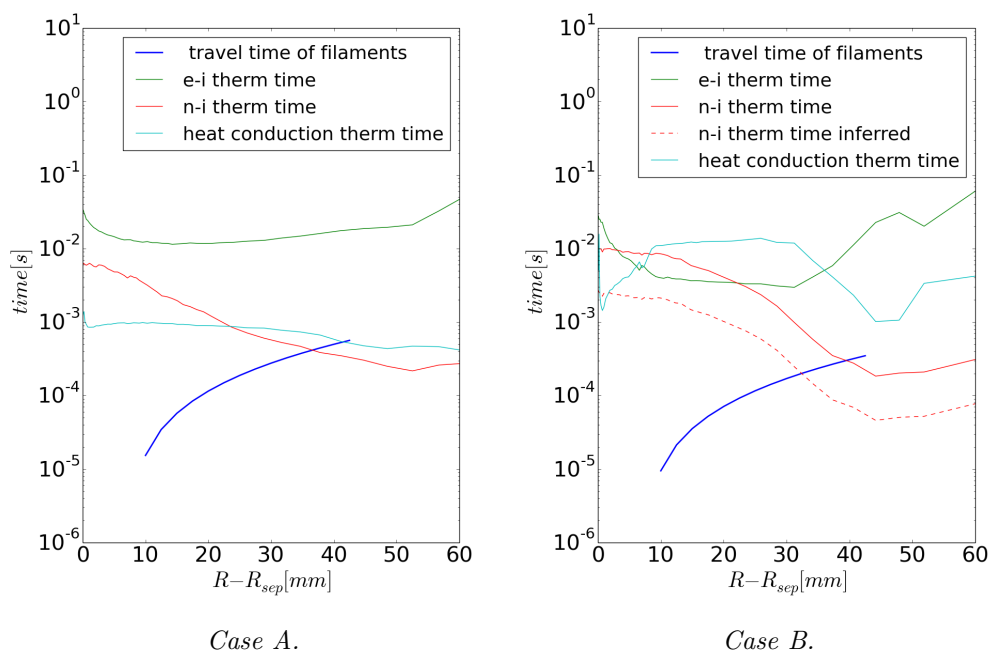


Figure 6.9: Thermalization and filament travel time against the distance from the separatrix. The solid blue lines show the filament travel time from the separatrix to a position in the midplane, the filament velocities are the ones measured in the experiment. The red, green and cyan solid curves represent the thermalization times as they are described in section 2.4.1. The dashed red line in left figure shows the neutral ion thermalization time computed for a four time higher neutral density then in the simulation, as measured by the neutral gas manometers.

The simulations provide a complete picture of the thermalization time in the whole scrape-off layer. Figure 6.10 shows the neutral-ion thermalization time, that is the most important one among the processes considered. Before the shoulder formation (figure 6.10 on the left) the neutral-ion collision time is lower than a ms only very close to the divertor targets. After the transition the neutral particles in the divertor region increase (see section 6.2) and that region extends up to the X-point. The interaction with neutral particles cools down the plasma by increasing the collisionality.

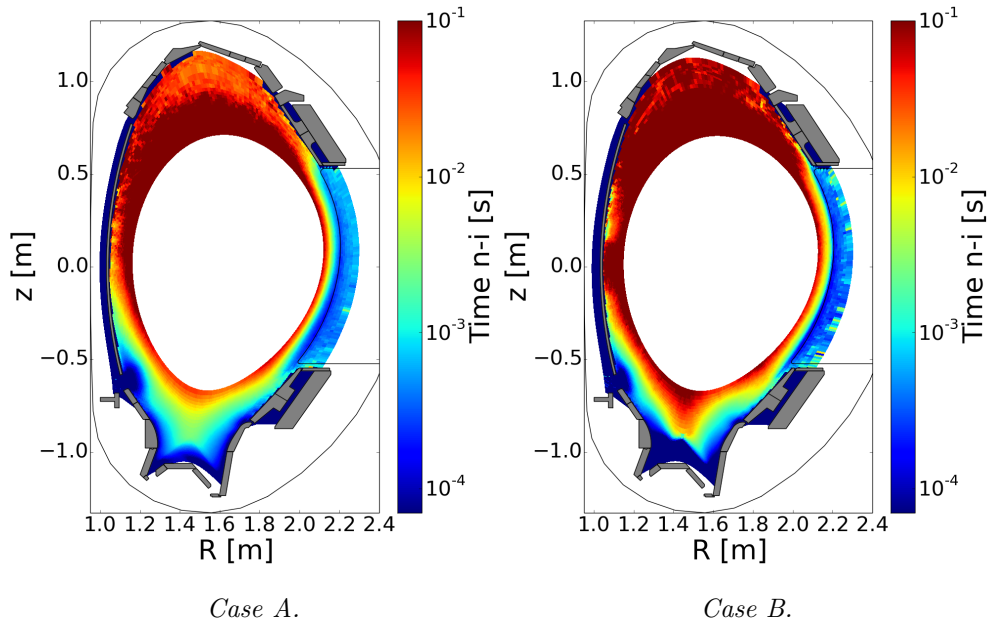


Figure 6.10: Characteristic thermalization time for neutral-ion collisions in a poloidal cross section for both cases A (left) and B (right).

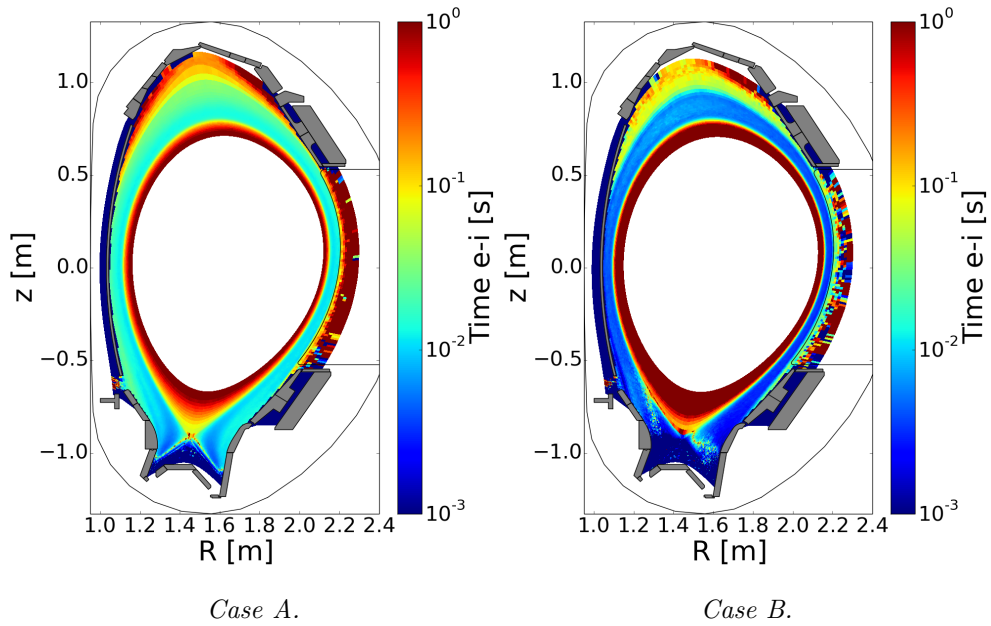


Figure 6.11: Characteristic thermalization time for electron ion collisions for both cases A (left) and B (right).

The parallel heat conduction time shows the opposite behavior with respect to the phenomenon of the neutral-ion collisions. In case A the parallel heat conduction is below 1 ms everywhere, on the other hand in the high density case the parallel heat conduction is of the order of $\simeq 10$ ms and therefore negligible

compared to the characteristic neutral-ion collision time.

The characteristic electron-ion collision time is negligible in both cases. Even if it is reduced after the transition, its value is higher than 1 ms 6.11, higher than the other processes. This is consistent with the observation that electrons and ion have different temperature: If the electron-ion collision time was not negligible they would have the same temperature.

6.5 Perpendicular fluxes

The density shoulder formation may lead to changes in the heat and particle fluxes against the plasma facing components. In order to discuss this, those fluxes are calculated using the results provided by the simulations:

$$\Gamma_{\perp} = -D_{\perp} \nabla_{\perp} n_e \quad (6.6)$$

$$q_{\perp}^{e,i} = -n_e \chi_{\perp}^{e,i} \nabla_{\perp} T_{e,i} \quad (6.7)$$

where Γ_{\perp} and $q_{\perp}^{e,i}$ represent the particle and heat fluxes respectively.

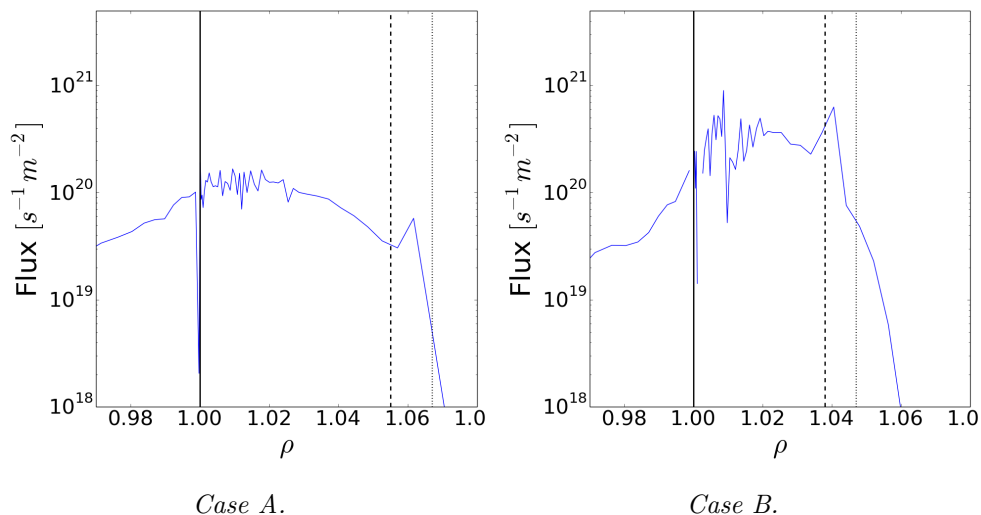


Figure 6.12: Particle flux at the outboard midplane for case A (left) and case B (right) respectively. The black dashed and dotted lines are the limiters, while the solid line is the separatrix.

The results are affected by Monte-Carlo noise, which implies a strong fluctuation in the gradient. Still, the results can be used to provide a qualitative picture of the transport. Figure 6.12 shows the particle flux for the two simulated cases: in the low density case (6.12 left) the particle flux at the limiters is around one order of magnitude lower respect to the high density case (6.12 right). In both cases, the particle flux increases in the SOL region, but in case A it decreases constantly until the limiters, while in case B it is almost constant until the limiter where it has a sharp decrease. In case B the particle flux is $\simeq 5$ times the flux of case A in the SOL region, in good agreement with the experimental results.

The energy fluxes due to electrons and ions are shown in figure 6.13. The energy fluxes show the same trend as the particles flux: in case A the fluxes decrease constantly, while in case B they are constant in the SOL and decrease after the limiter. It is important to notice that after the shoulder formation the particle flux is increased, but differently the heat fluxes are almost of the same order of magnitude in good agreement with the experimental results [33, 34]. In any case, the constant decrease of the fluxes in the low density case leads to a lower power deposition on the limiters. Moreover in the high density case the power density that flows onto the limiter is in the order of $\simeq 1 \text{ kWm}^{-2}$ similar to the one measured in the divertor targets 5.19. This means that after the shoulder formation the PFCs must withstand similar conditions as the one observed at the divertor targets in the detached regime.

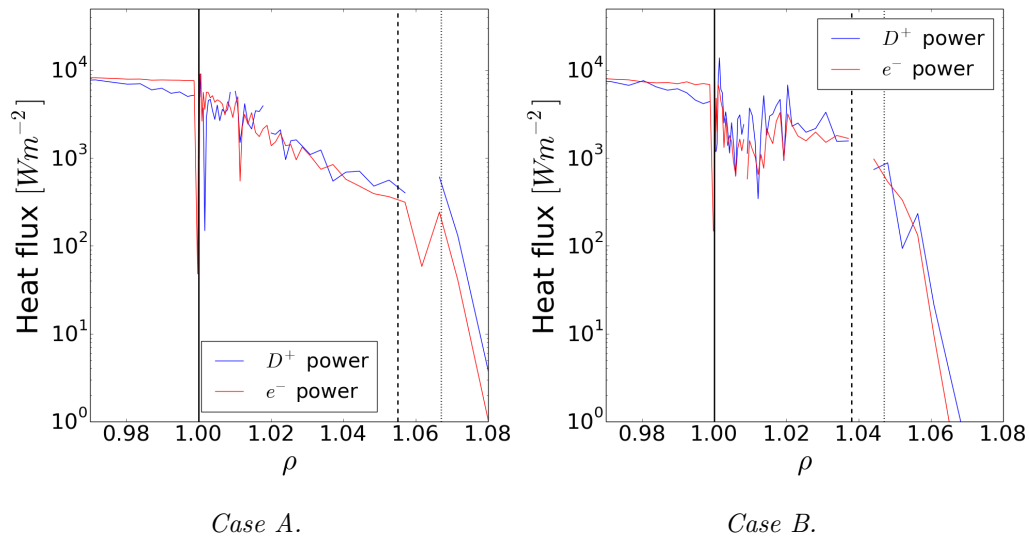


Figure 6.13: Heat fluxes at the outboard midplane for cases A (left) and B (right). The black dashed and dotted lines are the limiters, while the solid line is the separatrix.

Chapter 7

Summary and conclusions

In continuation of previous work [3], two different L-mode discharges at different degrees of shoulder formation are simulated. The filament-related transport, that is responsible for the shoulder formation, is described using diffusive, time independent transport coefficients. The function that describes the transport coefficients depends on the radial and poloidal position: this is an improvement with respect to the previous simulation that considers the transport coefficients to be a poloidally homogeneous function that depends only on the radial position. This provides a more realistic picture of the filament-related transport in the SOL, that is localized in the outer midplane. The results of the simulations are compared with the experimental measurements from different diagnostics: lithium beam, Thomson scattering, charge exchange recombination spectroscopy and probes at the midplane, Langmuir probes at the X-point, Langmuir probes at the divertor targets and neutral gas manometers. The measured experimental profiles are shifted in order to have a consistent picture of density and temperature at the outer midplane. The comparison shows how the implementation of the poloidally-dependent coefficient improves the agreement between the simulation and the experimental data. At the midplane, the simulated density and electron temperature match properly the experimental observations for both cases. Also in both cases, the simulations overestimate the ion temperature. At the targets, the simulations match only partially the experimental measurements because of the detachment. At the X-point the agreement between the experimental measurements and the numerical results has strongly improved, except at the X-point, the simulation significantly overestimates the density. The neutrals density provided by the simulations is in good agreement with the experimental measurements in low density case, while in high density case the simulations underestimate the neutral density both at the targets and midplane. Analyzing the simulations, the following conclusions can be drawn:

- It is possible to simulate the density shoulder formation by increasing transport by a factor 3 only at the outer midplane, in good agreement with the experimental measurements.
- A reduction in the particle transport coefficient at the limiter surface is needed in order to match the experimental profiles. This is in good agree-

ment with recent observations that show a reduction of the filament-related transport in the far SOL [32].

- A better agreement is achieved if the energy transport coefficients are decoupled from the ones for particle transport.

The results provided by the simulations are then used to analyze the plasma background differences before and after the shoulder formation. After the transition the collisionality increases and when it is larger than unity it causes the filament regime transition. Moreover it is observed that after the shoulder formation the collisionality along a field line saturates at the divertor targets. When analyzing the effects of shoulder formation at the outer midplane, it has been found that the most likely to cool down the filaments is the interaction between neutrals and ions.

Chapter 8

Acknowledgment

Finally I want to thank the ones that help me with this work: my supervisors in Germany: Daniel Carralero and Tilmann Lunt that patiently guide me and correct my "kindergarten" English. Elizabeth Wolfrung, Georg Birkenmeier, Dominik Brida and all the others of the E2M group for their help and their kindness. The IPP for the opportunity and FuseNet for the financial support.

Concludo con qualche breve riga in italiano, con le quali voglio ringraziare la mia famiglia per avermi sostenuto ed aiutato. La mia relatrice e professoressa Claudia Riccardi per la sua disponibilità e il prezioso aiuto. I miei compagni (comunisti) di università Erika, Simone e Bobbi (recentemente aggiornato in Paolo Banale), coi quali ho affrontato l'ardua sfida di sopravvivere alla burocrazia e alla, ben più semplice, laurea magistrale. Particolare menzione va a Bobbi con cui ho condiviso i corsi per oltre un anno, guadagnandoci la menzione "Sembra una vecchia coppia sposata!". I ragazzi conosciuti in Germania Sergiu, Jacob, Patrik, Berd e Bernhard che hanno tollerato il mio essere "too italian" (ma forse l'hanno fatto per i liquori e il caffè). Mimo e Mauricio per la merenda delle 16:00. Grazie per le serate, le grigliate i tuffi nel fiume e le discussioni senza fine dopo pranzo. Infine ringrazio Isabella per avermi sopportato, per l'aiuto con l'inglese, per le vacanze e per i caffè dopo pranzo e per essersi finita tutto il mio arancino.

Bibliography

- [1] INTERNATIONAL ATOMIC ENERGY AGENCY. *Fusion Physics*. Vienna: INTERNATIONAL ATOMIC ENERGY AGENCY, 2012. Chap. 1. URL: <http://www-pub.iaea.org/books/IAEABooks/8879/Fusion-Physics>.
- [2] ITER Organization. *ITER - the way to new energy About*. 2016. URL: <https://www.iter.org> (visited on 06/29/2016).
- [3] “EMC3-Eirene simulations of particle- and energy fluxes to main chamber- and divertor plasma facing components in ASDEX Upgrade compared to experiments”. In: ().
- [4] INTERNATIONAL ATOMIC ENERGY AGENCY. *Fusion Physics*. Vienna: INTERNATIONAL ATOMIC ENERGY AGENCY, 2012. Chap. 3, pp. 227–237. URL: <http://www-pub.iaea.org/books/IAEABooks/8879/Fusion-Physics>.
- [5] Prof. Ian Hutchinson. *Collisions in Plasmas Lecture Notes*. 2016. URL: <http://ocw.mit.edu/courses/nuclear-engineering/22-611j-introduction-to-plasma-physics-i-fall-2006/readings/chap3.pdf> (visited on 08/21/2016).
- [6] S. I. Braginskii. “Transport Processes in a Plasma”. In: *Reviews of Plasma Physics* 1 (1965), p. 205.
- [7] D. A. DIppolito, J. R. Myra, and S. J. Zweben. “Convective transport by intermittent blob-filaments: Comparison of theory and experiment”. In: *Physics of Plasmas* 18.6, 060501 (2011). DOI: <http://dx.doi.org/10.1063/1.3594609>. URL: <http://scitation.aip.org/content/aip/journal/pop/18/6/10.1063/1.3594609>.
- [8] JA Boedo et al. “Transport by intermittent convection in the boundary of the DIII-D tokamak”. In: *Physics of Plasmas* 8.11 (2001), pp. 4826–4833.
- [9] DL Rudakov et al. “Fluctuation-driven transport in the DIII-D boundary”. In: *Plasma physics and controlled fusion* 44.6 (2002), p. 717.
- [10] H. Meyer et al. “Overview of physics results from MAST”. In: *Nuclear Fusion* 49.10 (2009), p. 104017. URL: <http://stacks.iop.org/0029-5515/49/i=10/a=104017>.

- [11] S.I. Krasheninnikov. “On scrape off layer plasma transport”. In: *Physics Letters A* 283.56 (2001), pp. 368 –370. ISSN: 0375-9601. DOI: [http://dx.doi.org/10.1016/S0375-9601\(01\)00252-3](http://dx.doi.org/10.1016/S0375-9601(01)00252-3). URL: <http://www.sciencedirect.com/science/article/pii/S0375960101002523>.
- [12] M. Wiesenberger, J. Madsen, and A. Kendl. “Radial convection of finite ion temperature, high amplitude plasma blobs”. In: *Physics of Plasmas* 21.9, 092301 (2014). DOI: <http://dx.doi.org/10.1063/1.4894220>. URL: <http://scitation.aip.org/content/aip/journal/pop/21/9/10.1063/1.4894220>.
- [13] J. R. Myra, D. A. Russell, and D. A. DiIppolito. “Collisionality and magnetic geometry effects on tokamak edge turbulent transport. I. A two-region model with application to blobs”. In: *Physics of Plasmas* 13.11, 112502 (2006). DOI: <http://dx.doi.org/10.1063/1.2364858>. URL: <http://scitation.aip.org/content/aip/journal/pop/13/11/10.1063/1.2364858>.
- [14] D. Carralero et al. “Experimental Validation of a Filament Transport Model in Turbulent Magnetized Plasmas”. In: *Phys. Rev. Lett.* 115 (21 2015), p. 215002. DOI: 10.1103/PhysRevLett.115.215002. URL: <http://link.aps.org/doi/10.1103/PhysRevLett.115.215002>.
- [15] D. Carralero et al. “An experimental investigation of the high density transition of the scrape-off layer transport in ASDEX Upgrade”. In: *Nuclear Fusion* 54.12 (2014), p. 123005. URL: <http://stacks.iop.org/0029-5515/54/i=12/a=123005>.
- [16] D. Carralero et al. “Implications of high density operation on SOL transport: A multimachine investigation”. In: *Journal of Nuclear Materials* 463 (2015), pp. 123 –127. ISSN: 0022-3115. DOI: <http://dx.doi.org/10.1016/j.jnucmat.2014.10.019>. URL: <http://www.sciencedirect.com/science/article/pii/S002231151400703X>.
- [17] Sergiu Artene. “A study on the transport of particles and heat of plasma filaments in the scrape-off layer of ASDEX Upgrade”. MA thesis. TMU, 2016.
- [18] D. A. DiIppolito and J. R. Myra. “Thermal transport catastrophe and the tokamak edge density limit”. In: *Physics of Plasmas* 13.6, 062503 (2006). DOI: <http://dx.doi.org/10.1063/1.2206168>. URL: <http://scitation.aip.org/content/aip/journal/pop/13/6/10.1063/1.2206168>.
- [19] A Kallenbach et al. “Divertor power load feedback with nitrogen seeding in ASDEX Upgrade”. In: *Plasma Physics and Controlled Fusion* 52.5 (2010), p. 055002. URL: <http://stacks.iop.org/0741-3335/52/i=5/a=055002>.
- [20] Max Planck institut fur plasmaphysik. *ASDEX Upgrade database - plasma parameters About*. 2000. URL: <https://www.aug.ipp.mpg.de/documentation/bin/view/AUGProject> (visited on 09/08/2016).
- [21] Max Planck institut fur plasmaphysik. *ASDEX Upgrade database - plasma parameters About*. 2000. URL: <https://www.aug.ipp.mpg.de/documentation/bin/view/Diagnostics> (visited on 09/08/2016).

- [22] Hans Meister. *Überblick über die Ladungsaustauschspektroskopie an ASDEX Upgrade*. URL: https://www.aug.ipp.mpg.de/~hsm/diagnostik/cxrs_general.html (visited on 08/17/2016).
- [23] Daniel Carralero Ortiz. “Electromagnetic Instability Studies in Fusion Plasmas Edge”. PhD thesis. UNIVERSIDAD POLITÉCNICA DE MADRID, 2012.
- [24] M Willensdorfer et al. “Characterization of the Li-BES at ASDEX Upgrade”. In: *Plasma Physics and Controlled Fusion* 56.2 (2014), p. 025008.
- [25] B Kurzan et al. “Signal processing of Thomson scattering data in a noisy environment in ASDEX Upgrade”. In: *Plasma Physics and Controlled Fusion* 46.1 (2004), p. 299. URL: <http://stacks.iop.org/0741-3335/46/i=1/a=019>.
- [26] H. Murmann et al. “The Thomson scattering systems of the ASDEX upgrade tokamak”. In: *Review of Scientific Instruments* 63.10 (1992), pp. 4941–4943. DOI: <http://dx.doi.org/10.1063/1.1143504>. URL: http://scitation.aip.org/content/aip/journal/rsi/63/10/10.1063/1.1143504;jsessionid=mvV_wvee33ZW19VG1_BHKzqf.x-aip-live-02.
- [27] E. Viezzer et al. “High-resolution charge exchange measurements at ASDEX Upgrade”. In: *Review of Scientific Instruments* 83.10, 103501 (2012). DOI: <http://dx.doi.org/10.1063/1.4755810>. URL: <http://scitation.aip.org/content/aip/journal/rsi/83/10/10.1063/1.4755810>.
- [28] B Nold et al. “Generation of blobs and holes in the edge of the ASDEX Upgrade tokamak”. In: *Plasma Physics and Controlled Fusion* 52.6 (2010), p. 065005. URL: <http://stacks.iop.org/0741-3335/52/i=6/a=065005>.
- [29] M. Tsalas et al. “Langmuir probe measurements in the lower x-point vicinity of the {ASDEX} Upgrade divertor”. In: *Journal of Nuclear Materials* 337339 (2005). PSI-16, pp. 751–755. ISSN: 0022-3115. DOI: <http://dx.doi.org/10.1016/j.jnucmat.2004.09.027>. URL: <http://www.sciencedirect.com/science/article/pii/S002231150400861X>.
- [30] Y Feng et al. “3D edge modeling and island divertor physics”. In: *Contributions to Plasma Physics* 44.1-3 (2004), pp. 57–69.
- [31] Feng et. all. In: *Contributions to Plasma Physics* 44.611 (2001).
- [32] G Fuchert et al. “Towards a quantitative prediction of the blob detection rate”. In: *Plasma Physics and Controlled Fusion* 58.5 (2016), p. 054006. URL: <http://stacks.iop.org/0741-3335/58/i=5/a=054006>.
- [33] Carralero et all. “Recent Progress towards a Quantitative Description of Filamentary SOL Transport”. In: *Proceedings of the IAEA Fusion Energy Conference*. Kyoto, Japan, 2016.
- [34] Guillemaut et all. “Comparative H-mode density limit studies in JET and AUG”. In: *Proceedings of the Plasma Surface Interaction conference*. Rome, Lazio, Italy, 2016.